

2-DIMENSIONAL INTERCALATED CYANO-METALLATE COMPLEXES-
APPROACH TO ULTRAFILTRATION

by

Babatunde Matthew Adebisi, B.S., M.S.

A dissertation submitted to the Graduate Council of
Texas State University in partial fulfillment
of the requirements for the degree of
Doctor of Philosophy
with a Major in Material Science, Engineering, and Commercialization
May 2019

Committee Members:

Gary W. Beall, Chair

Kevin Lewis

Benjamin R. Martin

William Chittenden

Alex Zakhidov

COPYRIGHT

by

Babatunde Matthew Adebisi

2019

FAIR USE AND AUTHOR'S PERMISSION STATEMENT

Fair Use

This work is protected by the Copyright Laws of the United States (Public Law 94-553, section 107). Consistent with fair use as defined in the Copyright Laws, brief quotations from this material are allowed with proper acknowledgement. Use of this material for financial gain without the author's express written permission is not allowed.

Duplication Permission

As the copyright holder of this work I, Babatunde Matthew Adebisi, authorize duplication of this work, in whole or in part, for educational or scholarly purposes only.

DEDICATION

I dedicate this work to my late cousin, Segun Ogunleye, rest on.

ACKNOWLEDGEMENTS

I would like to thank my advisor, Dr. Gary Beall for his guidance and relentless effort and input in making sure the research is completed. I would like to thank Dr. Clois Powel (Rtd) for his insights, Dr. Ben Martin and my dissertation committee members for their inputs and positive criticism that brought me up to speed. To Dr. Shazly and Dr. Michael Opoku for their assistance in proffering solutions to my several questions.

I would like to thank my wife, Victoria for her support and understanding during my program. I would also like to appreciate my parents and my sisters; Keji, Funmilola, Taiwo and Kehinde Adebisi for believing in me and for their prayers and patience without which I will not be able to achieve this feat. To my friends Mr. and Mrs. Olanrewaju Ogedengbe, and Mr. and Mrs. Bolaji Adesanya, I say a big Thank you.

The financial support for this work by Graduate School Fellowship and MSEC program is highly appreciated.

TABLE OF CONTENTS

	Page
ACKNOWLEDGEMENTS.....	v
LIST OF TABLES.....	ix
LIST OF FIGURES	x
ABSTRACT.....	xv
CHAPTER	
1. INTRODUCTION	1
1.1 Background	1
1.2 Review of The Literature	3
1.2.1 Nature of Transition Metal in 3D Metal Framework.....	3
1.2.2 Fe, Ni, Mn and Co Transition Metal.....	4
1.2.3 Preceding Background Work.....	6
1.2.4 Potential Applications.....	14
1.3 Dissertation Effort and Research Objectives	16
2. EXPERIMENTAL METHODS.....	19
2.1 Preparation of Divalent Transition Metal Powder Complexes	19
2.1.1 Treatment of samples with DDP.....	21
2.1.2 Preparation of Powder Complex for SEM Imaging.....	21
2.1.3 X-Ray Diffraction Analysis	22
2.1.4 Thermo Graph Analysis	22
2.1.5 Raman Scattering.....	22
2.1.6 Transmission Electron Microscopy	22
2.1.7 Vibrating Sample Magnetometry.....	23
2.2 Divalent Transition Metal Growth Method on Microporous Membranes	23
2.2.1 Na Ion Selectivity	26
3. RESULTS AND DISCUSSIONS.....	30
3.1 FeNi(CN) ₄ and Derivative.....	30
3.1.1 X-Ray Diffraction	30

3.1.2	SEM and EDAX for Fe Transition Metal Complex	33
3.1.3	TEM Imaging for the Fe Transition Metal Complex	36
3.1.4	Raman Scattering for Fe Transition Metal Complex	40
3.1.5	TGA for Fe Transition Metal Complex	42
3.1.6	VSM for Fe Transition Metal Complex	43
3.2	MnNi(CN) ₄ and Derivative	44
3.2.1	X-Ray Diffraction	44
3.2.2	SEM and EDAX for Mn Transition Metal Complex	45
3.2.3	TEM Imaging for Mn Transition Metal Complex	47
3.2.4	Raman Scattering for Mn Transition Metal Complex	52
3.2.5	TGA for Mn Transition Metal Complex	53
3.2.6	VSM for Mn Transition Metal Complex	54
3.3	Ni ₂ (CN) ₄ and Derivative	55
3.3.1	X-Ray Diffraction	55
3.3.2	SEM and EDAX for Ni Transition Metal Complex	56
3.3.3	TEM Imaging for Ni Transition Metal Complex	58
3.3.4	Raman Scattering for Ni Transition Metal Complex	61
3.3.5	TGA for Ni Transition Metal Complex	62
3.3.6	VSM for Ni Transition Metal Complex	63
3.4	CoNi(CN) ₄ and Derivative	64
3.4.1	X-Ray Diffraction	65
3.4.2	SEM and EDAX for Co Transition Metal Complex	66
3.4.3	TEM Imaging for Co Transition Metal Complex	67
3.4.4	Raman Scattering for Co Transition Metal complex	71
3.4.5	TGA for Co Transition Metal Complex	72
3.4.6	VSM for Co Transition Metal Complex	72
3.5	Filtration Results of Transition Metal Complex on Microporous Fiber	73
3.6	BET Surface Area Results and Analysis	78
4.	RECOMMENDATION AND CONCLUSION	79
4.1	Recommendation for Future Work	79
4.2	Conclusions	79
5.	SYNTHESIS OF NICKEL FERRITE-GRAPHITIC LAYERS NANOCOMPOSITE WITH INVERTED MAGNETIC HYSTERESIS	82
5.1	Introduction	82
5.2	Experimental work	83
5.3	Characterizations	83
5.4	Results and Discussions	84

5.4.1	X-ray Diffraction	84
5.4.2	Scanning Electron Microscopy	85
5.4.3	Transmission Electron Microscopy	86
5.4.4	Raman Spectroscopy.....	87
5.4.5	Magnetic Properties	88
5.5	Proposed Mechanism of Nickel Ferrite Formation	90
5.5.1	Conclusions	92
APPENDIX SECTION.....		94
REFERENCES		98

LIST OF TABLES

Table	Page
1. Electronic Configurations for Mn, Co, Fe and Ni Transition Metals.....	5
2. Weight of potassium tetracyanonickelate complex and corresponding weight of transition metal salt.....	20
3. FWHM for calculating nanosize particle.....	33
4. Molarity Calibration.....	74
5. Linear Fit Summary for Na Ion Concentration.....	75
6. NaCl concentration in filtered water through respective membranes.....	76

LIST OF FIGURES

Figure	Page
1. Illustration of metal organic framework	2
2. Representation of octahedral and square planar coordination of a typical transition framework.....	4
3. Octahedral crystal field splitting.....	5
4. Low spin and high spin configuration of Fe^{2+} in $3d_6$ coordination	6
5. Generalized diagram of a Hofmann benzene clathrate.....	7
6. Assembly of two-dimensional grid networks at the air-water interface.....	12
7. Simplified mechanism for exfoliation of 3D structures into 2D sheets.....	13
8. Temperature dependence of the product of the zero-field cooled magnetization.....	15
9. Diagram showing square framework of atoms in a single layer.	18
10. Powder samples of $\text{MNi}(\text{CN})_4$. Where M is (a) Fe, (b) Ni, (c) Co and (d) Mn.....	20
11. Growth method for metal CN network.....	24
12. NaCl filtration set-up with vacuum pump.....	26
13. NaCl filtration set-up with tap to maintain differential pressure.....	28
14. Figure showing filtration set-up for powdered samples supported on filter paper supported sintered glass.....	29
15. X-ray diffraction pattern for $\text{FeNi}(\text{CN})_4$ before (black lines) and after exfoliation in DDP (blue lines).....	30
16. Similar X-ray diffraction pattern from literature for Zn substituted specie.....	31
17. FWHM of $\text{Fe}(\text{CN})_4$ for obtaining mean particle size.....	32

18. SEM images of FeNi(CN) ₄ at (a) 2500x, (b) 65000x, (c) 80000x and (d) spots mapped for EDAX.....	33
19. EDAX for images of FeNi(CN) ₄	34
20. SEM images of FeNi(CN) ₄ after exfoliation in DDP at (a)65000x, (b)50000x, (c) enhanced picture of 65000x and (d) spots mapped for EDAX.....	35
21. EDAX for Images of FeNi(CN) ₄ after treatment with DDP.....	36
22. Transmission electron images at (a) 40 nm and (b) 10 nm of the FeNi(CN) ₄ , revealing multilayer structure of the sample.....	37
23. Electron diffraction pattern of the FeNi(CN) ₄	37
24. TEM images of FeNi(CN) ₄ after treatment with DDP (a) 40 nm, (b) 20 nm, revealing single standing sheets of sample.....	39
25. Electron diffraction pattern of FeNi(CN) ₄ after treatment with DDP.....	40
26. Raman spectra in the 150-600 cm ⁻¹ region, inset shows the prominent CN ‘B1g’ and ‘A1g’ spectra in the 2100-2300 cm ⁻¹ region.....	41
27. TGA. Analysis for Fe samples (a) before and (b) after exfoliation with DDP.....	42
28. Magnetic hysteresis loop for Fe complexes.....	44
29. X-ray diffraction pattern for the MnNi(CN) ₄ before (blue line) and after exfoliation in DDP (black line).....	45
30. SEM Images of MnNi(CN) ₄ at (a)120000x, (b)150000x, (c) 80000x and (d) spot mapped for EDAX.....	46
31. EDAX for images of MnNi(CN) ₄	46
32. Transmission electron images at (a) 8 nm and (b) 60 nm of MnNi(CN) ₄ , revealing multilayer structure of the sample.....	48
33. Electron diffraction pattern of MnNi(CN) ₄	49
34. TEM images of MnNi(CN) ₄ after treatment with DDP (a) 10 nm, (b) 20 nm, revealing single standing sheets of sample.....	50

35. TEM images of the MnNi(CN) ₄ showing distinct regions with different d-spacing...	51
36. Electron diffraction pattern of MnNi(CN) ₄ after treatment with DDP.....	52
37. Raman spectra in the 150-600 cm ⁻¹ region, inset shows the prominent CN ‘B1g’ and ‘A1g’ spectra in the 2100-2300cm ⁻¹ region.....	53
38. TGA. Analysis for Mn samples (a) before and (b) after exfoliation with DDP.....	54
39. Magnetic hysteresis loop for Mn complexes.....	55
40. X-ray diffraction pattern for NiNi(CN) ₄ before (blue line) and after exfoliation in DDP (black line).....	55
41. (a) SEM images for NiNi(CN) ₄ before exfoliation in DDP, (b) Spot mapped for EDAX.....	56
42. (a) SEM images for the NiNi(CN) ₄ after exfoliation in DDP, (b) Spots mapped for EDAX.....	57
43. EDAX for Images of NiNi(CN) ₄ (a) before exfoliation in DDP, (b&c) after exfoliation in DDP.....	57
44. Transmission electron images at (a) 10 nm and (b) 20 nm (c) 80 nm of NiNi(CN) ₄ , revealing multilayer structure of the sample.....	58
45. Electron diffraction pattern of NiNi(CN) ₄ before exfoliation.....	59
46. TEM images of NiNi(CN) ₄ after treatment with DDP.....	60
47. Electron diffraction patterns of the NiNi(CN) ₄ after treatment with DDP.....	61
48. Raman scattering for Ni before exfoliation	62
49. TGA analysis for the Ni samples (a) before and (b) after exfoliation with DDP.....	63
50. Magnetic hysteresis loop for Ni complexes.....	64
51. X-ray diffraction pattern for CoNi(CN) ₄ before (red line) and after exfoliation in DDP (black line).....	65

52. Different colors of cobalt cyanonickelate complex.....	66
53. SEM images of $\text{CoNi}(\text{CN})_4$ at (a&b) 65000x, (c) 80000x, and (d) spots mapped for EDAX.....	67
54. EDAX for images of $\text{CoNi}(\text{CN})_4$	67
55. Transmission electron images at (a) 10 nm and (b) 60 nm of the $\text{CoNi}(\text{CN})_4$, revealing multilayer structure of the sample.....	68
56. Electron diffraction pattern of $\text{CoNi}(\text{CN})_4$	69
57. TEM images of $\text{CoNi}(\text{CN})_4$ after treatment with DDP.....	70
58. Electron diffraction pattern of $\text{CoNi}(\text{CN})_4$ after treatment with DDP.....	70
59. Raman shift for Co sample before exfoliation.....	71
60. TGA. Analysis for Co samples (a) before and (b) after exfoliation with DDP.....	72
61. Magnetic hysteresis loop for Co complexes.....	73
62. Linear fit for molarity calibration.....	75
63. Comparison of the amount of NaCl rejected during filtration.....	78
64. Limiting growth mechanism of complex within microporous membranes.....	81
65. X-ray Diffraction of synthesized Nickel Ferrite.....	85
66. SEM images of Nickel Ferrite (a) 1 μm (b) 300 nm.....	86
67. TEM Images of Nickel Ferrite (a) 100 nm (b) 10 nm.....	87
68. Raman spectra of Nickel Ferrite.....	88
69. Magnetic hysteresis loop of the Nickel Ferrite.....	90
70. Self-propagating ignition of Nickel Ferrite formation.....	91

71. Rapid expansion of iron tetracyanonickelate (II) to form Nickel Ferrite.....92

ABSTRACT

The discovery of graphene and other two-dimensional (2-D) materials has opened the way for a huge opportunity in material development, manipulation, and their corresponding potential applications. 2-D materials including graphene have been shown to have unique properties such as high electrical conductivity, high mobility, and high surface area. These properties have made 2-dimensional materials amenable to small-scale electronic applications, molecular sieves and for high strength composite applications. Despite the promise graphene holds, it has been difficult to completely harness its potential because it is difficult and expensive to produce single layer graphene sheets in substantial quantity. A unique class of 3-dimensional nanomaterials that can be produced in substantial quantity and cost effectively processed into 2-dimensional hybrid structures are the Metal Organic Frameworks (MOFs). MOFs, which are basically a composition of molecular complexes formed between metals and salts, organic and inorganic molecules, have been rationalized to be a coordination complex with a stereospecific structure. Transition Metal Cyanates are a unique class of 3-dimensional cyanometallate network. The most common are hexacyano transition metal complexes with divalent transition metal counter ions. We have prepared and exfoliated transition metal cyanates into 2-dimensional structures by exfoliation into separates sheets. Hybrid 2-D structures have also been produced and studied by intercalation with organic linkers.

Density Function Theory (DFT) studies have predicted an increase in the d-spacing of potassium tetra-cyanonickelate, on substitution with di-metallic cation such as

Fe^{2+} , Mn^{2+} , Cd^{2+} and Co^{2+} , and additional processing with organic linkers. Dodecyl pyrrolidone (DDP) was used to intercalate the metal complexes and X-ray diffraction results showed significant peak shifts to the left on all metal complexes, corroborating the DFT predictions. The increased distance between layers allows for further separation into exfoliated sheets. In this report, we have demonstrated an approach for producing a long-range defect-free 2-D sheets. We have grown di-metallic cation complexes of Fe^{2+} , Mn^{2+} , Ni^{2+} and Co^{2+} on Teflon supports. This was done by placing hydrophilic 1.0 micron Teflon as a barrier between a desired salt of the complex and potassium tetracyano nickelate. The desired metal complex was formed by diffusion of the opposing solution in the Teflon support. The membrane was dried and used as barrier for Na^+ ion selectivity test. The test was carried with 1.0 M NaCl. The solution was pumped under vacuum through the membrane, and a pristine membrane was used as a control. Results showed that the Fe and Mn tetracyano nickelate selectively reject Na^+ ion salts while control experiments proved otherwise.

These results hold promise for material applications in waste water remediation, separations, desalination, and purification. In this work, we also reported a simple process of synthesizing Nickel Ferrite-graphitic layers with inverted magnetic hysteresis.

1. INTRODUCTION

1.1 Background

The discovery of graphene and other two-dimensional (2-D) materials has opened the way for a huge opportunity in material development, manipulation, and their corresponding potential applications. 2-D materials including graphene have been shown to have unique properties such as high thermal conductivity, high electrical conductivity, and high electron mobility, with current densities of about 1,000,000X that of copper. The surface area of graphene is of the order of 2630 m²/g. These properties have made 2-dimensional materials amenable to small-scale electronic applications. Besides this, graphene has a great potential to be applied for high strength composite applications, owing to its inherent high tensile strength formed by the construct of sp² hybridized covalent bonds [1]. With a tensile strength of 130 GPa, graphene is 200X stronger than steel which has a tensile strength of 600 MPa [2, 3].

It has however been difficult to harness the full benefits of the interesting properties of graphene, partly because it is expensive to produce high quality graphene in substantial quantities that will be relevant for commercial applications. And partly because of challenges in integrating 2-dimensional materials into 3-dimensional systems. A 2015 roadmap for graphene and 2-dimensional materials highlights some of the challenges that need to be overcome with opinions that the cheapest 2-D materials with least stringent requirements could be the first to be available in the market for large-scale commercial applications [4].

A unique class of nanomaterials that can be produced in substantial quantity at a cost-effective production rate are the Metal Organic Frameworks (MOFs). MOFs consist

of metal ions coordinated to organic molecules to form multi-dimensional structures. It has been predicted that this class of compounds upon further processing can be easily converted into 2-dimensional sheets and possess graphene-like attributes. MOFs are basically a composition of molecular complexes formed between metal and salts, organic and inorganic molecules, (Figure 1). The interest in understanding the structures of this class of compounds dates back to the end of the 19th century when the composition of the molecular complexes formed between metal, salt, and inorganic molecules were viewed as coordination complexes with stereospecific structures [5].

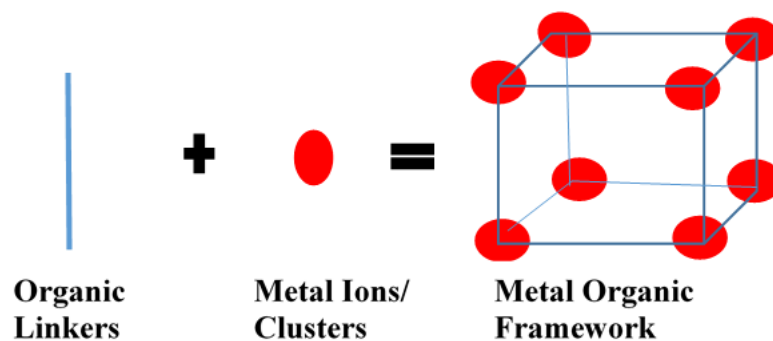


Figure 1. Illustration of metal organic framework

Transition Metal Cyanides are a unique class of MOFs worthy of considerations because they can easily be synthesized by precipitation in aqueous solution. The most common are hexacyano transition metal complexes with divalent transition metal counter ions. However, this class is 3-dimensional material and cannot be easily exfoliated into sheets. This makes it difficult to harness the 2-dimensional properties that we seek. Coincidentally, tetracyano transition metal, another group of transition metal cyanide have been studied in the past and has been predicted to have the capacity to be easily exfoliated into 2-dimensional sheet materials. In this work we prepare this class of

transition metal, exfoliate them into 2-d sheets, and experimentally validate some of the theoretical predictions of their properties and finally investigate their potential applications. For instance, molecular complexes of metal and di-metallic salts of cyanonickelate, such as square planar $[\text{Ni}(\text{CN})_4]^{2+}$, tetrahedral $[\text{Cd}(\text{CN})_4]^{2+}$ and their corresponding ligands such as ammonia, water and unidentate amine can be applied to take advantage of the characteristics of the connecting ligand, e.g. light-actuating devices ligands can be prepared with light-responsive connecting organic ligands in the framework. Just as functionalizing tetra-cyanonickelate with different cations results in 2-D materials with varying porosity, making these high porosity metal tetra-cyanonickel materials comparable to transition metal aluminosilicate (zeolites) for catalytic applications and selective filtration purposes [6].

1.2 Review of the Literature

1.2.1 Nature of Transition Metal in 3D Metal Framework

Nickel in $[\text{Ni}(\text{CN})_4]^{2-}$ exhibits square planar symmetry. In the ground state, the valence shell electronic configuration of a Ni atom is $3d^84s^2$. Nickel ions in $[\text{Ni}(\text{CN})_4]^{2-}$ have a +2 oxidation state, coordination number of 4 and $3d^84s^0$ electronic configuration. Because of the strong field from ligands such as CN^- ions, a forced pairing which counteracts Hund's rule of maximum multiplicity occurs between the 3d orbital of Ni and the donor CN^- ion, making a dsp^2 instead of sp^3 hybridization. Hence, the number of unpaired electrons in the d orbital reduces to zero in Ni (8 from the central Ni atom and 2 from the CN^-) resulting in a low spin magnetic moment, and a square planar instead of tetrahedral configuration. The Ni ion is therefore consistent with the fact that almost all

known square planar metal complexes contain a d^8 central metal ion, since 8 valence electrons can be exactly accommodated in the four reasonably stable orbitals [7].

The 3-D framework of $MNi(CN)_4$ (where M is a divalent metal transition element) results from alternating divalent metals, one having six coordination and the other four coordination numbers. With these metals adjacent to each other, they form a 3-dimensional block. The four-coordinated metal forming a square planar sheet in the two-dimensional axis, while the six-coordinated or octahedral metal forming the third dimension to form a 3-D block. Figure 2 shows a simplified representation of the octahedral and square planar position in a typical MOF as presented by Nash [8].

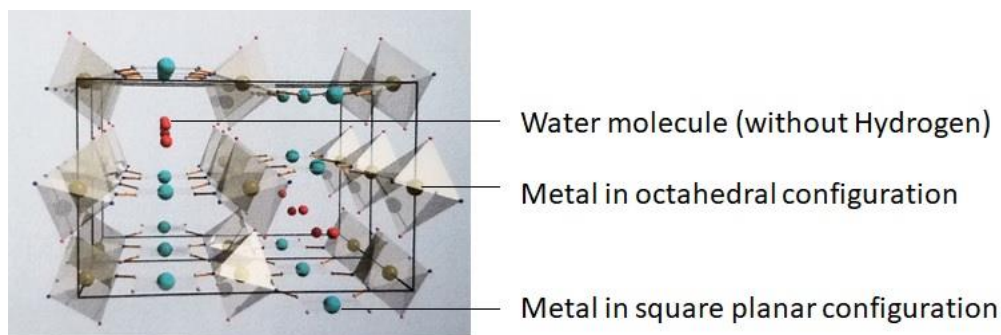


Figure 2. Representation of octahedral and square planar coordination of a typical transition metal framework. Source [8].

The blue balls in the framework represents the metals in the square planar coordination, while the yellow balls are in octahedral coordination. Water molecules (red balls) are trapped within the layers of this representation. The black lines represent the unit cell.

1.2.2 Fe, Ni, Mn and Co Transition Metal

The transition metals of concern in this study are Ni, Co, Mn and Fe. These are of interest because the electron states in their d-orbitals respond to the static electric field

produced by neighboring anions according to crystal field theory. They can also exhibit alternating planar and octahedral configuration. Table 1. shows the electronic configuration for the interested transitional metals.

Table 1. Electronic Configurations for Mn, Co, Fe and Ni Transition Metals

Electronic	Mn	Fe	Co	Ni
+2 Configuration	3d ⁵	3d ⁶	3d ⁷	3d ⁸
+3 Configuration		3d ⁵	3d ⁶	3d ⁷

The five electrons in the 3d orbitals of octahedral Mn²⁺ will not exhibit degeneracy and will not be in the same energy levels because of the effect of electrical field of neighboring ligand ions on the energies of the valence orbitals of the ions in the crystal. The energy of the 3d_{x²-y²} and 3d_{z²} (i.e. the ‘eg’ orbitals) increases much more than the energies of the other three 3d_{xy}, 3d_{yz} and 3d_{xz} (‘t_{2g}’ orbitals), because the ‘eg’ orbitals faces directly towards the ligands while the t_{2g} orbitals lie in-between the ligand field. Figure 3 depicts the conventional octahedral crystal field. This explains the octahedral behavior where there is high spin because Hund’s rule will be obeyed in filling degenerate orbitals before any other orbital in the same subshell.

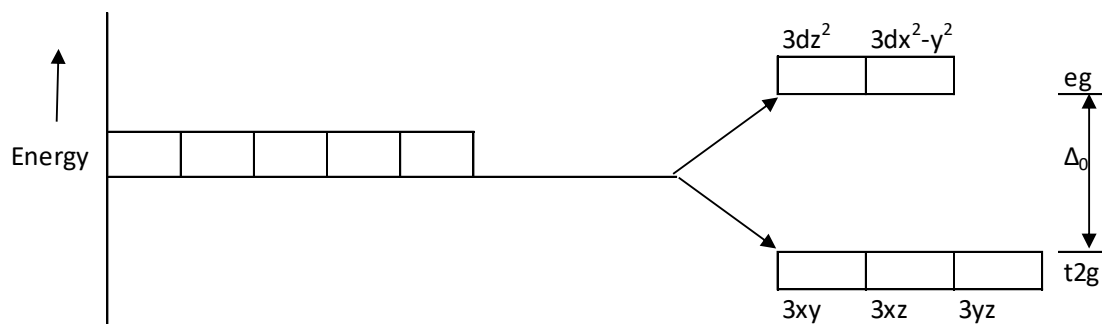


Figure 3. Octahedral crystal field splitting

For instance, in Fe^{2+} with a d^6 configuration (Figure 4), a high spin octahedral results if it takes less energy to excite the electron to 'eg' orbital.

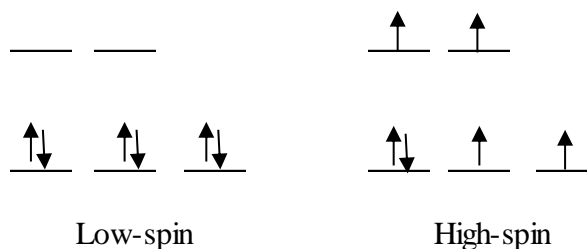


Figure 4. Low spin and high spin configuration of Fe^{2+} in $3d^6$ coordination

The square planar coordination crystal field effect decreases in the order $\text{Co}^{2+} > \text{Fe}^{3+} > \text{Fe}^{2+} > \text{Co}^{2+} > \text{Ni}^{2+} > \text{Mn}^{2+}$, from strong-field to weak-field ligands [9, 10].

1.2.3 Preceding Background Work

Prussian blue (Iron(III)-hexacyanoferrate(II)), the first modern artificially made pigments have been used for artistic work since 1724 [11]. The accidental discovery of the 3-dimensional pigment had motivated research into similar compounds, such as the family of Hoffman clathrates – chemical structures formed between two or more independent chemical species without direct or strong chemical bonds [12, 13] and consequently lots of work has been dedicated to this class of material in a bid to derive applications from their interesting structures.

Monolayers and bulk powders of Prussian blue-like network of material, that were prepared on air-water interface by Culp et al., have been shown to display unique magnetic behavior. They exhibit different magnetic behavior when thin films of the bulk material is prepared directly on solid surfaces [14, 15] . At the same time, it has been

shown that the transition metal tetracyanide material can exhibit both the square planar structure and octahedral structure in the same framework [15, 16].

1.2.3.1 Structure

Figure 5 shows that the basic structure of the 3-dimensional frameworks is built from alternating units of a divalent six-coordination transition metal center with a divalent metal in square planar or four coordination. A cyanide group forms a bridge between these centers in each of four directions. This forms a planar lattice network of squares that extend into two dimensions. The unit cell of the structure is given by assigning a and b directions to the planes that contain the atoms. The direction that runs perpendicular to these planes is assigned the c direction. Because there is no direct bonding between the metal cyanide sheets, there is a basal space or interlamellar spacing between the sheets in the c direction. The term clathrate was first used by Powell and Palin for the quinol compound $3\text{C}_6\text{H}_4(\text{OH})_2 \cdot \text{SO}_2$ [5, 17] to interpret the structure of Hofmann's benzene compound that has no direct chemical bonds between the 2-dimensional metal complex network and the benzene molecule. The concept of clathrate has since been used to show that a well-ordered chemical structure can be formed between two or more independent chemical species without direct or strong chemical bonds. Molecules occupy the basal space coordination-bonded to the two available coordination sites above and below the plane. The width of the basal space is dependent on the type and size of the molecule. This has promising application if the basal spacing can be increased and tuned to occupy molecules of interest. By tuning such spacing, the molecules of interest can be intercalated into the space and discharged from the space depending on the type of application to which it is being applied.

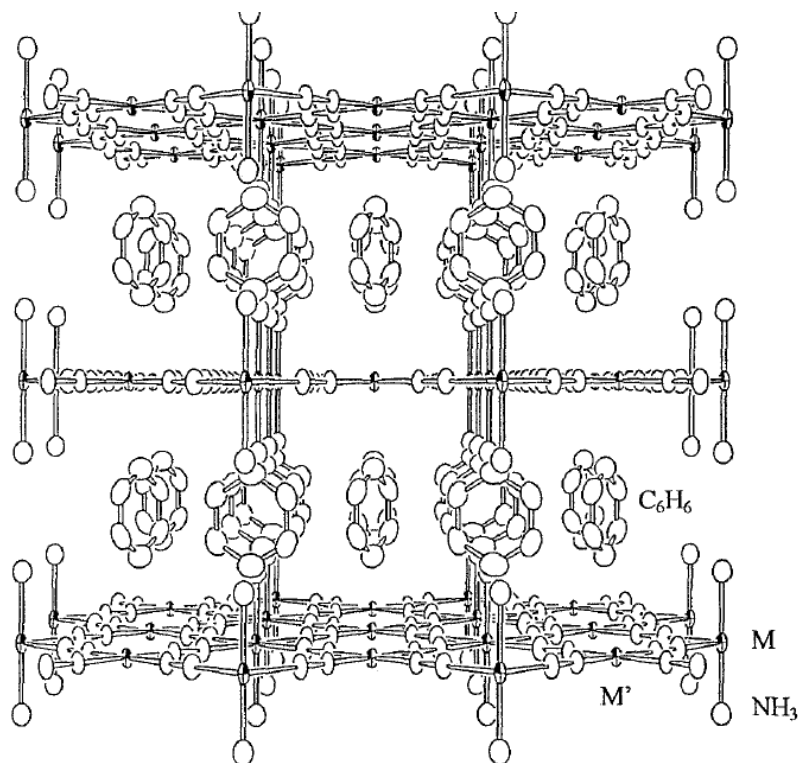


Figure 5. Generalized diagram of a Hofmann benzene clathrate.

$M(NH_3)_2M'(CN)_4 \cdot 2C_6H_6$. M at the octahedral position coordinated by two NH_3 ligands in trans positions; and M' in square planar position coordinated by four CN . In Hofmann's benzene clathrate $M=M'=Ni$. Source [5]

In Figure 5, showing a generalized form of the Hofmann-type benzene clathrate, there are two types of Ni atoms in the two-dimensional network, one in a square planar low-spin Ni^{2+} acting as the central metal coordinating with four CN in the $[Ni(CN)_4]^{2-}$. The other Ni is the octahedral high-spin Ni^{2+} coordinating with four N atoms from the four $[Ni(CN)_4]^{2-}$ formed by the previous Ni. Two N atoms from two NH_3 ligands are at trans positions. The resulting formula should be $[Ni(NH_3)_2Ni(CN)_4] \cdot 2C_6H_6$ [5].

Based on X ray diffractions data, cage structure with imprisonment of divalent metals and without the secondary NH_3 ligands in a 3-dimensional network was proposed by Keggin and Miles to represent the Prussian blue which had been a known dye and

other complexes [5, 18]. However, carefully prepared single crystals of Prussian blue by Ludi et al. shows that the water molecules were coordinated from inside the cage at sites where Keggin and Miles had proposed the presence of $[\text{Fe}^{\text{II}}(\text{CN})_6]^{4-}$, thus expanding the cage [5, 19]. The Ludi structure indicated that molecules such as water molecules, serve different roles such as ligand, fillers and stabilizers for the cubic supramolecular structure.

In the 1978 work by Beall et al., insight and understanding of the crystal structure and the color transition effect in hexacyano transition metal complex of cobalt and manganese, $\text{Co}_3[\text{Co}(\text{CN})_6]_2 \cdot 12\text{H}_2\text{O}$ and $\text{Mn}_3[\text{Co}(\text{CN})_6]_2 \cdot 12\text{H}_2\text{O}$ was determined by neutron and x-ray diffraction analysis. Prior to this time, detailed understanding of the structure of the hexacyano-compounds had been elusive and limited by available analysis tool before the time, with several explanations of their unique structures. The 3-dimensional model obtained by x-ray and neutron diffraction [20] provides a good understanding of the behavior of hydrogen-bonded H_2O structure ‘trapped’ within the structure of a hexacyano metal organic framework as well as the tetracyano transition metal counterparts.

Earlier investigations into the structure of metal tetracyanonickel by Ludi et al. had posited a distorted octahedron coordination of two water molecules and four cyanide group that make up the complex. Later understanding and neutron diffraction results suggested otherwise. The 1978 explanation of $\text{Co}_3[\text{Co}(\text{CN})_6]_2 \cdot 12\text{H}_2\text{O}$ and $\text{Mn}[\text{Co}(\text{CN})_6]_2 \cdot 12\text{H}_2\text{O}$ structures, showed that the structure consists of divalent metal ions linked to the cobalt and manganese atoms by cyanides. A better understanding of the water network molecules in the disordered network was also provided in [21]. The

explanations were substantiated by the similar results that were obtained in methanol ligands substituted species [20]. An explanation was given for the observed lattice constant change for dehydrated and hydrated structures and the presence of the two types of hydrogen bonding discussed by Brown [22] were seen as substantiating evidence in the explanation of the structure. Hence, adequate and more insightful explanations for experimental observations in the structures.

The model was found to be octahedral as against Ludi's model and the hydrogen bonding was confirmed as an important stabilizing agent for the structure. Transport for semi permeable applications is made possible by the presence of alpha-bonding properties and hydrogen bonding capability - methanol substituted complex with greater hydrogen bonding and bigger sizes diffuse through the lattice faster than smaller molecule like H₂S with lower hydrogen bond, hence hydrogen bonding is even more important than size [20]. Size sets the upper limit on size of ligands entering the lattice and charge neutrality of the complex. A clearer explanation of color transition observed in the Co complex as well as the low magnetic moment of the salts which were inadequately explained earlier by Shriver and Brown [23] was achieved. This was made possible by the improvement done by Beall et al. on the 1942 structure proposed by Miligan and Weiser [24].

1.2.3.2 Preparation and Exfoliation Approaches

An approach to obtain a square planar structure was described by Culp and co-workers, to probe into application of inorganic finite and infinite complex network in sensing, catalysis, electronic and optical functions, as well as magnetic effects related to information storage [14, 25, 26]. The approach makes use of air-water interface directly

in the fabrication of the network assembly. Interface has been shown to play a role in determining the network structure, [14, 27-29]. The surface of a liquid while helping to facilitate the diffusion of reactants also retains the structure directing character of an interface. In Figure 6, an amphiphilic pentacyanoferrate (3^+) complex confined to a monolayer on an aqueous sub phase reacts with a second divalent metal ion in the aqueous sub phase, utilizing the air–water interface. By confining one of the reactants to the air–water interface the propagation of the structure in the third dimension is prevented, resulting in a planar network at the water surface. The final structure of the network is a square rigid array, resulting from linear geometry of the cyanide bridge and the bond angles of the octahedral metal complexes. An amorphous colloidal product resulted when the same reaction was done in homogeneous mixture. This illustrates the ability of an interface to direct the structure of the network. This approach makes 2-dimensional complexes whose properties can be harnessed as a family of molecule–based magnets. Structural and material properties can also be harnessed by the convenience of utilizing Langmuir–Blodgett technique to transfer the assembly network to solid supports [14, 30-33].

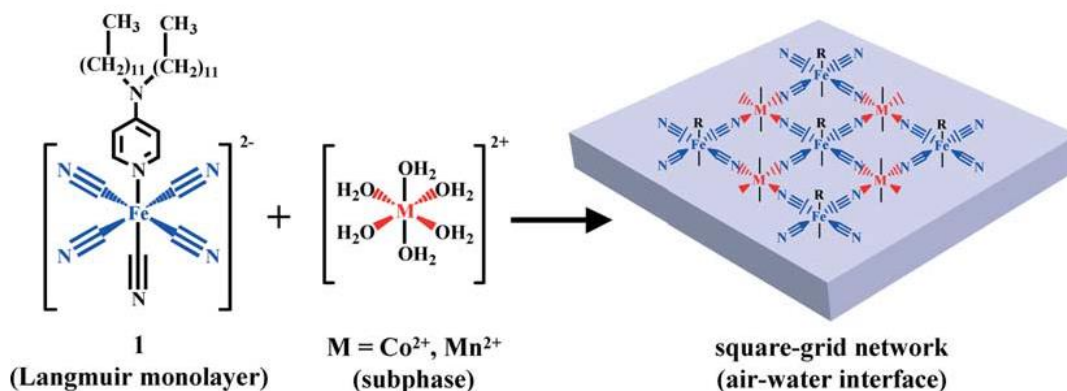


Figure 6. Assembly of two-dimensional grid networks at the air-water interface. Source [14]

Preparation techniques such as slow release of the cyanometallic group, can cause the cyanide ion to act as terminal group in a hydrothermal synthesis of cyano-bridge network. Studies showed that the cyanide source can also affect the coordination of the cyanide anions [34]. For $\text{Cd}(\text{CN})_2$, it has been predicted that the most favorable configuration is $\text{MC}_2\text{N}_2\text{--MC}_2\text{N}_2$ (where M= divalent transition metal) whereas three possible configurations are near almost equally favorable for $(\text{CN})_2$ [35]. Origin of magnetic anisotropy studies suggested by Quan and Cheng-Lin Luo gathered that the magnetic anisotropy observed in Molybdenum substituted cobalt (II) is due to the unsymmetrical distribution of the methanol ligands surrounding the Cobalt (II) [36]. Nash et al. described an exfoliation technique that can also be utilized to harness the 2-dimensional structure (Figure 7). The 3-D to 2-D is made possible by using dodecyl pyrrolidone (DDP) to separate the 3-D network into sheets with increased interplanar space due to the long carbon chain in of DDP. Subsequently, the ligands separating the sheets can be removed by heat treatment. Thus, freely existing long range single sheets dehydrated (M(II)-Nickel(II) cyanide-bridged network can be obtained. In their method, Nash et al. showed that the DDP was used to push apart and exfoliate individual

nanosheets of various $MNi(CN)_4$ compound, this has also been reported earlier by Beall and Goss for Montmorillonite [37].

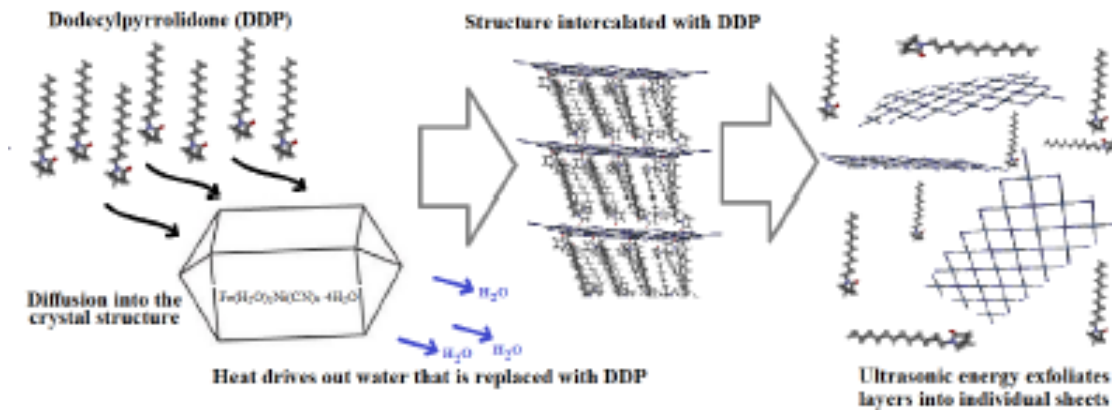


Figure 7. Simplified mechanism for exfoliation of 3D structures into 2D sheets. Source [15]

Theoretical calculations using density function theory (DFT) are usually employed for predicting the ground state configuration and behavior of this class of compounds and has been used successfully to predict the properties of the dehydrated monolayers of $MNi(CN)_4$. Nash et al. proposed synthesis for the preparation of $M(H)_2Ni(CN)_4 \cdot 4H_2O$ compounds where M are the metal ions such as Ti, V, Cr, Mn, Co, Cu, and Zn which can replace the nickel ions bonded to nitrogen. The changes in the bond length between the metals which results from the substitution at the octahedral site and the nitrogen of the cyanide can be used to correlate the variation in the lattice constant [5].

The build-up to this dissertation includes the work done by Tyler Nash and Marcus Goss. In 2014, Nash et al. predicted the electronic band structure and density of states of some transition metal tetracyano nickelate complexes (including V, Cr, Mn, Fe, Co etc.). The results of their density functional theory for predicting the magnetic

behavior suggest that Mn and Fe have higher magnetic susceptibility. Ab-initio simulation was successfully used to theoretically predict the bond lengths of C-N, Ni-N and Ni-C and compared with experimental samples of dehydrated and hydrated samples of $\text{FeNi}(\text{CN})_4$ [38, 39]. Nash also worked on the application of 2-D transition metal cyanide bridge for an ultralow platinum group catalyst [8].

Goss predicted using the crystal data from Nash et al. and molecular modeling using Accelrys® inc. Cerius², to compare water permeability between graphene sheets and the 2-D sheets of $\text{FeNi}(\text{CN})_4$. His results showed that water is impermeable in pristine graphene while it is permeable in the cyanide bridge. Goss also provided a qualitative prediction that a sheet of $\text{FeNi}(\text{CN})_4$ will selectively reject Na^+ ions in saline solution. The mechanism posited was that the water molecules reorient themselves while moving through the pore space, while Na^+ is rejected on a size basis. In addition, their results suggest that the chloride ion is strongly attracted to the transition metal atoms and does not move through the pore, while the amount of Na^+ ion that bridge the pore increases with the concentration of the solution. This current work is predicated on these theoretical predictions.

1.2.4 Potential Applications

1.2.4.1 Magnetic

Molecular level magnetic behavior is identical to bulk magnetic behavior found in materials like transition metal, electromagnets, and rare earth metals. Ferromagnetic behavior of $\text{Mn}_3[\text{Fe}(\text{CN})_6]_2$ and $\text{Co}_3[\text{Fe}(\text{CN})_6]_2$ at low-temperature [14] has been reported. Figures 8a and b shows the magnetic behavior of Fe-Co film and Fe-Mn film. In the two films, the cyanide ligand mediates the magnetic exchange.

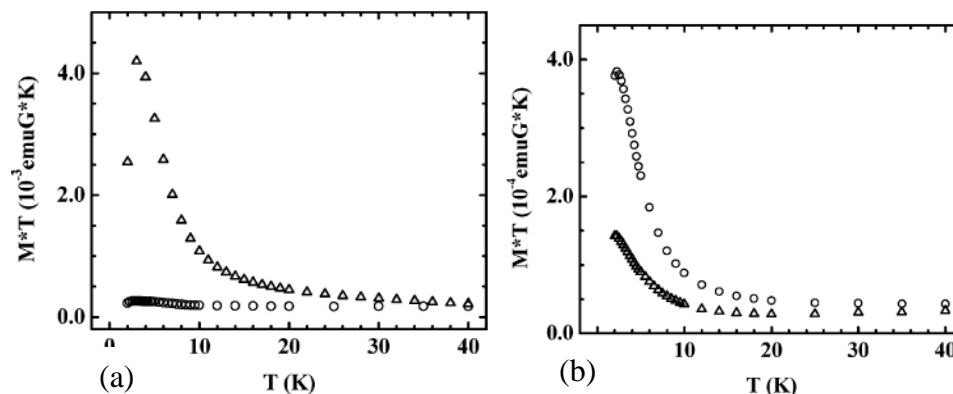


Figure 8. (a) Temperature dependence of the product of the zero-field cooled magnetization (measured in 20 G) and temperature for a 100 bilayer (per side) sample of the Fe-Co network on Mylar showing the anisotropy of the magnetic response when the field is applied parallel to the sample surface (Δ) and perpendicular to the sample surface (o). (b) The temperature dependence of the product of the zero-field cooled magnetization (measured in 20 G) and temperature for a 125 bilayer (per side) sample of the Fe-Mn network on Mylar showing the anisotropy of the magnetic response when the field is applied perpendicular to the sample surface (o) and parallel to the sample surface (Δ). Source[14]

Unlike conventional metallic magnets, the metal atoms containing d or f shell electrons don't have to be adjacent to one another. The atoms containing unpaired electrons can be separated by other atoms or organic moieties [15, 40]. Transition metals which have unpaired electrons in the d shell serve as magnetic centers which can be separated by cyano ligand bridges. The distance between the magnetic centers as mediated by the cyanide bridge influences the effectiveness of magnetic coupling and the bulk magnetic moment [16]. If the distance between the transition metals can be manipulated, the stability of para and di-magnetic phases can be tuned or controlled. Thermodynamics dictates the competing high and low spin state. Molecular switches and molecular magnetic memory devices are viable commercial applications of these properties [15, 16, 41]. In this work we report the magnetic behavior of the transition

metal cyanide complexes and the hybrid cyanometal complexes using vibration sample magnetometer analysis.

1.2.4.2 Molecular Sieve

Transition cyanometallate networks can be applied as ultrathin molecular sieves in gas purification, ion selective, reaction buffer, and reverse osmosis membranes. Unlike conventional membranes utilizing thin film composite, e.g. polyamide-polyethersulphone composite for water desalination via reverse osmosis, ultrathin cyano-metal networks present atomistically thin benefit - with lower material and energy cost [15]. Antifouling advantages are also possible with metal tetracyanonickelate networks. 2-D cyano-bridged transition metal nanosheet frameworks provide a maximum pore density and atomistic thickness which are necessary for permeability and support for ultrathin molecular membranes. This is unlike graphene sheets and carbon nanotubes models, where there is a tradeoff between mechanical strength and permeability due to inclusion of pores which increases permeability but reduces strength [42-45]. Considerations in designing, selecting, and explaining water permeability and ion rejection in ultrathin molecular sieves include; pore size exclusion, charge repulsion, dehydration effects on the cage structure around ionic species, specific pore interactions (like biological channel mechanisms), interactions of solutes with the pore's chemical structure, and entropic differences [46].

1.3 Dissertation Effort and Research Objectives

The aim of the research was to validate previous DFT calculations using experimental methods, SEM, X-ray diffraction, VSM and other analysis tools. The aim also included using other divalent metals in the preparation of the tetracyanonickelate

complexes other than the relatively well-known divalent metals. In addition, we aimed to investigate the opportunities and application presented by hybrid metal tetracyanonickelate. We aimed to increase the interlamellar spacing of the complex and seek means of tuning the basal spacing to suit various applications. We also wanted to seek additional ligands that can serve to block the coordination sites and the basal spacing with useful applications.

Lastly, we investigated the application of these cyanometallate complexes for ultrathin molecular sieves for water remediation and gas purification. In previous work by Goss and co-worker [12], a 2-dimensional nanosheet was speculated for cyanide-bridge transition complex based on the orientation and structure. It was postulated that the opening within the matrix of the 2-D material (approximately 0.3 nm) (Figure 9) can be utilized for porous media filtration, desalination and separation applications. In this work, we present a novel preparatory method for microporous media activated with the desalination potentials presented in Goss's work. To the best of the author's knowledge no such approach has been used to utilize the class of MOF's in the proposed applications.

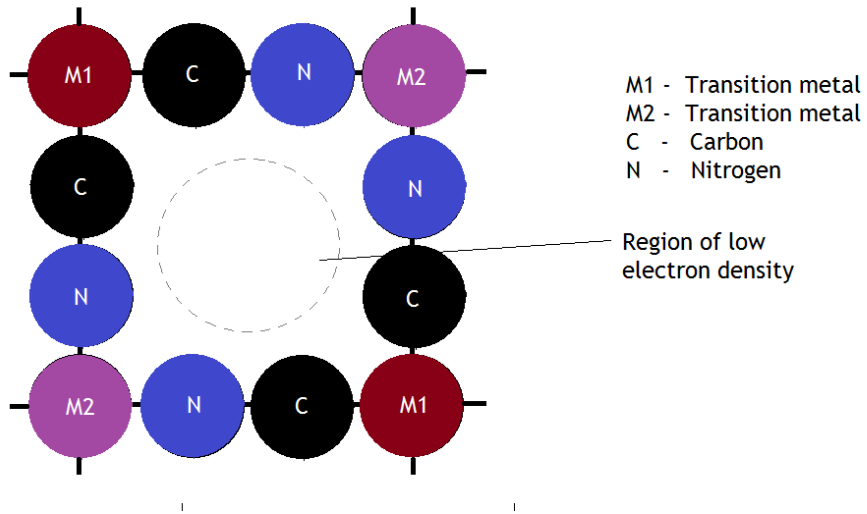
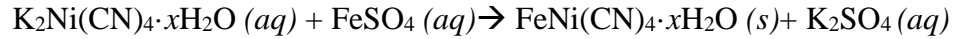


Figure 9. Diagram showing square framework of atoms in a single layer. The framework creates a small opening between atomic radii that water molecules can move through. The circles shown are not to scale. Source [15]

2. EXPERIMENTAL METHODS

2.1 Preparation of Divalent Transition Metal Powder Complexes

Powder samples of Fe substituted in the $K_2Ni(CN)_4 \cdot xH_2O$ were prepared according to Nash et al. [39]. Powder sample of iron complex was precipitated as follows: 8.1409 g of Fe salt (iron (II) ammonium sulphate, from Scholar Chemistry) was dissolved in 50 ml of distilled water. 5.0183 g of potassium tetracyanonickelate (II) hydrate obtained from Aldrich was also dissolved in 50 ml of DI water. The two solutions form equimolar with respect to Fe and K when mixed.



The resulting mixture was mechanically stirred for 16 hours. The solution was centrifuged using Thermofisher Sorval LYNX6000 centrifuge for Fiberlite F14-6X250Y Rotor at a g-force of 10000g and approximately 8000 rpm at 25 °C for 15 minutes. It was decanted and rinsed with distilled water. The centrifuging and rinsing process were repeated three times to remove any excess salts.

The process was repeated for equimolar solution of Mn^{2+} (manganese II chloride, Aldrich), Co^{2+} (cobalt II chloride hexahydrate, 98%, Sigma-Aldrich), and Ni^{2+} (nickel II sulphate hexahydrate, 99% ACS Reagents) in $K_2Ni(CN)_4 \cdot xH_2O$ as follows;

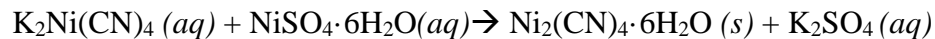
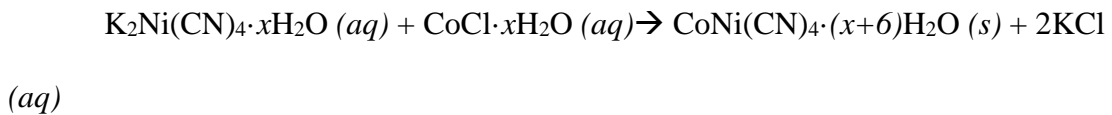
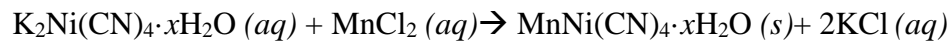


Table 2. Weight of potassium tetracyanonickelate complex and corresponding weight of transition metal salt

	Mass of $K_2Ni(CN)_4 \cdot xH_2O$ (g)	Equimolar Mass of Transition Metal Salt (g)
Fe:K ₂	8.1409	5.0183
Mn:K ₂	5.0138	9.5725
Co:K ₂	5.0183	5.0745
Ni:K ₂	5.4637	5.0408

The resulting powder were dried at 60°C in the oven for 24 hours. Figures 10a-d shows the resulting powder samples.

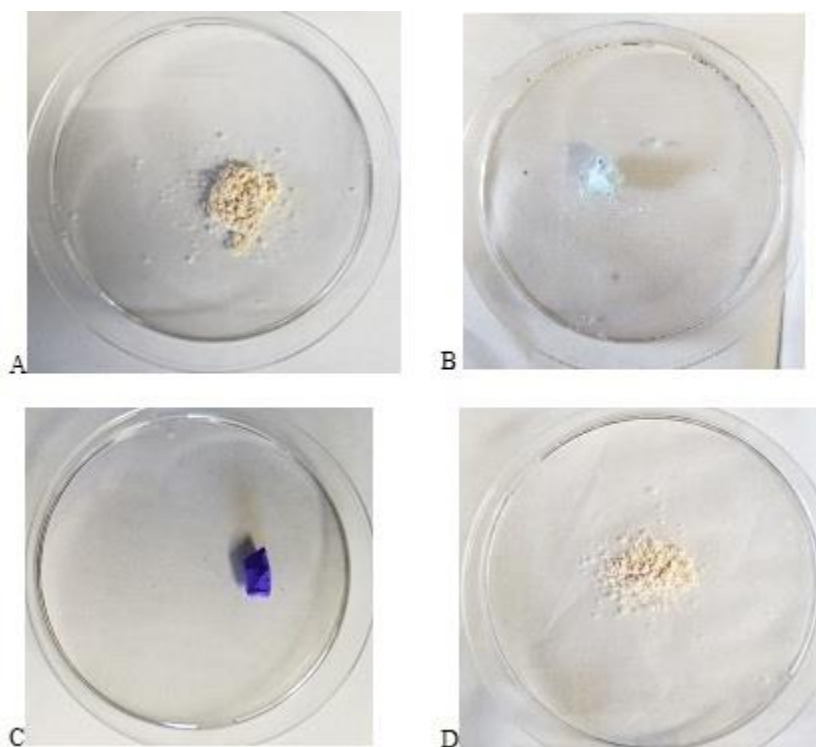


Figure 10. Powder samples of $MNi(CN)_4$. Where M is (a) Fe, (b) Ni, (c) Co and (d) Mn

2.1.1 Treatment of samples with DDP

The powder complexes were divided into two parts. One half was kept for analysis, while the other halves were treated with Dodecyl Pyrolidinone (DDP). DDP was added to the samples in a glass vial until saturated. The resulting mixtures were placed in oven and heated until 185°C. Ramping took 3 hours, after which the temperature was kept at 185°C for 1 hour. The temperature was dropped to 85°C and kept at the temperature for 24 hours. Co and Ni samples were completely dried. While Mn requires a little more time. It was kept for additional 5 hours until completely dried. Fe sample remained wet but had expanded drastically that the glass vial was broken. The sample was thereafter heated in petri dish and allowed to dry for 1 more hour at 185°C.

2.1.2 Preparation of Powder Complex for SEM Imaging

SEM images were obtained by dispersing 2-8 mg of the powder samples in 10-20 ml of ethyl alcohol and sonicated for 20-40 minutes to obtain an even dispersion. 1-2 drops of the sonicated samples were deposited on a silicon wafer. The silicon wafers had been cleaned overnight in a 50/150 ml mixture of H₂O₂/H₂SO₄ and washed several times and dried. The wafer was dried in air for 12 hours and SEM images were obtained.

SEM images of the samples were obtained using JEOL JSM –6010 PLUS/LA. It is worthy of note that because of the magnetic charging of the samples, it is difficult to obtain images at high voltages, and at immersion modes. Powder samples were initially collected for imaging, but the extreme charging make this impossible. Hence the samples were prepared on Si wafer for imaging. Field free images were obtained at 5 kV and 86 pA settings for most imaging.

2.1.3 X-Ray Diffraction Analysis

Approximately 0.5 g of respective samples were grounded in mortar to obtain fine distribution of powder. The resulting powder were analyzed using Bruker D8 X-ray diffraction equipment.

2.1.4 Thermo Graph Analysis

The TGA analysis was done on the powder samples at constant heating rate (*b*) of 10°C/Min up 800°C under 40 ml/min argon purge and 60 ml/min TGA run analysis using TA instrument TGA Q50 V6.7.

2.1.5 Raman Scattering

Insight into the nature of the bonds was done with Raman inelastic scattering of light. The shift in the wavelength that corresponds with to the vibrational/rotational modes of the powder complexes were compared with different reference sources and reported. Thermo Scientific Raman equipment with Omnic Spectra analyzer was used. The following settings was utilized for sample analysis; laser wavelength of 532 nm, 2.0 mW of 10 mW maximum laser power, aperture of 50 µm pinhole, 900 lines/mm laser grating and 50X objective lens.

2.1.6 Transmission Electron Microscopy

Sample preparation for TEM analysis was done by dispersing 1-2 mg of samples in 10 ml of ethanol and sonicating for 20 minutes at ambient temperature. The dispersed solution was immediately transferred onto the coated side of a holey carbon film TEM Grid HC300-Cu 300 mesh by Electron Microscopy Science. The analysis was done using JEOL 2010F High Resolution Field Emission TEM using acceleration voltage of 200 kV.

2.1.7 Vibrating Sample Magnetometry

VSM analysis was done in order to experimentally determine magnetic hysteresis loop behaviors of the powder samples before and after treatment with DDP.

Approximately 50 mg of the powder complexes were measured, filled into a threaded boron powder VSM cup. The cup was attached to the quartz rod sample holder. The hysteresis loop measurement was done using Microsense Easy VSM, with maximum applied field of 15000 Oe. VSM analysis was done for empty boron nitride cup, the signal was subtracted as background from the main sample signals, all measurements were done at ambient temperature.

2.2. Divalent Transition Metal Growth Method on Microporous Membranes

Growth was done by placing 1.0 micron polytetrafluoroethylene (Teflon, PTFE), as barrier between desired transition metal salt of the complex and potassium tetracyano nickelate as shown in Figure 11.

Two elbow glasses were connected using pinch clamps such that the membrane support was placed between the two glasses. The connection was made water tight by applying grease on the edge of the adjoining glass. So that solvent cannot pass through the joining points. Equimolar samples of desired salts were prepared; 1.6246 g of desired metal ($\text{Fe}(\text{NH}_4)\text{SO}_4$) was dissolved in DI water to make 10 ml of aqueous salt solution. Also 0.9999 g of potassium tetracyano nickel salts was dissolved in DI water to make 10 ml of solution. After complete mixing and dissolution, the two solutions were administered into the opposite's sides of the set-up in Figure 11 using pipets. The set up was left at ambient temperature for 24 hrs. Afterwards, there was a solvent migration and reaction at the PTFE interface, resulting in the formation of desired metal complex by diffusion of

the opposing solution in the Teflon support. The resulting PTFE support was removed from the set-up, gently rinsed several times and dried in oven at 50°C. The membrane was dried and used as barrier for Na⁺ ion selectivity test.

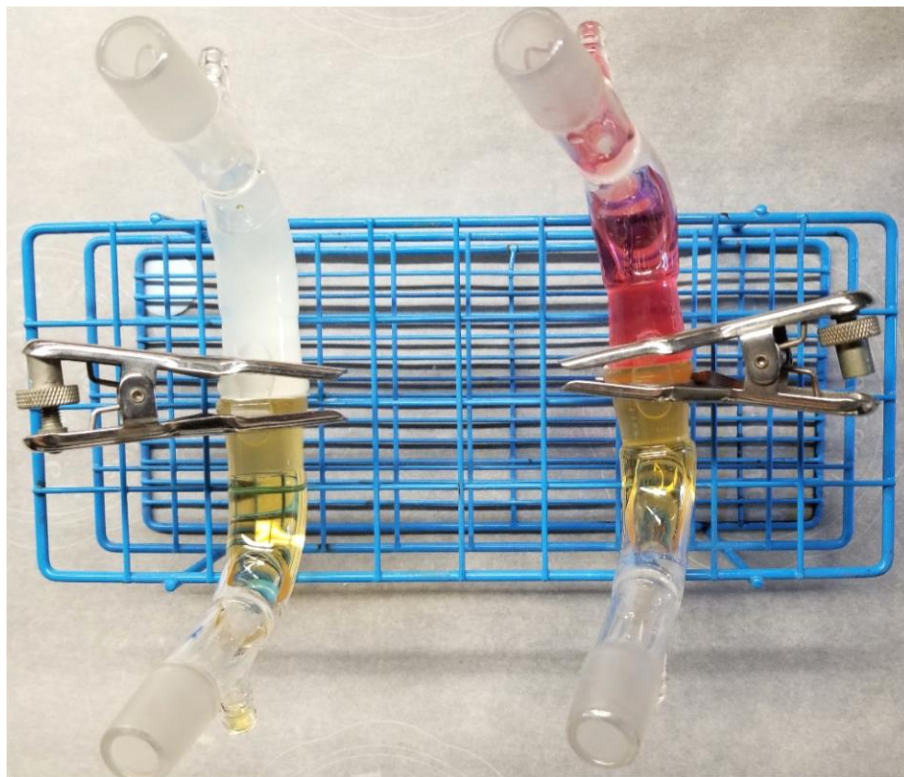


Figure 11. Growth method for metal CN network

Also, in the same manner, equimolar solution of other transition metal salts was prepared, and the experiments were repeated. 1.0043 g of MnCl₂ salt in 10 ml of its solution was prepared along with side 1.9155 g of KNi(CN)₄ in 10 ml of solution. Nickel (II) sulphate (1.0945 g in 10 ml solution) with 1.0056 g of KNi(CN)₄ in 10 ml water. 1.0020 g of CoCl₂·6H₂O alongside 1.0162 g of K₂Ni(CN)₄ both in 10 ml of aqueous solution.

Three different types of microporous membranes were considered for the experiments. These are; 1.0 micron 25 mm PTFE unlaminated hydrophilic membrane, from Sterlitech Corporation, 5.0 micron 90 mm, PTFE unlaminated hydrophobic membrane from Sterlitech Corporation and 0.45 micron 25 mm cellulose nitrate membrane from Micro Filtration Systems. Achieving microporous growth in the unlaminated hydrophobic Teflon requires prior treatment in ethanol to make it hydrophilic. This was done by soaking the Teflon in ethanol until it is completely wet. The Teflon was then dried in air before usage. There was no change observed via the hydrophobic membrane, so the experimental set-up was then placed in oven at 75°C. Little growth was then achieved via this membrane. The cellulose membrane interferes with the growth reaction and it was consequently rejected. The experiments with 1.0 micron hydrophilic PTFE membranes was done at ambient temperature without any need for elevated temperatures. The hydrophilic membrane yields a consistent and even growth across all the considered transition metal and was consequently used.

Separate set of filters were also produced by further treatment of the impregnated dried filters with DDP. This was done by placing the already impregnated filters in a petri dish, drops of DDP was added until saturated. This was kept at ambient for 1 hour to ensure complete saturation of filters. The resulting DDP saturated filter was then transferred to a hot plate under fume cupboard and heated at 185°C until all DDP is completely evaporated and dried. The resulting filters were also used for Na⁺ selective test.

2.2.1 Na Ion Selectivity

The test was carried out by preparing 1.0 Molar NaCl solution. The NaCl solution was administered into an elbow glass which had been connected to an Erlenmeyer flask with a side arm. The filter was placed between the elbow glass and the Erlenmeyer flask, it was held in place by a pinch clamp. The system was connected to a Welsh 1399 DuoSeal vacuum pump as shown in Figure 12. The experiment was performed for all filters including a pristine filter which acted as control experiment.



Figure 12. NaCl filtration set-up with vacuum pump

Filtration was initiated by setting the pump to 0.01-0.03 MPa for most of the filters. The system was watched closely to avoid caving in of the filter papers. Most of media were able to filter without vacuum assistance after initiation. Pressure drop could also be initiated by carefully controlling and running water tap through the Erlenmeyer flask with side arm as shown in Figure 13.

The water samples were collected and further analysis for Na ion was done. 0.001, 0.002, 0.005, 0.01, 0.02, 0.05 and 0.100 M standard solutions of NaCl were prepared to compare and correct an already calibrate Hanna Edge Instrument for percentage sodium chloride. The test was done by placing the ion probe in the water samples and held until constant reading was obtained. The electric conductivity, percentage NaCl, and total dissolved solid were obtained alongside the temperatures. The amount of Na ion in the filtered water samples were subsequently determined by averaging results from five trials.

In other to compare the filtration effect of the membrane with reverse osmosis (RO), an experiment was performed where only 20 % of the concentrated solution was allowed to pass through the membrane impregnated with Iron tetracyanonickelate (II). This was done by administering 10-15 ml of the concentrated salt solution into the filtering set-up, but only 2 ml of the filtered sample was collected and analyzed. Unlike the previous case where the whole 10-15 ml solution was allowed to pass through. This approach mimics RO process where about 10-20 % of the solution is filtered through the membrane and the rest of the stream is recycled in a continuous process. The result is presented in chapter 3.



Figure 13. NaCl filtration set-up with tap to maintain differential pressure

An initial variant of the complexes was prepared in the presence of 1,4, benzene-dimethanol. This was achieved as follows: equimolar amounts of the potassium tetracyanonickelate (II) hydrate obtained from Aldrich and respective salts of Mn (Manganese (II) Chloride, Aldrich), Cd (Cadmium Chloride hydrate, 99%, Alfa Aesar), Co (Cobalt (II) Chloride hexahydrate, 98%, Sigma-Aldrich), Fe (Iron (II) Ammonium Sulphate, Scholar Chemistry) were obtained. 10 ml of deionized water was added to the equimolar amount of Potassium tetracyanonickelate, 10 ml of deionized water was used to prepare solution of the salts in the presence of 10 ml of 1,4 benzene dimethanol. The precipitate was treated according to the previous preparation, in Nash et al. The resulting complex were obtained, washed and dried. The sampled were then treated with DDP and kept in oven at 185°C for 1 hour and for 24 hours.

An initial attempt that was set-up for filtering NaCl solution and produce water using powder samples of transition metal complex is presented in Figure 14. In the set-up, a thin layer of dried powder sample was pressed into thin cake and was placed on a filter paper supported by sintered glass microfilter. The system was held in place by pinch clamp to ensure no solution escape on the adjoining points. Produce water and 1.0 M NaCl solution was gently administered into the system and allowed to filter under gravity. The filtered water samples were also collected in glass vial and analyzed. It was difficult to make any judgement from the results due to the disturbance on the cake while administering the water. Appendix 2 shows the results from these initial attempts before the membrane method was fully developed.



Figure 14. Figure showing filtration set-up for powdered samples supported on filter paper-supported sintered glass

3. RESULTS AND DISCUSSIONS

3.1 FeNi(CN)₄ and Derivative

This section discusses the results obtained from the analysis of FeNi(CN)₄ before and after exfoliation with DDP.

3.1.1 X-Ray Diffraction

The X-ray diffraction pattern for FeNi(CN)₄ before and after exfoliation in DDP is presented in Figure 15.

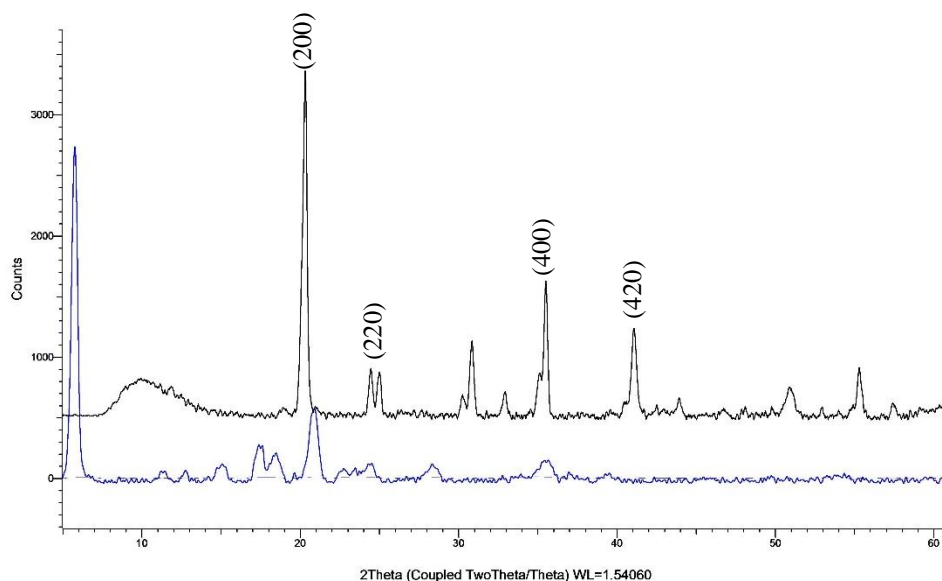


Figure 15. X-ray diffraction pattern for FeNi(CN)₄ before (black lines) and after exfoliation in DDP (blue lines)

Similar x-ray patterns shown in Figure 16 have been reported by Zhang et al for the zinc substituted specie of tetracyanonickelate (II) complex, which resulted from the removal of a CN group from an electroplating waste stream.

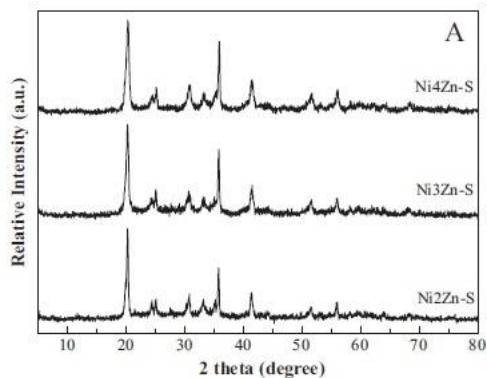


Figure 16. Similar X-ray diffraction pattern from literature for Zn substituted specie Source [47]

From the result obtained in Figure 15, it was observed that the major peak at 2-theta of 20.284° , with a d-spacing of 0.4374 nm corresponds to the 002 plane [39]. There is a shift of the peak to 5.767° after exfoliation with DDP. This corresponds to a d-spacing of 1.5324 nm, hence we observed a significant increase in the d spacing judging from the XRD. The mean particle size for the material was obtained from the Scherrer equation by obtaining the FWHM. A mean particle size of 23.92 nm was obtained using Scherrer equation and the FWHM of the peak (Figure 17 and Table 3).

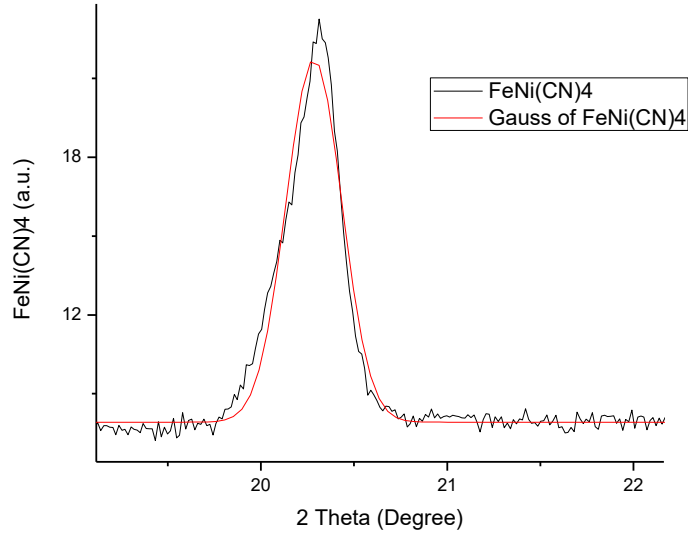


Figure 17. FWHM of Fe(CN)₄ for obtaining mean particle size

Table 3. FWHM for calculating nanosize particle

Adj. R-Square	0.97265		
		Value	Standard Error
FeNi(CN) ₄	y0	7.92013	0.03446
FeNi(CN) ₄	Xc	20.28461	0.00199
FeNi(CN) ₄	Sigma	0.1497	
FeNi(CN) ₄	FWHM	0.35253	
FeNi(CN) ₄	Height	13.80802	

$$\tau = \frac{K \lambda}{\beta \cos \theta} = \frac{0.9 * 0.15418}{\left(0.35253 * \frac{2\pi}{360}\right) * (\cos 20.28461)} = 23.92 \text{ nm}$$

Where; τ is the mean size of the ordered (crystalline) domains, which may be smaller or equal to the grain size, K is a dimensionless shape factor, with a value close to

unity. The shape factor has a typical value of about 0.9, λ is the X-ray wavelength, (1.5418 nm for Cu-K-alpha), β is the line broadening at half the maximum intensity (FWHM), and θ is the Bragg angle.

3.1.2 SEM and EDAX for Fe Transition Metal Complex

Figures 18(a-d) shows the SEM images of $\text{FeNi}(\text{CN})_4$, as prepared before treatment with DDP. Figure 18(b) reveals the stacks of the layered material at 65000 magnification. The structure has several layers. However, these layers are locked in place and although the sheet layers seem to obvious, they are not separated in out into single sheets. As discuss they seem to be held in place by the inter-planar intermolecular and hydrogen bond in the complex [20].

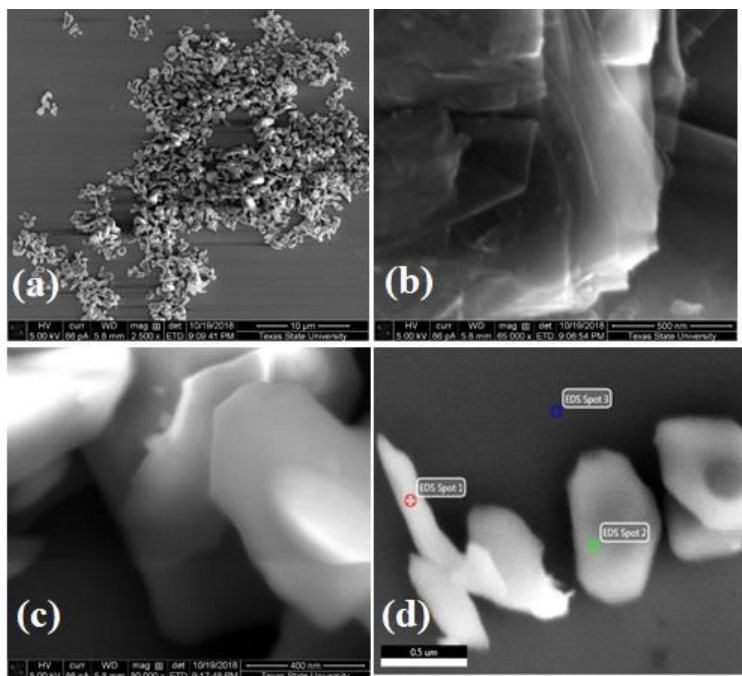


Figure 18. SEM images of $\text{FeNi}(\text{CN})_4$ at (a) 2500x, (b) 65000x, (c) 80000x and (d) spots mapped for EDAX

Figures 19a-c shows the Energy Dispersive X-ray spectroscopy of the different spots marked in Figure 18d. Figures 19a and b maps spots 1 and 2 in Figure 18d, they contain weight percent of the different constituents, there is between 7-11% by weight of Fe. Spot 3 is mapping the Si substrate on which the transition metal complex was deposited.

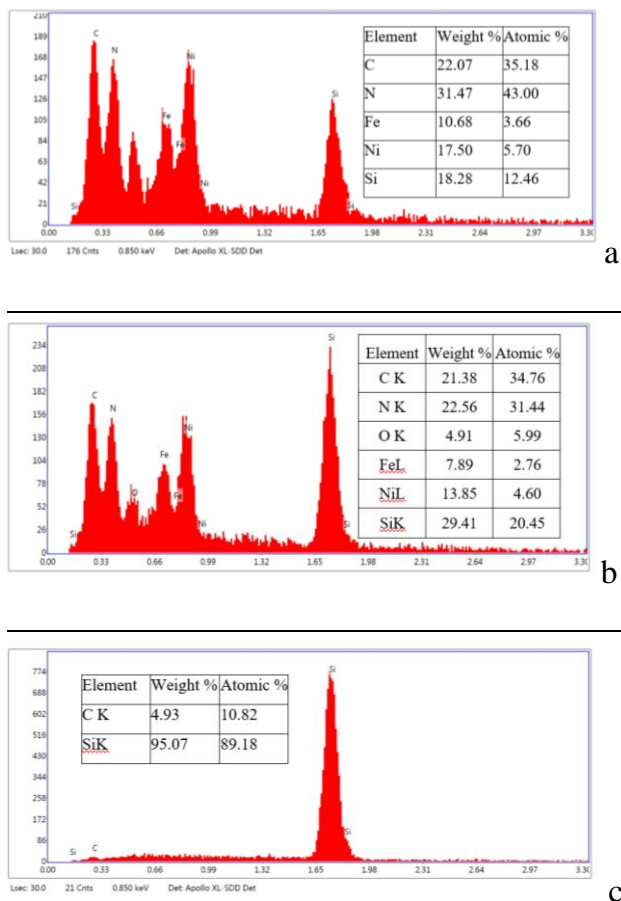


Figure 19. EDAX for images of $\text{FeNi}(\text{CN})_4$

After DDP was used to exfoliate the Fe complex, the images obtained shows the single layers that were separated out of the bulk materials. Figures 20a-c reveals the single layers sheets and the Figure 20d shows the spots mapped for EDAX analysis.

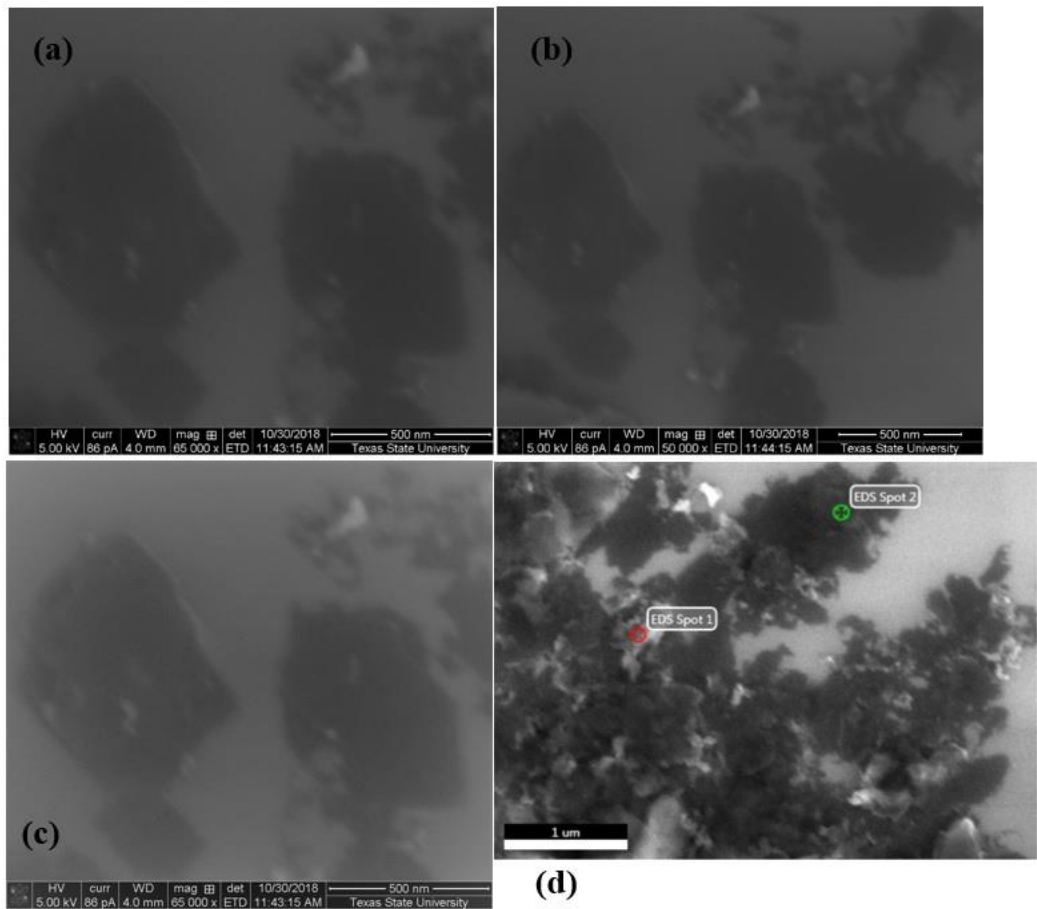


Figure 20. SEM Images of FeNi(CN)₄ after exfoliation in DDP at (a)65000x, (b)50000x, (c) enhanced picture of 65000x and (d) spots mapped for EDAX

The corresponding EDAX for mapped spots 1 and 2 is shown in Figures 21a and b, respectively. The silicon substrate peak is very pronounced due to the thin monolayer of the exfoliated single sheet. Ni, Fe and CN and O peaks that make up the structure are found in the EDAX peaks.

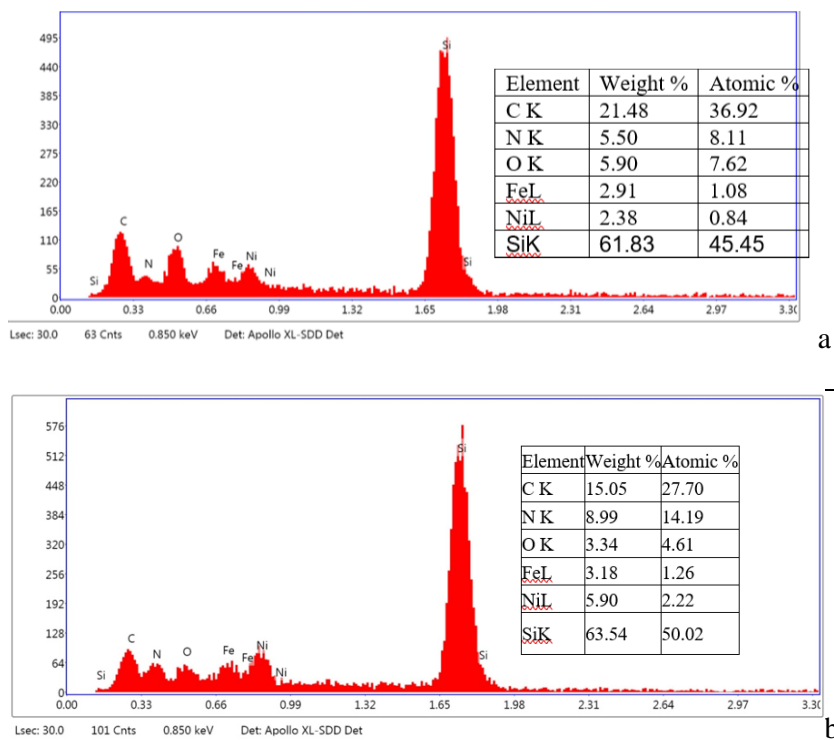


Figure 21. EDAX for Images of $\text{FeNi}(\text{CN})_4$ after treatment with DDP

3.1.3 TEM Imaging for the Fe Transition Metal Complex

The TEM images obtained from the $\text{FeNi}(\text{CN})_4$ powder complex deposited on a holey carbon TEM grid is shown in Figures 22a&b and Figures 23a&b shows the electron diffraction pattern of the sample.

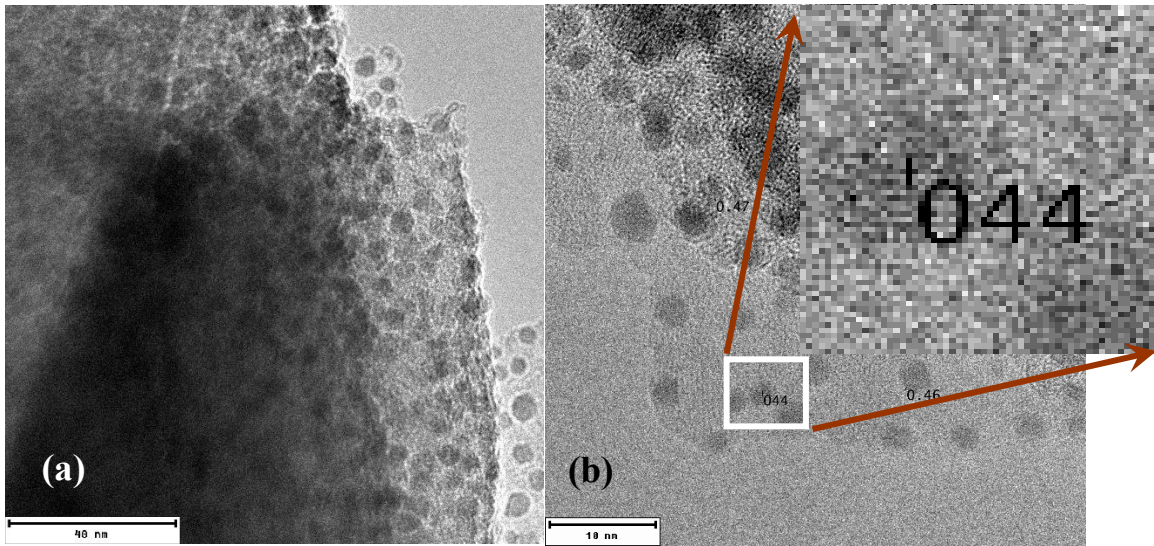


Figure 22. Transmission electron images at (a) 40 nm and (b) 10 nm of the $\text{FeNi}(\text{CN})_4$, revealing multilayer structure of the sample.

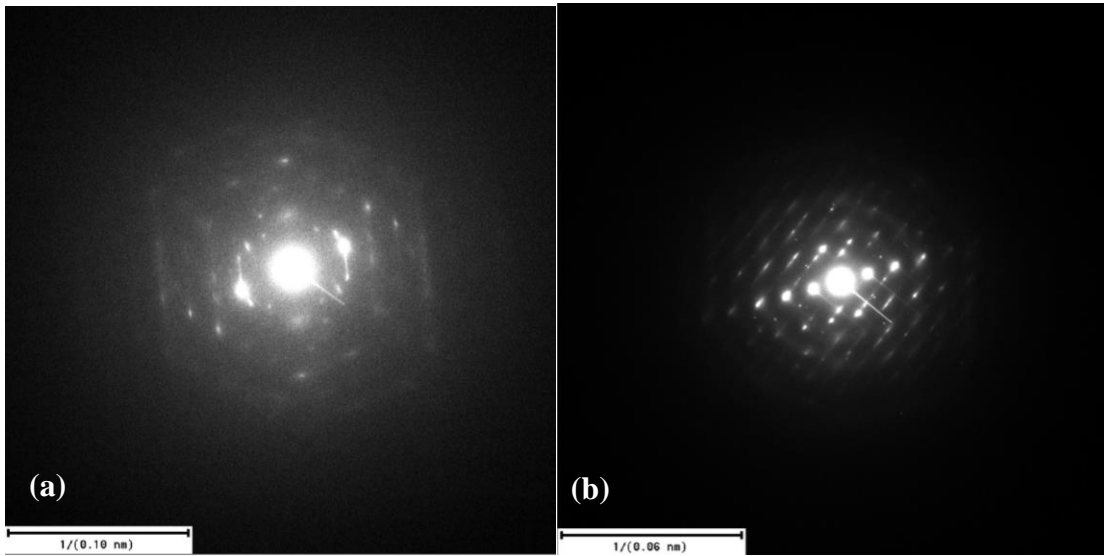


Figure 23. Electron diffraction pattern of the $\text{FeNi}(\text{CN})_4$. The diffraction suggests the quality of the periodicity of the lattice is hampered by the diffraction from underlying layers of the sheet sample. Causing diffraction from more than one layer of the sample.

The TEM images reveal there are more than one layer of the $\text{FeNi}(\text{CN})_4$ sheet.

The interplanar spacing obtained from the three locations (Figure 22b) on the TEM are 0.44, 0.46 and 0.47 nm giving an average of 0.46 nm d-spacing. This is comparable to 0.4374 nm that is obtained in section 3.1 for $\text{FeNi}(\text{CN})_4$ 200 plane. The diffraction

pattern reveals crystallinity and the presence of periodic lattice fringes, the quality of which have been reduced by the presence of additional underlying sheets contributing to the diffraction, revealing bright and dim spots representing surface and lower layers in the diffraction.

By comparing the above images with the $\text{FeNi}(\text{CN})_4$ that had been treated with DDP as seen in the TEM images in Figures 24a&b; we observe a long range single layer of the $\text{FeNi}(\text{CN})_4$ sheet. The diffraction pattern of Figures 25a&b also show well defined diffraction pattern of a single layered sheet.

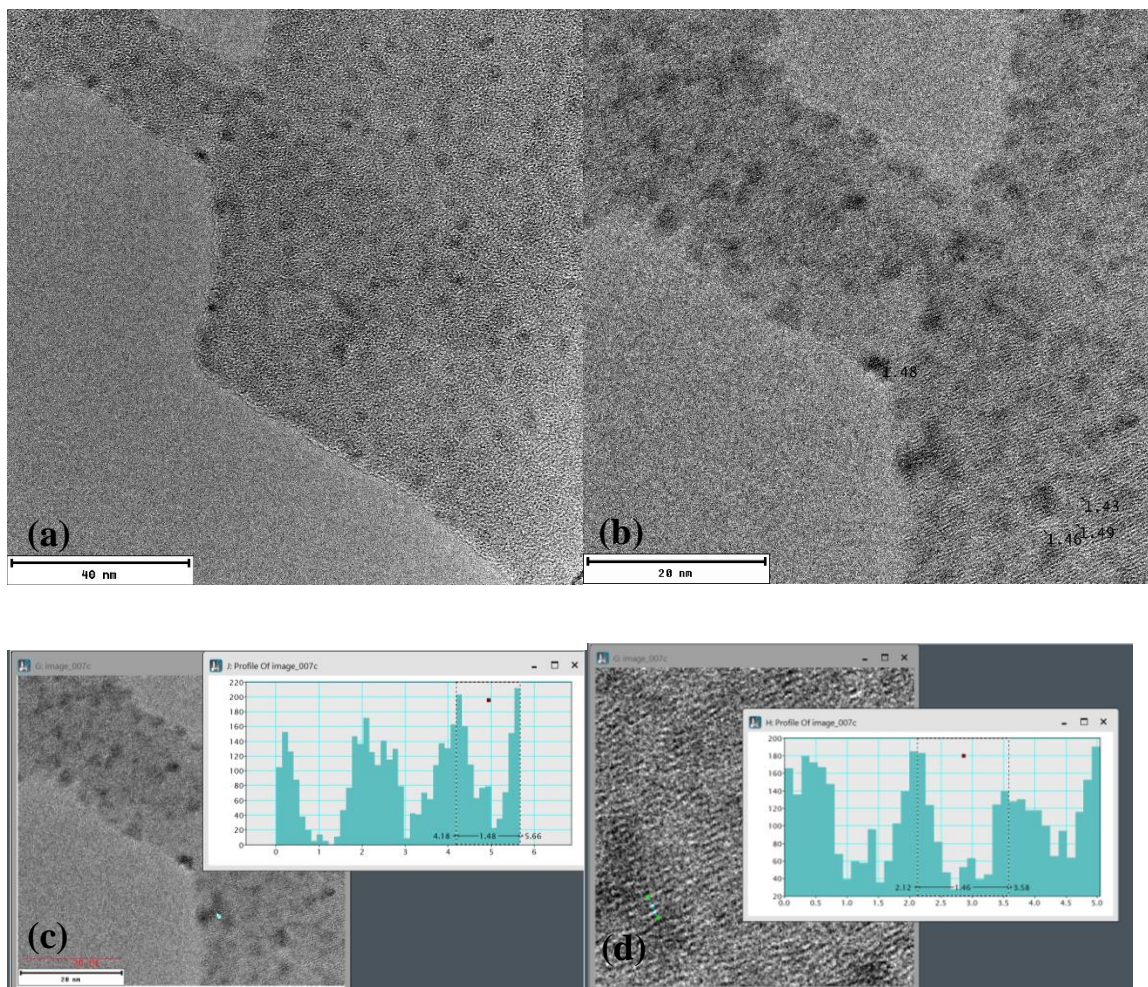


Figure 24. TEM images of $\text{FeNi}(\text{CN})_4$ after treatment with DDP (a) 40 nm, (b) 20 nm, revealing single standing sheets of sample

The d-spacing obtained from four different locations in Figure 24b are 1.46, 1.43, 1.49, and 1.46 nm giving an average d-spacing of 1.46 nm. This result is comparable to the 1.533 nm that is obtained from the X-ray diffraction data for the 200 plane in section 3.1.1. In addition, a profile of the measurement using a calibrated digital micrograph, from Gatan, (GMS 3) is shown in Figures 24c&d, the profile shows two d-spacings of 1.46 and 1.48 nm respectively. This supports results from the two earlier measurements.

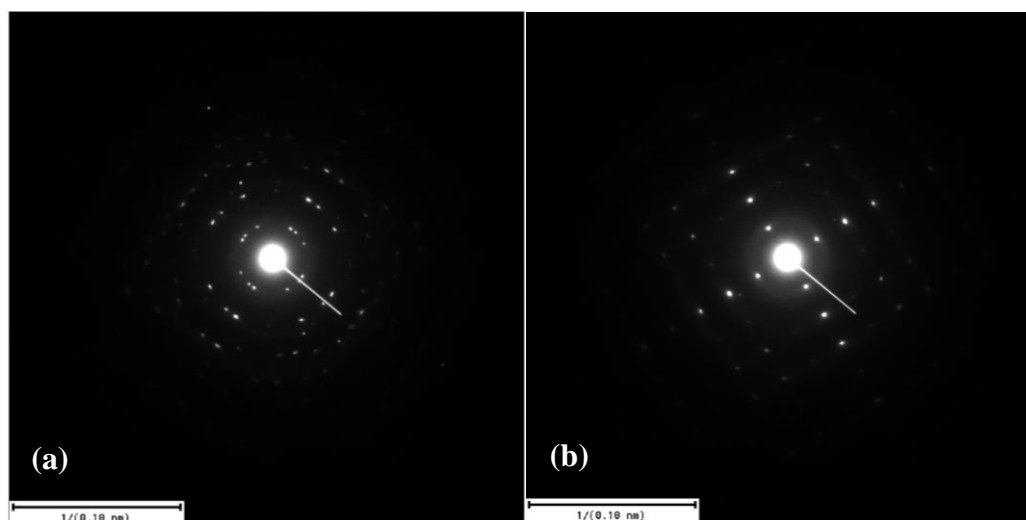


Figure 25. Electron diffraction pattern of $\text{FeNi}(\text{CN})_4$ after treatment with DDP (a and b). Distinct well-ordered patterns reveal singly standing sheets

3.1.4 Raman Scattering for Fe Transition Metal Complex

The Raman scattering for the $\text{FeNi}(\text{CN})_4$ powder before exfoliation in DDP is presented in Figures 26.

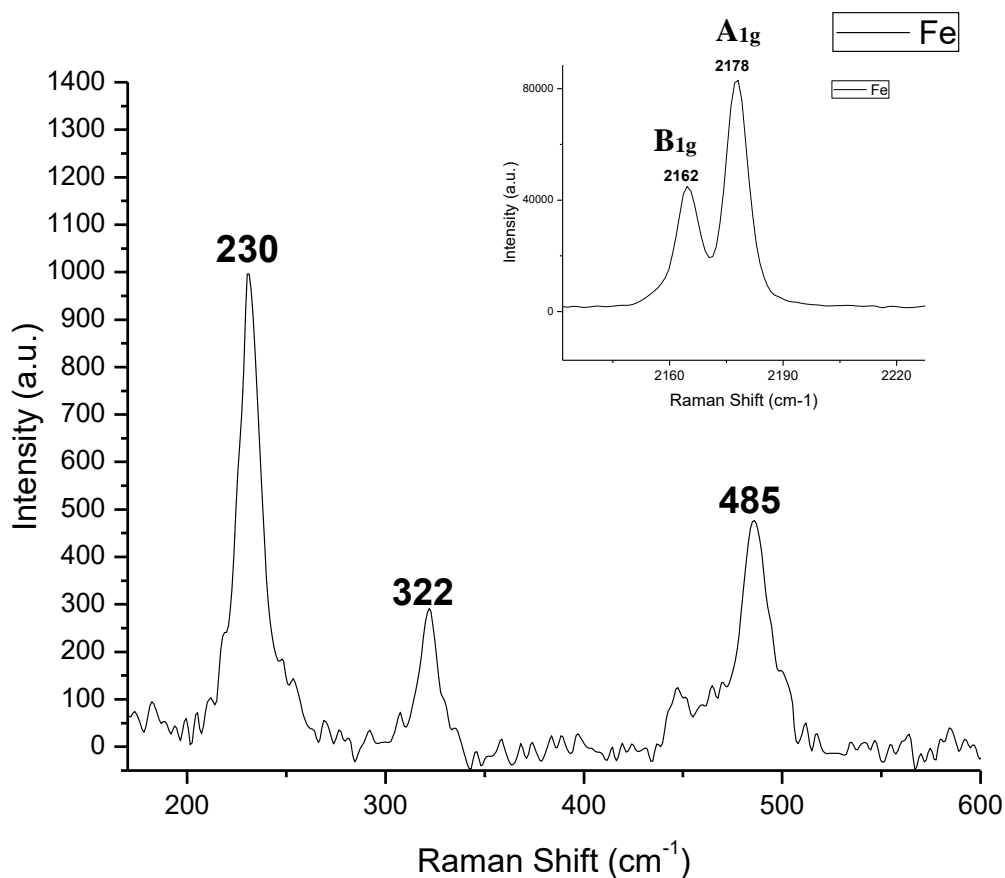


Figure 26. Raman spectra in the 150-600 cm^{-1} region, inset shows the prominent CN ‘B_{1g}’ and ‘A_{1g}’ spectra in the 2100-2300 cm^{-1} region.

The most prominent Raman peaks for the Fe complex occur at wavenumbers 2162 and 2178 cm^{-1} shown in the inset in Figure 26. These peaks have been assigned ‘B_{1g}’ and ‘A_{1g}’ stretching vibrational modes of the C≡N bonds respectively. These stretching vibrations are attributed to the $\nu(\text{CN})$ vibrational wavenumbers found in Hoffman-type Clathrate. The presence of the two band indicate that the square planar layered structure of the $[\text{Ni}(\text{CN})_4]^{2-}$ been preserved [48]. In addition, Strong surface interactions in solution containing CN^- has been reported to result in single sharp non-resonance Raman scattering at 2080 cm^{-1} and broad peak up to 2171 cm^{-1} [49, 50]. The bands at 322/485 cm^{-1} has been identified to correspond to CN-Fe-NC bond. The origin

of this bound ligand spectra had been considered by Sanghwa et al. and thought to arise from the isotropic shift pattern in either linear or bent Fe-CN bond [51]. This suggest that Fe center may be flexible to re-orient itself to accommodate external ligands and enclathrate molecules [52]. The sharp peak observed at 230cm^{-1} corresponds to the ‘ A_{1g} ’ stretching of the octahedral site of the central Fe atom [53].

3.1.5 TGA for Fe Transition Metal Complex

TGA for the $\text{FeNi}(\text{CN})_4$ is shown in Figures 27a&b for before and after DDP exfoliation respectively. It reveals onset at 96.7°C and 343°C . The first weight loss of 15% suggest that some water of hydration trapped in the interplanar space was lost between 96.7°C through 125°C . The 15% loss can be related to three water molecules lost in the Fe complex, a close call to a theoretical value of 18%. The second weight loss onset at 343°C through 354°C . About 55.5% of the total weight or 26.8% of the remaining weight from the first transition was lost during this phase. The transition represents the decomposition of the Fe complex. In Figure 27b, the onset temperature after treatment with DDP is 202°C through 248°C . 45% reduction in weight is attributed to the loss of remaining DDP in the sample. Degradation of the sample occur at 348°C , until 25% wt of the starting material was left remaining.

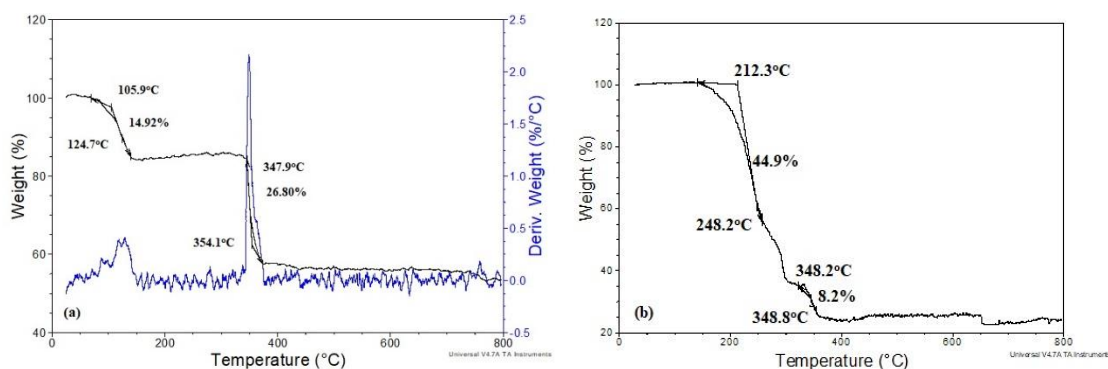


Figure 27. TGA. Analysis for Fe samples (a) before and (b) after exfoliation with DDP

3.1.6 VSM for Fe Transition Metal Complex

Figure 28 shows the hysteresis loop of the Fe samples obtained from VSM measurements at room temperature. The hysteresis indicates that the synthesized Fe complex before exfoliation has a saturation magnetization = 0.1428 emu/g. The coercivity, which is a measure of reduction in magnetic sensitivity (H_c) is 270.476 Oe. The magnetization remanence, which is the magnetic memory of the material (M at $H=0$) is 0.03836 emu/g while the squareness ($S = M_r/M_s$) equals 0.267. The low saturation magnetization agrees with the experimental observation by Goss et al. in their experiment of the Fe complex suspension in close proximity with a permanent magnet. The even number d-electron is either diamagnetic or anti ferromagnetic as predicted by Nash et al. After exfoliation with DDP, there is only a slight difference in the VSM responses. A slightly lower saturation magnetization of 0.1299 emu/g is obtained. A coercive field (H_c) of 319.059 Oe, and remanent magnetization (M at $H=0$) of 0.03604 emu/g are obtained, while the squareness ($S = M_r/M_s$) is equal to 0.275. The slight reduction in magnetic saturation may be due to the presence of trace DDP which may cover the crystals, thus shielding and reducing the magnetic saturation measurements.

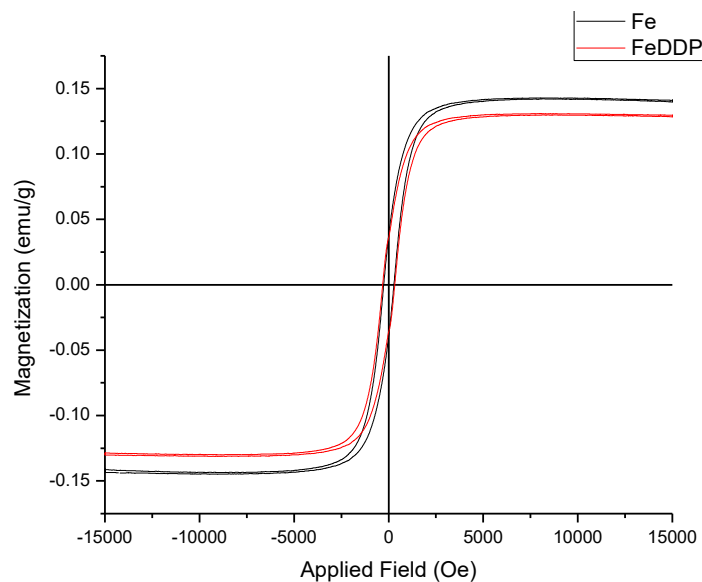


Figure 28. Magnetic hysteresis loop for Fe complexes

3.2 MnNi(CN)₄ and Derivative

This section discusses the results obtained from the analysis of the MnNi(CN)₄ before and after exfoliation with DDP.

3.2.1 X-Ray Diffraction

Figure 29 shows the XRD pattern for Mn transition metal complex before and after exfoliation with DDP. Similarly, there is an increase in the d-spacing, a shift of the peak to the left after exfoliation. The major peak for the unexfoliated Mn complex is at 2-theta of 19.838° (0.4472 nm), while the major peak after exfoliation is found at a 2-theta of 5.686° (1.5530 nm)

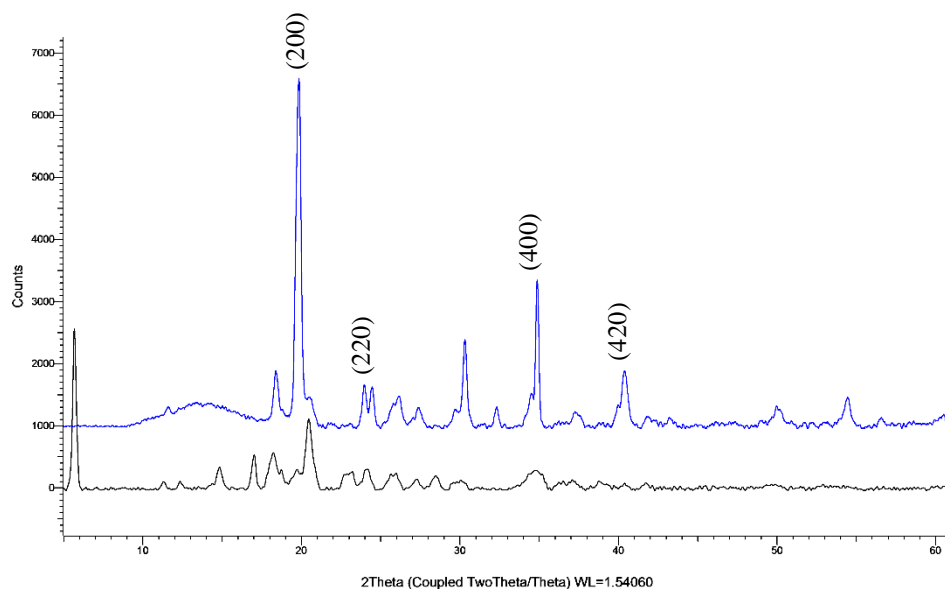


Figure 29. X-ray diffraction pattern for the $\text{MnNi}(\text{CN})_4$ before (blue line) and after exfoliation in DDP (black line)

3.2.2 SEM and EDAX for Mn Transition Metal Complex

Figures 30(a-d) shows the SEM images of the as prepared $\text{MnNi}(\text{CN})_4$, before treatment with DDP. Figure 30(b) reveals the stacks of the layered material at 150000x magnification. The structure has several layers. However, these layers are locked in place and not separated into sheets by the hydrogen bond in the complex.

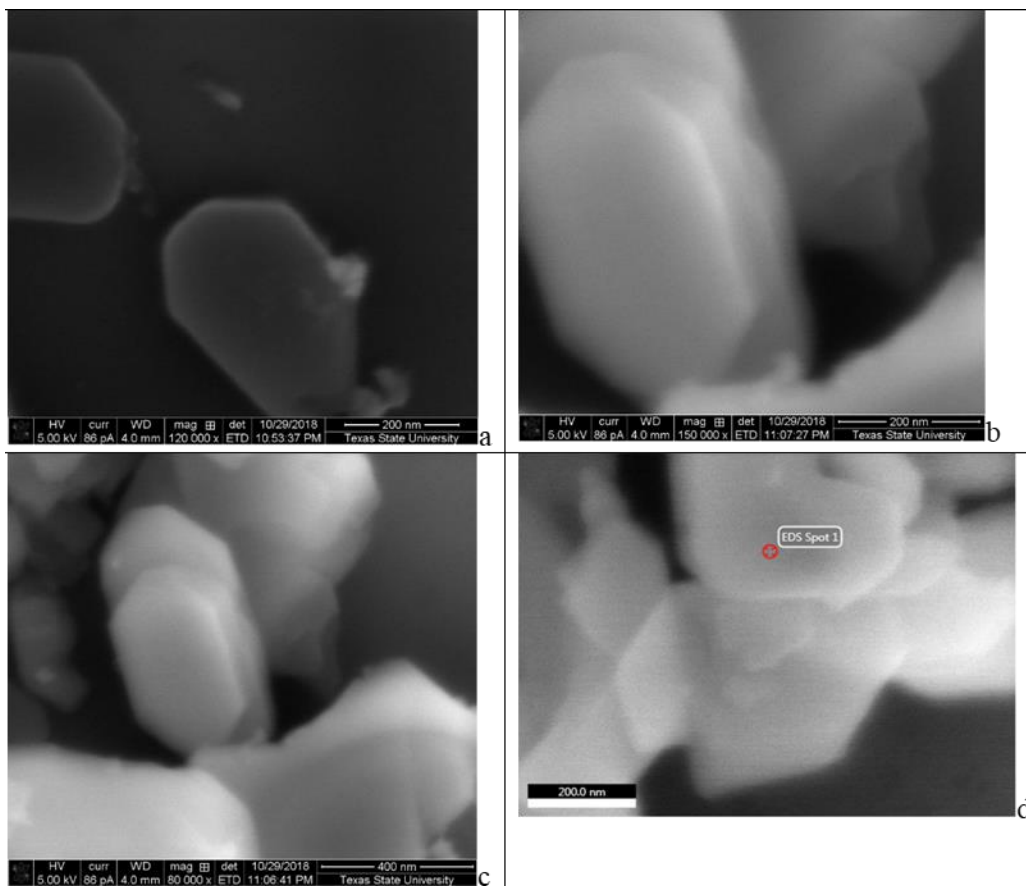


Figure 30. SEM Images of MnNi(CN)_4 at (a)120000x, (b)150000x, (c) 80000x and (d) spot mapped for EDAX.

The EDAX is shown in Figure 31, the structure contains 9.14% Mn, and other elements making up the structure, i.e. Ni, C and N. The corresponding weight percentage is also shown in the Figure.

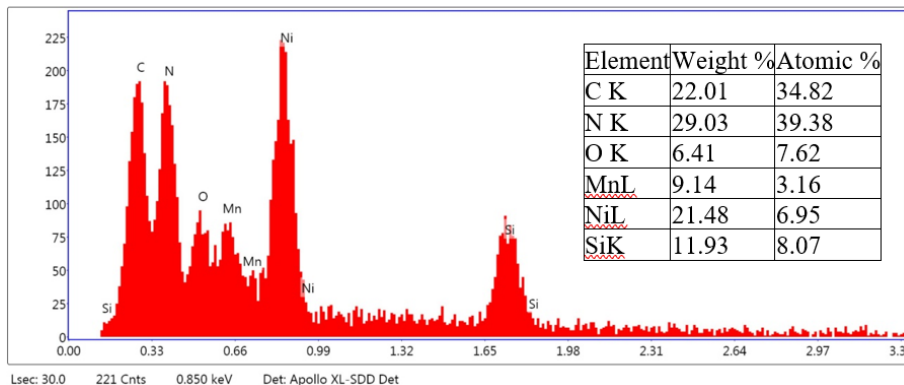


Figure 31. EDAX for Images of MnNi(CN)_4

It was very difficult to obtain a good SEM images after the sample have been exfoliated in DDP because of the magnetic charging even at low acceleration voltages. Hence the TEM images were taken and analyzed.

3.2.3 TEM Imaging for Mn Transition Metal Complex

Figures 32a&b shows the TEM images of Mn powder complex before it was treated with DDP. The profile of the image in Figure 32a shows a d-spacing of 0.445 and 0.443 nm averaging 0.444 nm as shown in Figure 32c. The x-ray diffraction calculations earlier for the unexfoliated sample show a d-spacing 0.4472 nm.

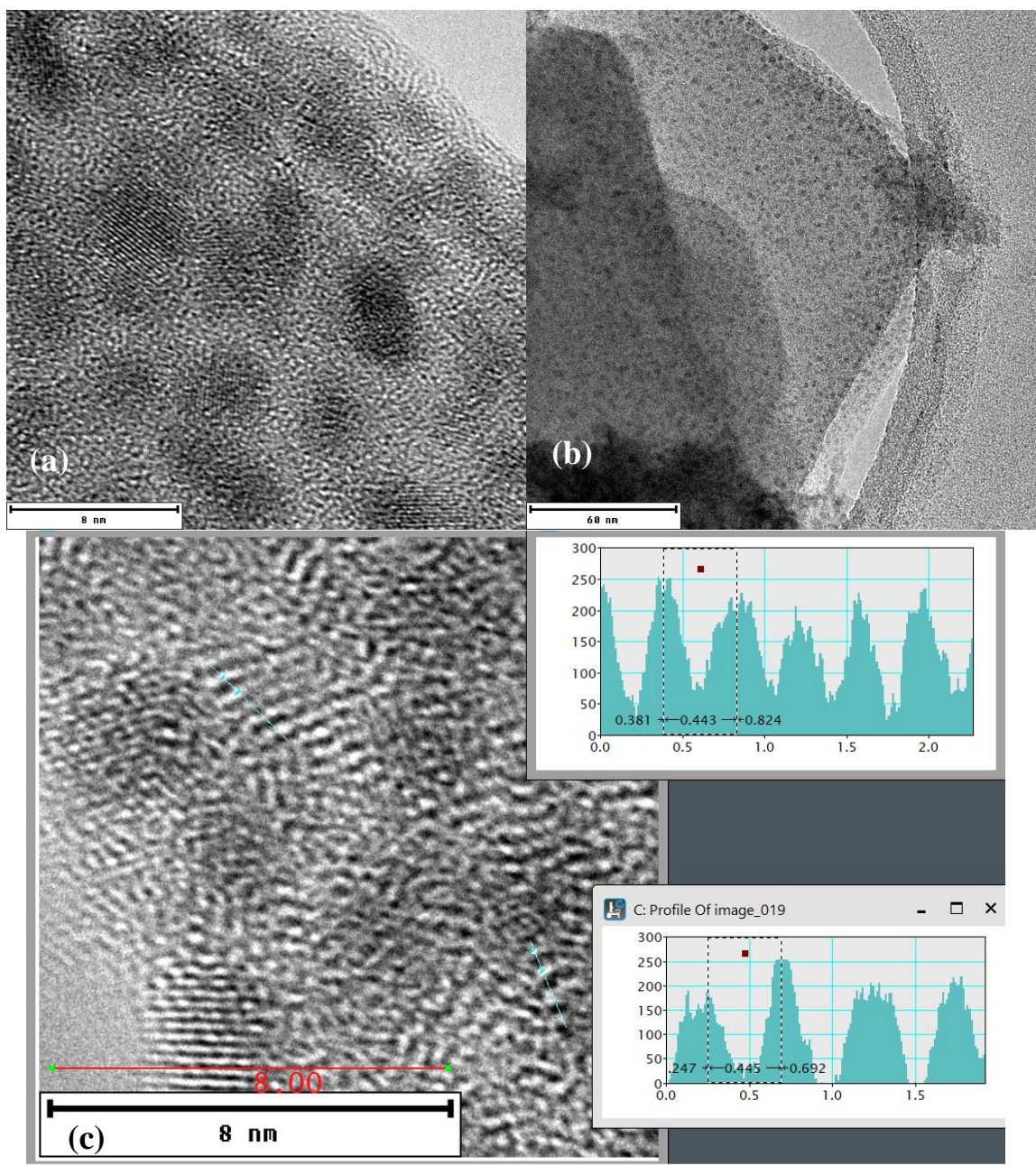


Figure 32. Transmission electron images at (a) 8 nm and (b) 60 nm of MnNi(CN)₄, revealing multilayer structure of the sample.

The diffraction pattern in Figure 33, suggests the quality of the periodicity of the lattice is hampered by the diffraction from underlying layers of the sheet sample making

it seem like an amorphous material. Causing diffraction from more than one layer of the sample.

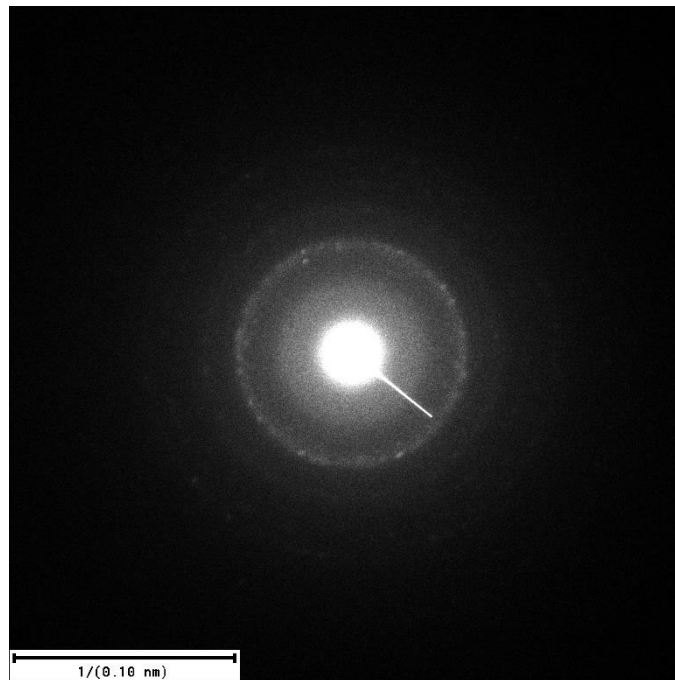


Figure 33. Electron diffraction pattern of $\text{MnNi}(\text{CN})_4$.

The TEM images and diffraction patterns obtained after exfoliation in DDP is shown in Figures 34 to 36.

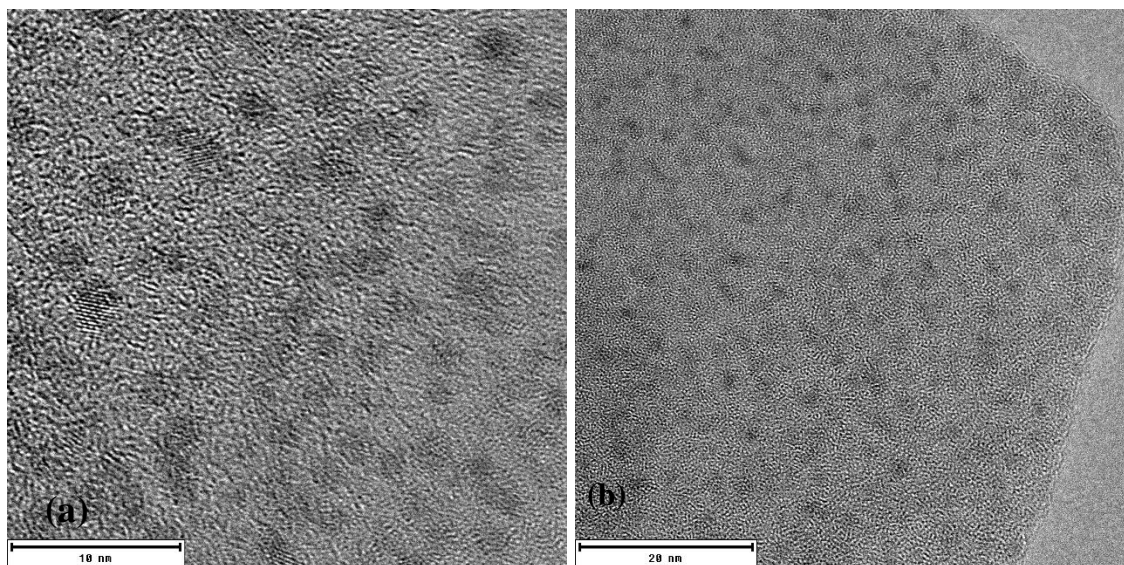


Figure 34. TEM images of MnNi(CN)_4 after treatment with DDP (a) 10 nm, (b) 20 nm, revealing single standing sheets of sample.

Analysis of the TEM images show three distinct group of d-spacing as shown in Figure 35a&b; the first group 1.653 and 1.693 nm averages 1.628 nm which corresponds to the d-spacing of 1.5543 nm obtained from the x-ray diffraction data in section 3.2.1. The second group has a d-spacing of and 0.8688 nm, and the last has d-spacing about 0.512 nm. The latter two are thought of as a d-spacing expansion transitioning phase, and some unexfoliated phase.

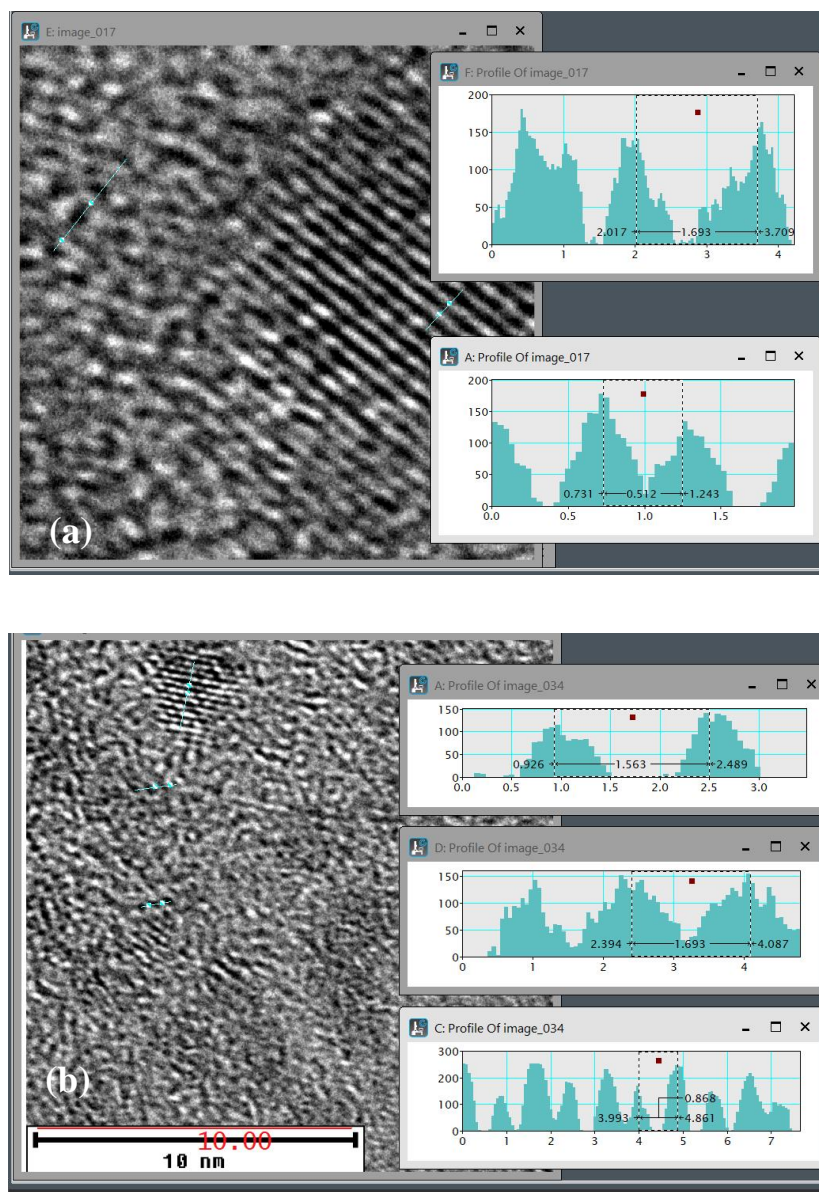


Figure 35. TEM images of the $\text{MnNi}(\text{CN})_4$ showing distinct regions with different d-spacing.

Figure 36 shows the electron diffraction of $\text{MnNi}(\text{CN})_4$ after treatment with DDP. The distinct and well-ordered diffraction patterns suggest the presence of more single standing sheets compared to before exfoliation.

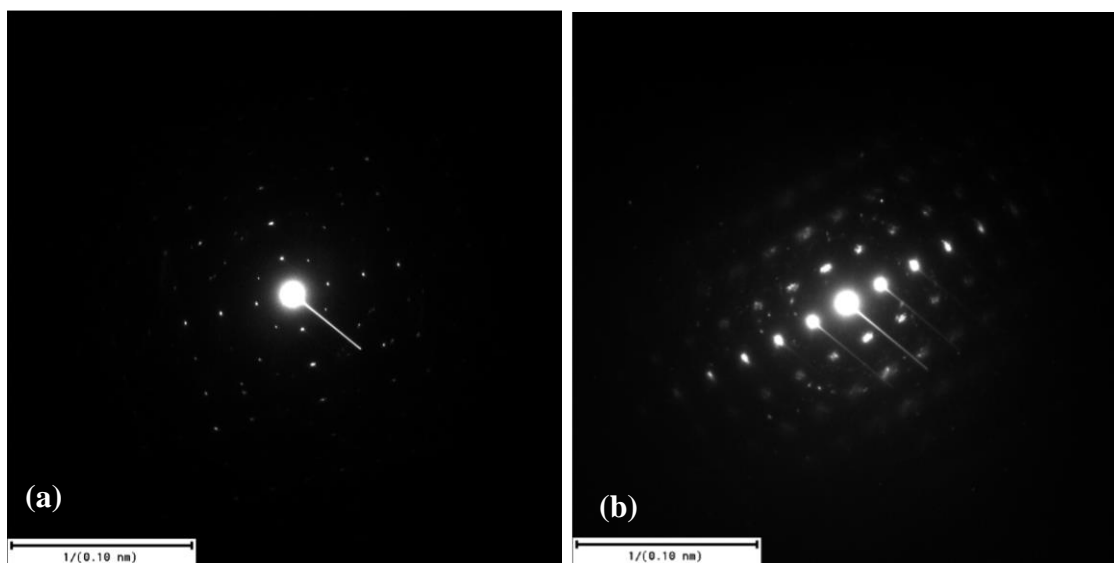


Figure 36 Electron diffraction pattern of $\text{MnNi}(\text{CN})_4$ after treatment with DDP (a and b). Distinct well-ordered pattern suggests singly standing sheets

3.2.4 Raman Scattering for Mn Transition Metal Complex

The Raman scattering for the $\text{MnNi}(\text{CN})_4$ powder before exfoliation in DDP is presented in Figures 37. The most prominent Raman peaks in the Mn occur at wavenumbers 2162 and 2178 cm^{-1} shown in the inset in Figure 37. As discussed in section 3.1.3, the peaks have been assigned ‘ B_{1g} ’ and ‘ A_{1g} ’ stretching vibrational modes of the $\text{C}\equiv\text{N}$ bonds respectively. Similarly, the bands at 316/480 cm^{-1} has been identified to corresponds to Mn-CN bond, thought to arise from the isotropic shift pattern in either linear or bent Mn-CN bond, suggesting that the Mn center may be flexible to allow re-orientation to accommodate external ligands and clathrate molecules. The sharp peak observed at 211 cm^{-1} corresponds to the ‘ A_{1g} ’ stretching of the octahedral site of the central Mn atom.

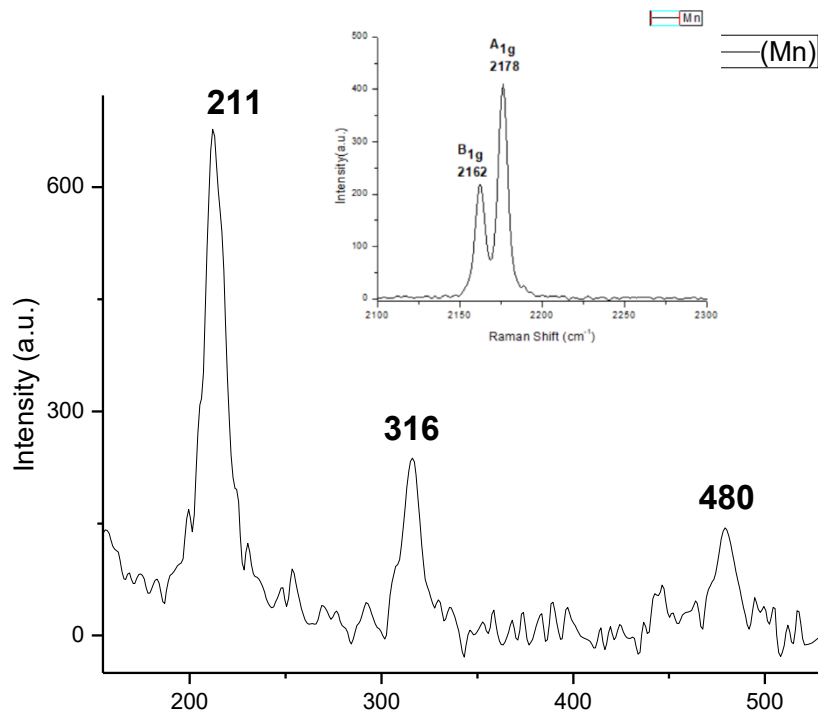


Figure 37. Raman spectra in the 150-600 cm^{-1} region, inset shows the prominent CN ‘B_{1g}’ and ‘A_{1g}’ spectra in the 2100-2300 cm^{-1} region.

3.2.5 TGA for Mn Transition Metal Complex

Figures 38a&b show the results for Mn samples before and after exfoliation with DDP. Before exfoliation, consider two onset temperatures at 92°C and 337°C. The first suggest a 11% wt loss. From calculations, 12.4% weight loss represents 2 molecules of non-coordinated water molecules. The next transition has onset at 337°C, result on 36% weight loss and resulting in 64% weight remaining from the initial mass. Figure 38b, reveals that after treatment with DDP, the onset temperature for first transition of the complex occur at 269°C, 29% weight loss occurred here, some of which is attributed to traces of DDP left in the sample. Decomposition of the sample occur from 389°C up to 418°C. The final amount of degraded sample after 470°C represents 41% of the total starting material.

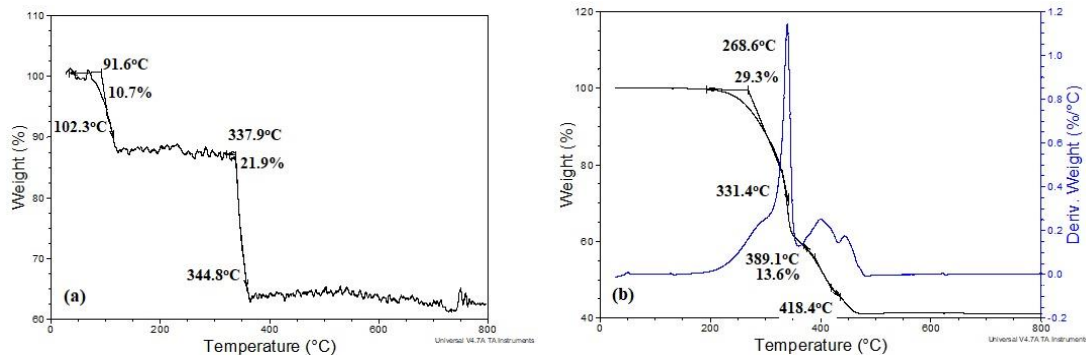


Figure 38. TGA. Analysis for Mn samples (a) before and (b) after exfoliation with DDP

3.2.6 VSM for Mn Transition Metal Complex

Figure 39 shows the hysteresis loop of the Mn samples obtained from VSM measurements at room temperature. The hysteresis indicates that the synthesized Mn has a saturation magnetization of 0.1450 emu/g, a coercive field (H_c) value of 271.143 Oe, remanent magnetization (M at $H=0$) of 0.0383 emu/g and squareness ($S = M_r/M_s$) is equal to 0.263. Similar values were obtained after exfoliation with DDP. The saturation magnetization is 0.1429 emu/g. The coercive field (H_c) is 271.834 Oe, the remanent magnetization (M at $H=0$) is 0.0383 emu/g and squareness ($S = M_r/M_s$) is equal to 0.267. The low magnetization saturation results for an odd-numbered d-electron species such as Mn complex suggest that the material is a diamagnetic or a weak ferromagnetic material as suggested by Nash et al. and observed by Goss et al.

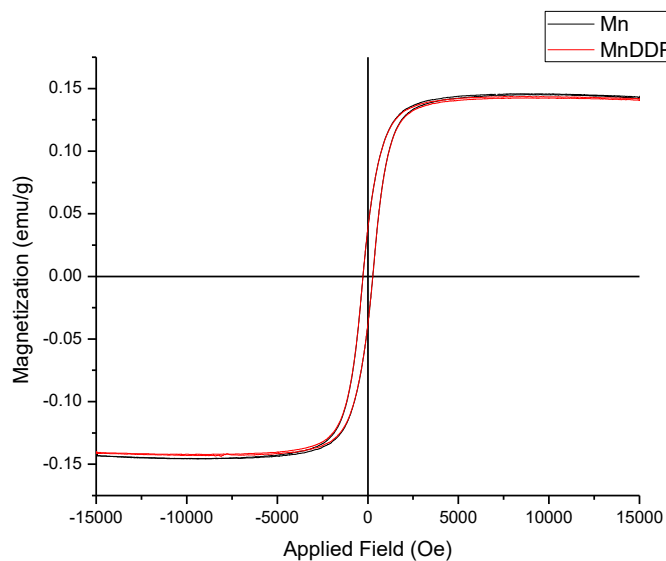


Figure 39. Magnetic hysteresis loop for Mn complexes

3.3 $\text{Ni}_2(\text{CN})_4$ and Derivative

This section discusses the results obtained from the analysis of $\text{Ni}_2(\text{CN})_4$ before and after exfoliation with DDP.

3.3.1 X-Ray Diffraction

The X-ray diffraction pattern for the $\text{Ni}_2(\text{CN})_4$ before and after exfoliation in DDP is presented in Figure 40.

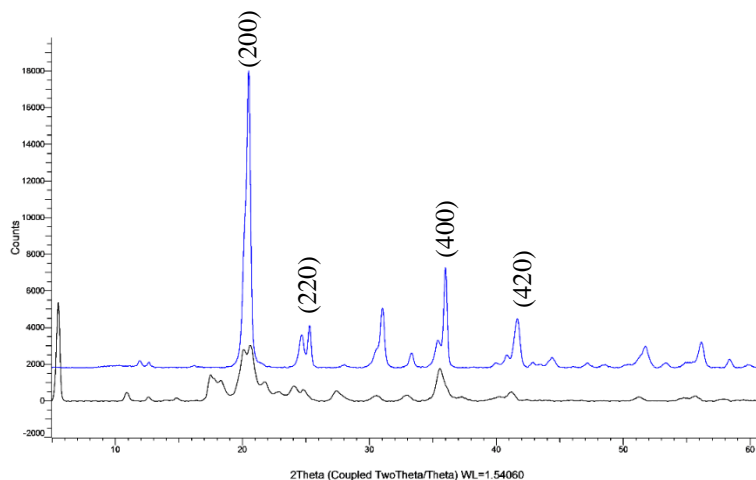


Figure 40. X-ray diffraction pattern for $\text{Ni}_2(\text{CN})_4$ before (blue line) and after exfoliation in DDP (black line)

It is observed that the major peak at 2-theta of 20.497° , with a d-spacing of 0.4330 nm. There is a shift of the peak to 5.514° after exfoliation with DDP. This correspond to a d-spacing of 1.6014 nm, hence we observe a significant increase in the d spacing judging from the XRD.

3.3.2 SEM and EDAX for Ni Transition Metal Complex

Figure 41a&b show the SEM image of the $\text{Ni}_2(\text{CN})_4$ before treatment with DDP and 42a&b show the SEM images after exfoliation in DDP, exfoliated sheet can be seen to separated out on the left hand side of the image in Figure 42a. The EDAX obtained from Figures 41b and 42b, depicted in Figures 43a&b, showing the respective energy dispersive x-ray spectroscopy before and after exfoliation.

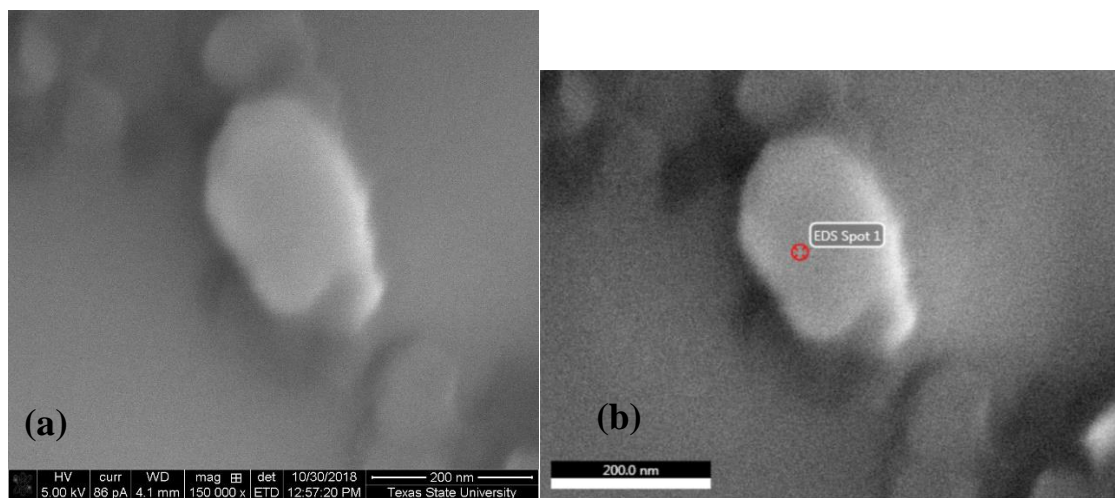


Figure 41. (a) SEM Images for $\text{Ni}_2(\text{CN})_4$ before exfoliation in DDP, (b) Spot mapped for EDAX

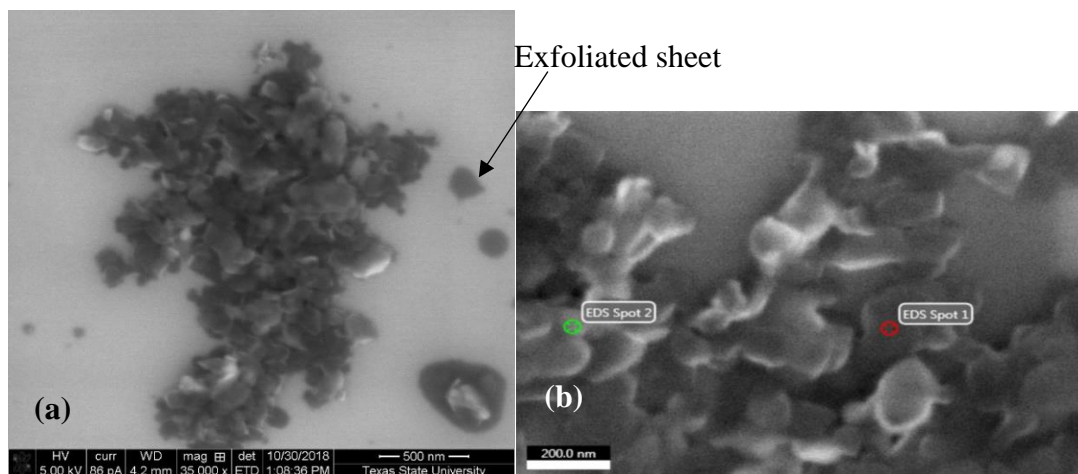


Figure 42. (a) SEM Images for the $\text{NiNi}(\text{CN})_4$ after exfoliation in DDP, (b) Spots mapped for EDAX

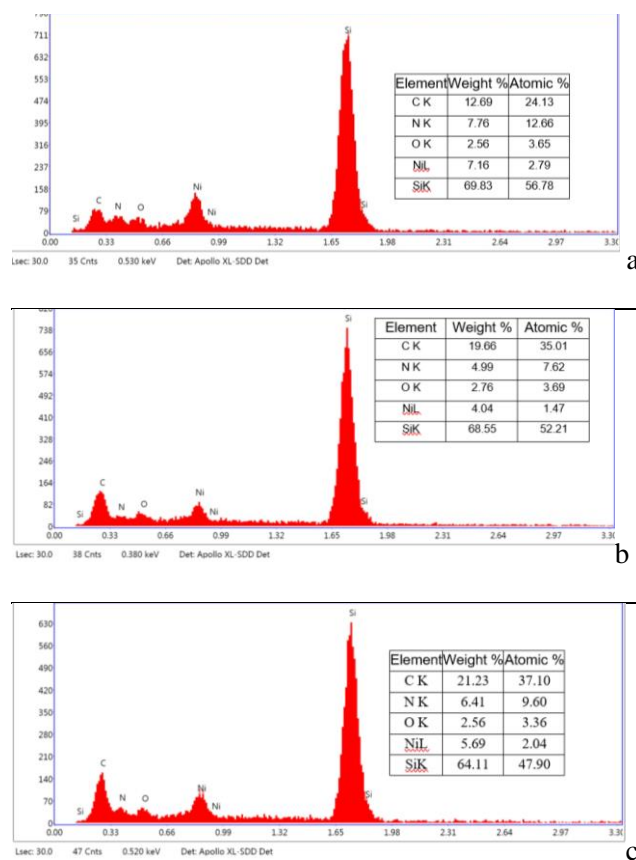


Figure 43. EDAX for Images of $\text{Ni}_2(\text{CN})_4$ (a) before exfoliation in DDP, (b&c) after exfoliation in DDP

3.3.3 TEM Imaging for Ni Transition Metal Complex

In a similar manner to previous sections, the TEM images of the Ni complex was obtained before and after exfoliation. Figure 44 reveals the TEM images of the Ni complexes before treatment with DPP. Multilayered structures can be observed from these images. These multiple layers can be seen stuck together and not separated into individual sheets before exfoliation.

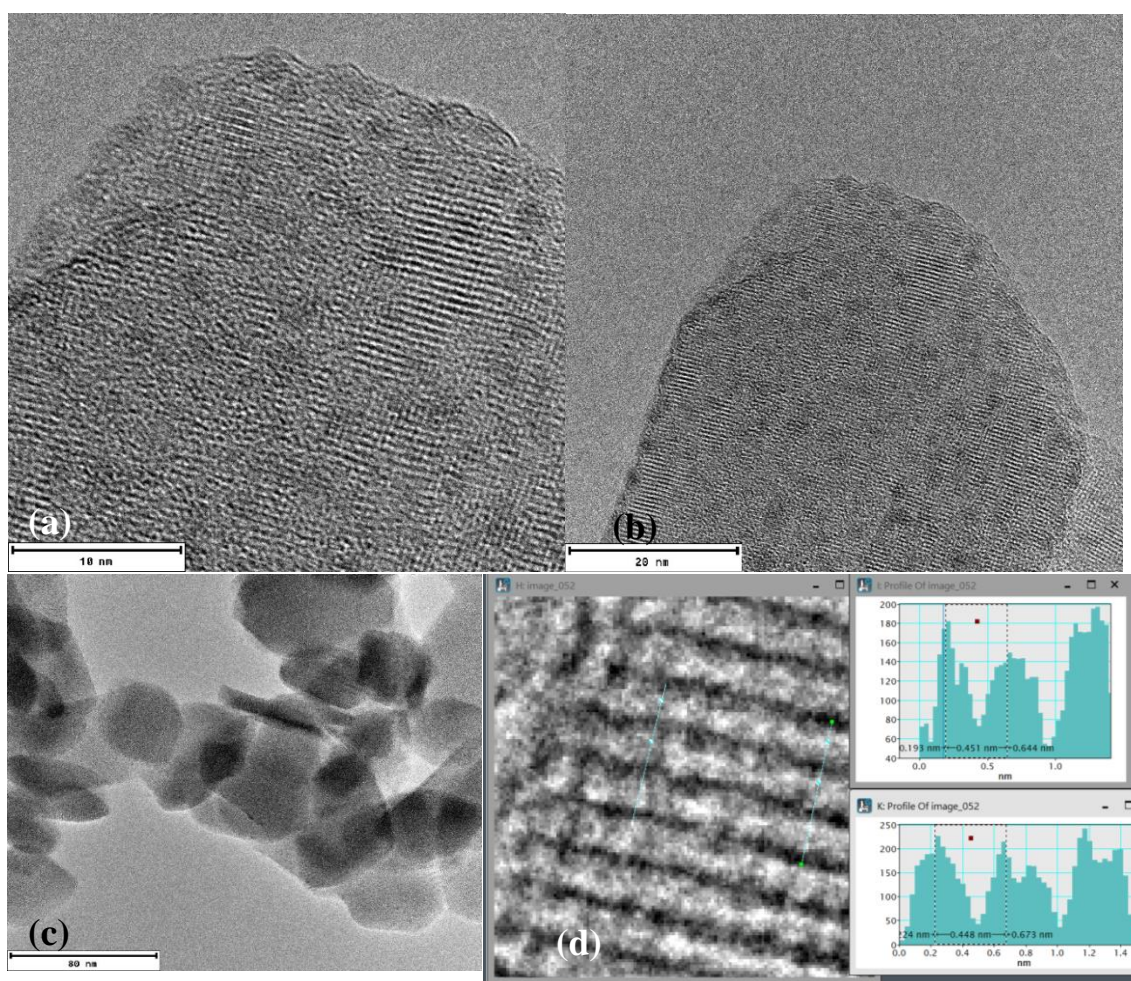


Figure 44. Transmission electron images at (a) 10 nm and (b) 20 nm (c) 80 nm of NiNi(CN)₄, revealing multilayer structure of the sample.

Analysis of the Figures reveal the d-spacing as 0.451 and 0.448 nm averaging 0.449 nm as shown in Figure 44d.

Figures 45a&b show the imperfect periodicity of Ni transition metal due to diffraction of electrons from the lower layers of the sample. These are seen as dim dots in the Figures

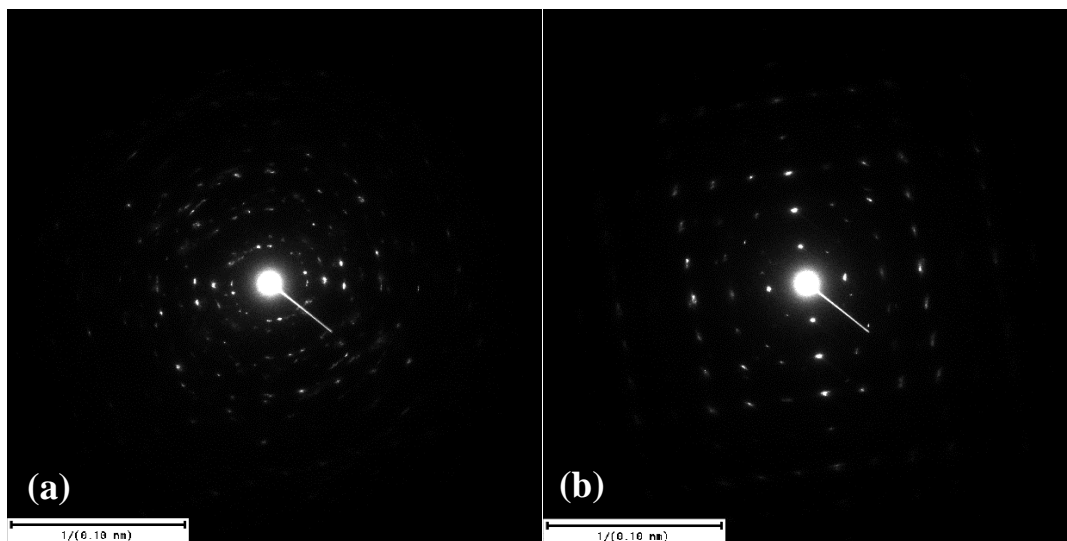


Figure 45. Electron diffraction pattern of NiNi(CN)₄ before exfoliation. The diffraction suggests the quality of the periodicity of the lattice is hampered by the diffraction from underlying layers of the sheet sample. Causing diffraction from more than one layer of the sample.

Results after exfoliation in DDP reveal separation of sheets. However, as can be seen in Figure 46a&b, unlike the distinct and clear separation observed in the case of Fe, there are still a substantial amount of multi-layers of stacked sheets mixed with the obtained single sheets of Ni complex after the DDP treatment. This observation may be due to preparatory method for sample analysis such as insufficient dilution of the prepared sample for TEM, or limited capacity to use sonication to exfoliate the DDP-

intercalated samples. Diffraction pattern shown in Figure 47 shows the well-ordered and crystalline nature of the exfoliated sample.

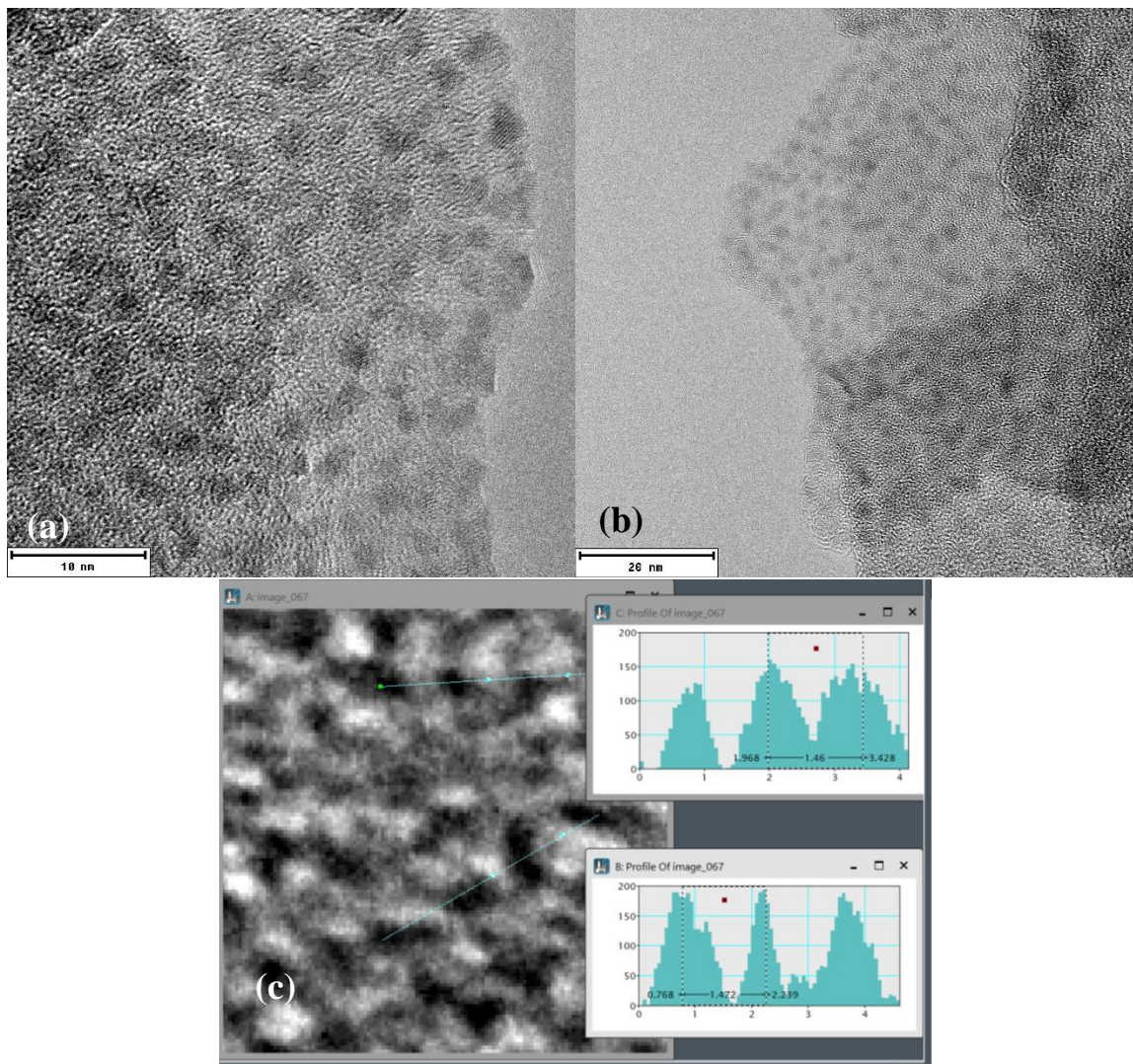


Figure 46. TEM images of NiNi(CN)₄ after treatment with DDP (a) 10 nm, (b) 20 nm, revealing single standing sheets as well as some multiple layers of sheet of sample. (c) profile d-spacing

The profile of image 46a reveal a d-spacing of 1.46 and 1,472 nm averaging 1.466 nm as shown in Figure 46c.

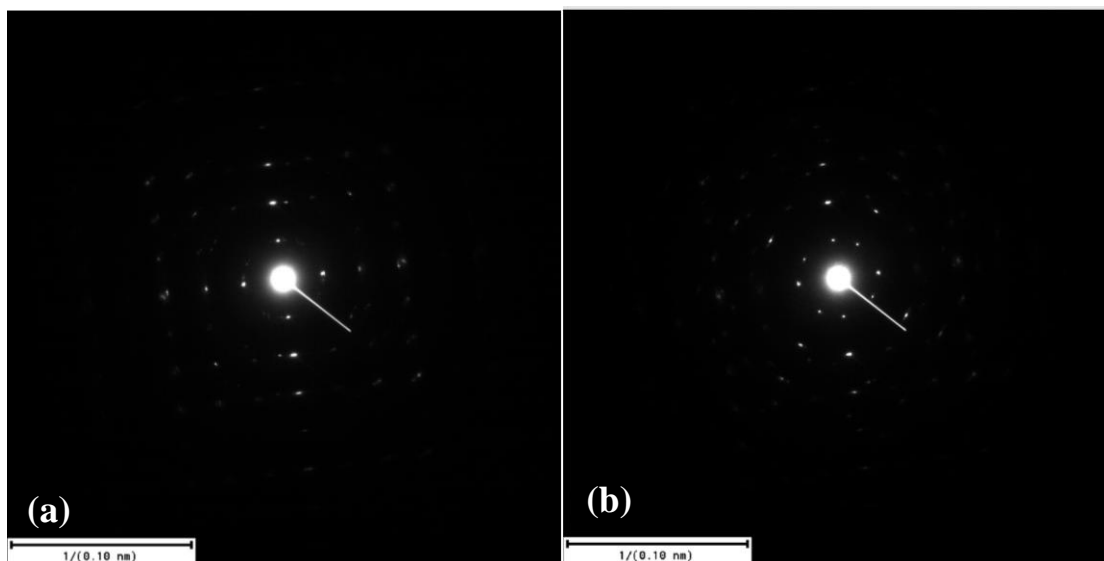


Figure 47. Electron diffraction patterns of the $\text{NiNi}(\text{CN})_4$ after treatment with DDP

3.3.4 Raman Scattering for Ni Transition Metal Complex

The insert in Figure 48, reveals the most prominent Raman peaks in Ni complex. This shift occurs at 2178 and 2190 cm^{-1} . This has been shown to correspond to and assigned to ‘ B_{1g} ’ and ‘ A_{1g} ’ of the $\text{C}\equiv\text{N}$ vibrational mode. The bands at $330/495\text{ cm}^{-1}$ has been identified to correspond to Ni-CN bond, which arises the isotropic shift of linear or bent Ni-CN bond. The bands suggest that the Ni center is flexible and capable of re-orientation to accommodate clathrate molecules. The sharp peak observed at 265 cm^{-1} is similar to the sharp peak of the Fe center at 230 cm^{-1} and in similar fashion corresponds to the ‘ A_{1g} ’ stretching of the octahedral site of the central Ni atom.

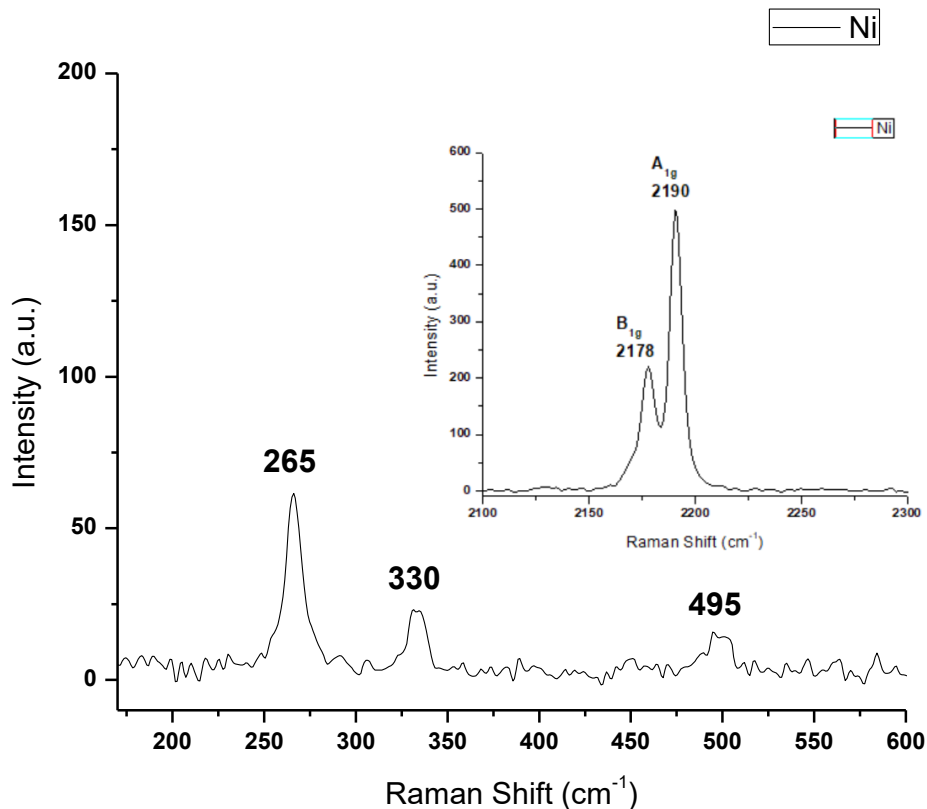


Figure 48. Raman scattering for Ni before exfoliation

3.3.5 TGA for Ni Transition Metal Complex

TGA for the nickel sample is shown in the Figures 49a&b below. The loss regions at onset temperatures of 98.43°C and 387.7°C. 18.1% weight loss occur after the first transition, this is close to a 19.6% theoretical loss of 3 molecules of water from trihydrate structure. The subsequent transition results in a 55% wt loss, this represent the decomposition of the complex which start just before 387°C and resulting in a leftover of 45% wt of the starting material. After exfoliation in DDP, the loss region onset at 194°C, resulting in 27.52% weight loss. This represents loss of any remaining DDP in the structure. The second transition occurs at 412°C resulting in a decomposition of the nanomaterial, about 40% wt of the starting material remained afterward.

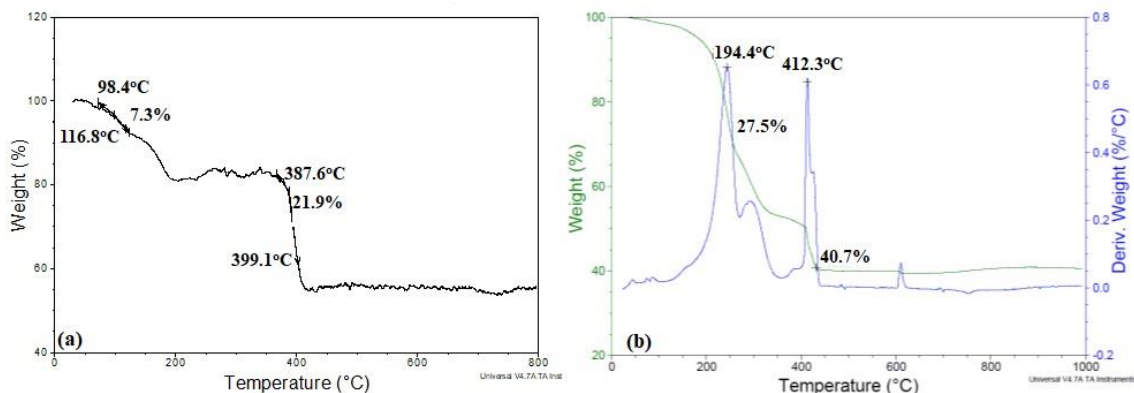


Figure 49. TGA analysis for the Ni samples (a) before and (b) after exfoliation with DDP

3.3.6 VSM for Ni Transition Metal Complex

Figure 50 shows the hysteresis loop of the Ni samples obtained from VSM measurements at room temperature. The hysteresis indicates that the synthesized Ni has a low saturation magnetization of 0.1430 emu/g, a coercive field (H_c) value of 270.418 Oe, a remanent magnetization (M at $H=0$) of 0.0383 emu/g and squareness ($S = M_r/M_s$) of 0.267. Similar value is obtained after exfoliation in DDP. The saturation magnetization after exfoliation is 0.1456 emu/g, the coercive field (H_c) is 264.217 Oe, the remanent magnetization (M at $H=0$) is 0.0386 emu/g and squareness ($S = M_r/M_s$) is equal to 0.262. The low saturation also indicates a diamagnetism in agreement with Nash et al. predictions.

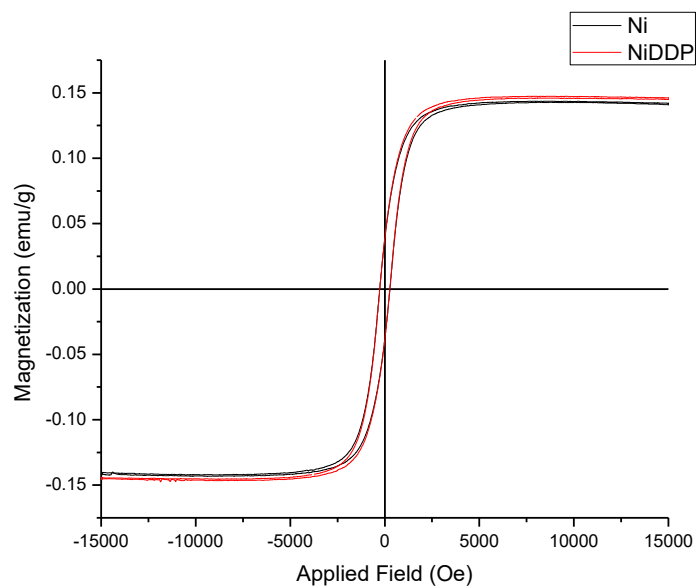


Figure 50. Magnetic hysteresis loop for Ni complexes

3.4 CoNi(CN)₄ and Derivative

This section discusses the results obtained from the analysis of CoNi(CN)₄ before and after exfoliation with DDP.

3.4.1 X-Ray Diffraction

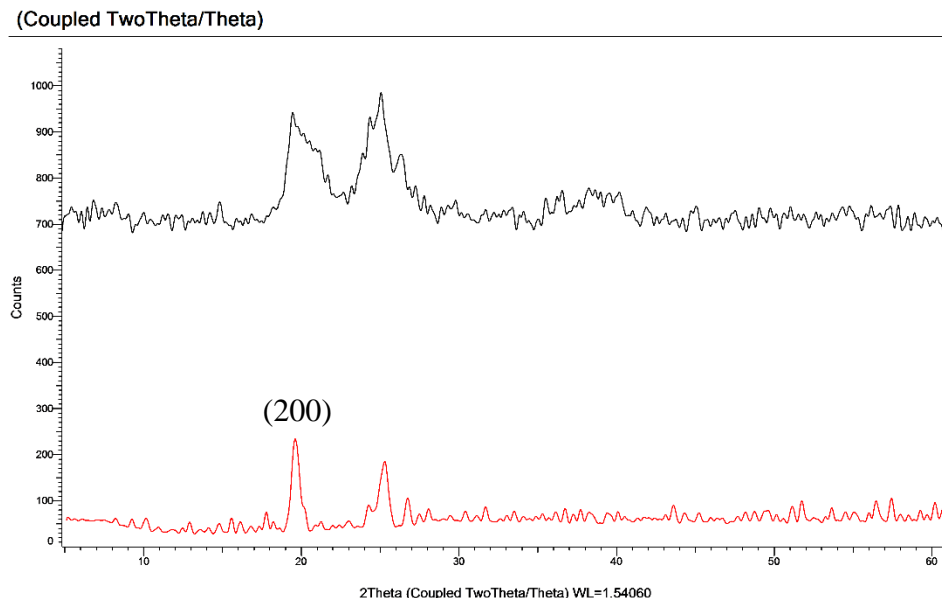


Figure 51. X-ray diffraction pattern for CoNi(CN)₄ before (red line) and after exfoliation in DDP (black line)

From the X-ray diffraction in Figure 51, the exfoliation process shows no significant changes in the d-spacing of the cobalt complex. The d-spacing of the two prominent peaks before exfoliation are at 2-theta of 19.806° (0.4479 nm) and 25.229° (0.3527 nm), while after exploitation in DDP are 19.479° (0.4553 nm) and 25.194° (0.3532 nm). It can be observed that the peaks obtained before exfoliation are sharp, but after treatment with DDP, the peaks are broadened with lower intensity. This might be due to lower crystalline size due to partial or no exfoliation with DDP. The lack of change in the position of the peak suggest that there is no intercalation with DDP. The previously investigated samples have higher d-spacing when compared to the data obtained here (0.3527 nm). It can be suggested that it is difficult to get water and DDP back into the structure once they have been removed, causing lack of intercalation and subsequently no exfoliation. The suggestion is consistent with other experimental observations with hydrated and unhydrated samples. The hydrated sample (pink color)

was dehydrated by heating and color changes to blue. Water was added to the dehydrated sample and left for 3 days at 75°C. The sample remained blue and never got reverted to the initial pink color, the reversion requires other chemical substitution which is beyond the scope of the present work. Figure 52 shows the different color regime of hydrated and dehydrated samples before and after exfoliation with DDP.

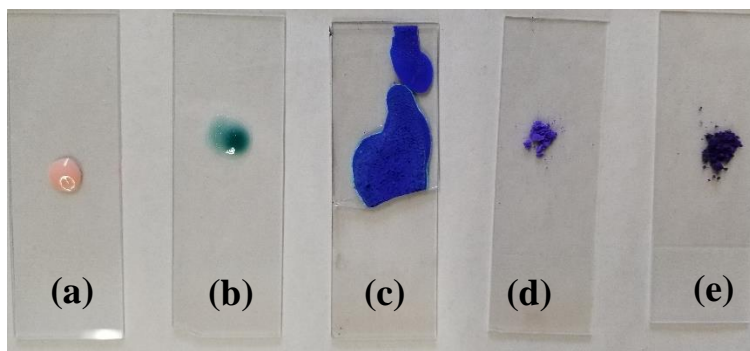


Figure 52. Different colors of cobalt cyanonickelate complex (a) Freshly prepared sample (b) fresh sample mixed with DDP (c) after heating to complete drying (d) aged dried sample (e) treated dried sample in DDP.

The freshly prepared sample of the Cobalt sample after removing excess salts give the pink color figure 52a, after completely drying the sample to become dehydrated, the sample becomes bluish purple figure 52d. The treatment of sample in figure 52a with DDP results in the light blue coloration observed in figure 52b and figure 52e upon complete drying at 185°C.

3.4.2 SEM and EDAX for Co Transition Metal Complex

The SEM images in Figures 53a-d for the $\text{CoNi}(\text{CN})_4$ before DDP treatment were taken with difficulties because of the magnetic charging in the sample. The Co complex are stacked together in a 3-D network of clusters. Figure 53 shows the EDAX with weight percent of Co (18.17%), the result was mapped from spot-1 in Figure 54d.

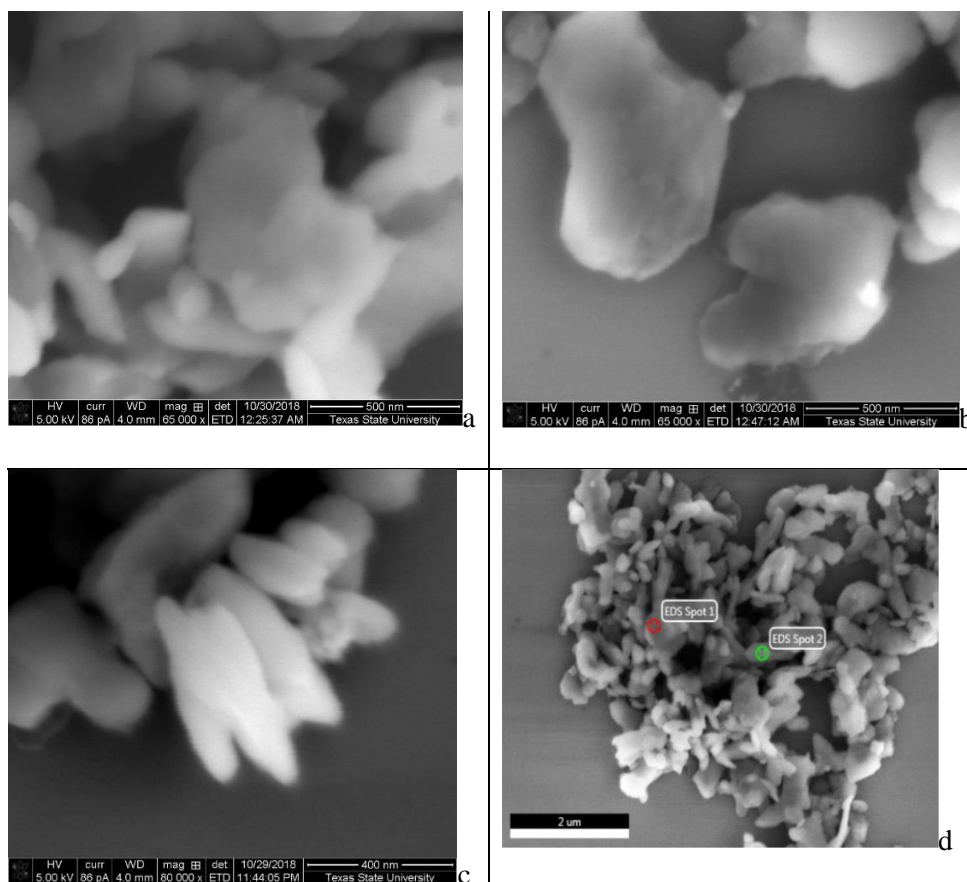


Figure 53. SEM Images of CoNi(CN)_4 at (a&b)65000x, (c)80000x, and (d) spots mapped for EDAX.

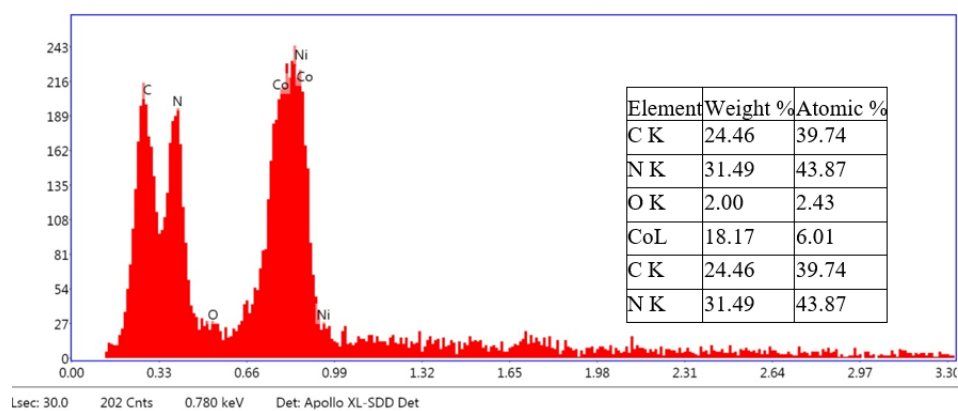


Figure 54. EDAX for Images of CoNi(CN)_4

3.4.3 TEM Imaging for Co Transition Metal Complex

Figures 55a&b shows the TEM images of Co powder complex before it was treated with DDP. Figure 55c shows the fringes with d-spacing of 0.427 and 0.361 nm

which supports the x-ray diffraction data in section 3.4.1. The diffraction pattern in Figures 56a&b suggests the quality of the periodicity of the lattice is hampered by the diffraction from underlying layers of the sheet sample, causing diffraction from more than one layer of the sample.

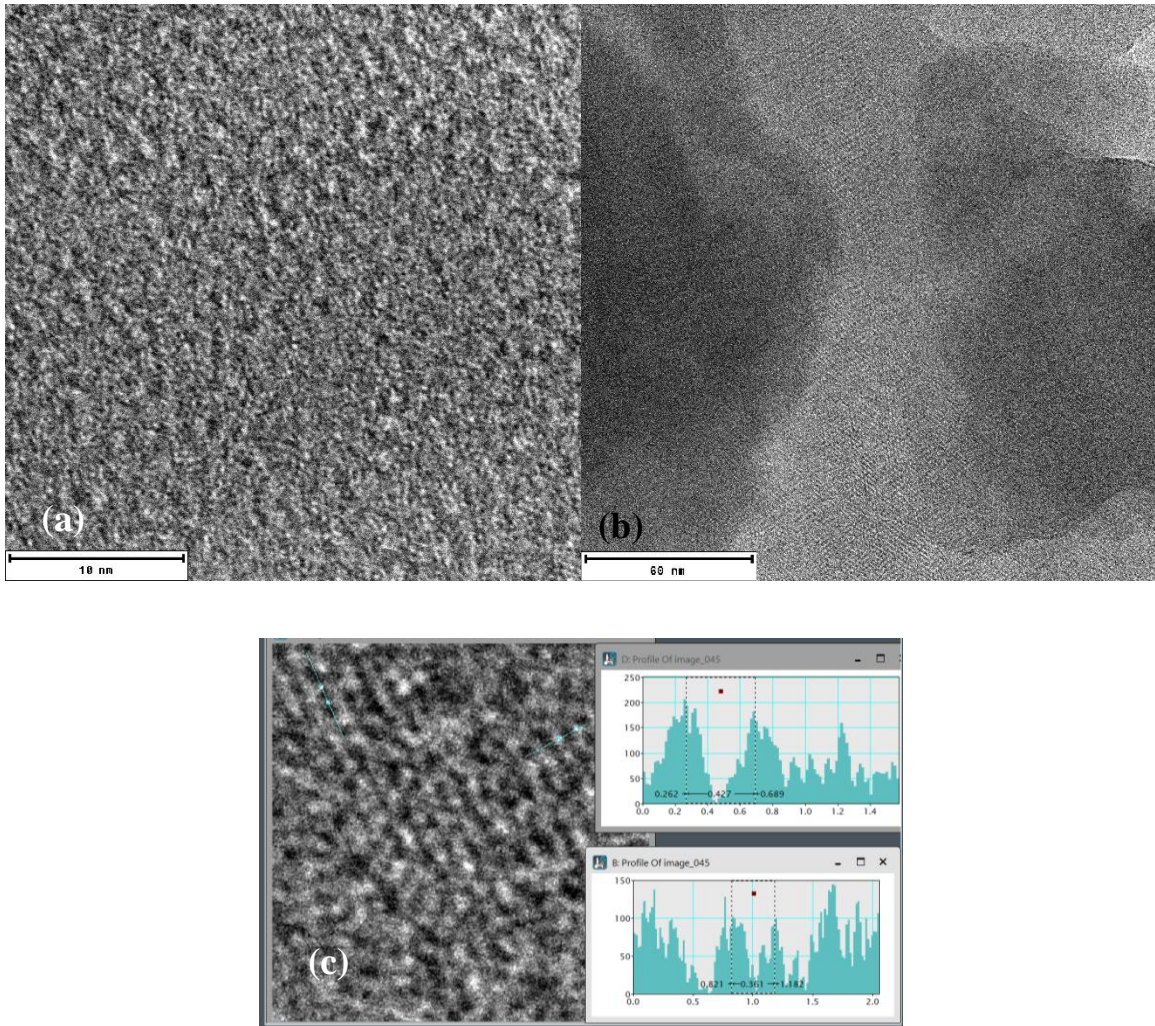


Figure 55. Transmission electron images at (a) 10 nm and (b) 60 nm of the $\text{CoNi}(\text{CN})_4$, revealing multilayer structure of the sample.

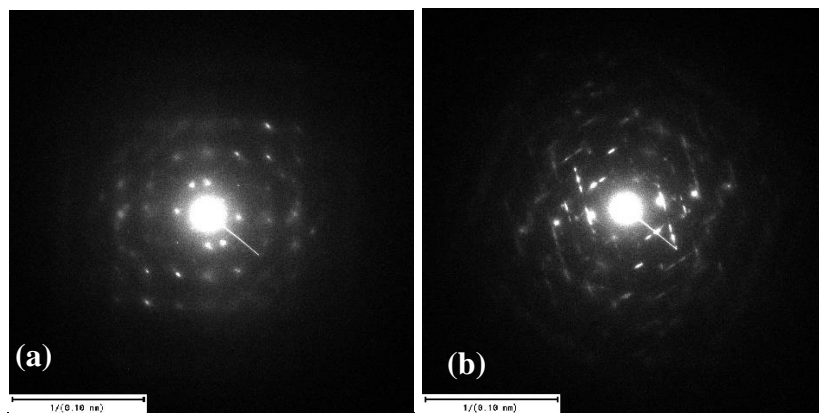
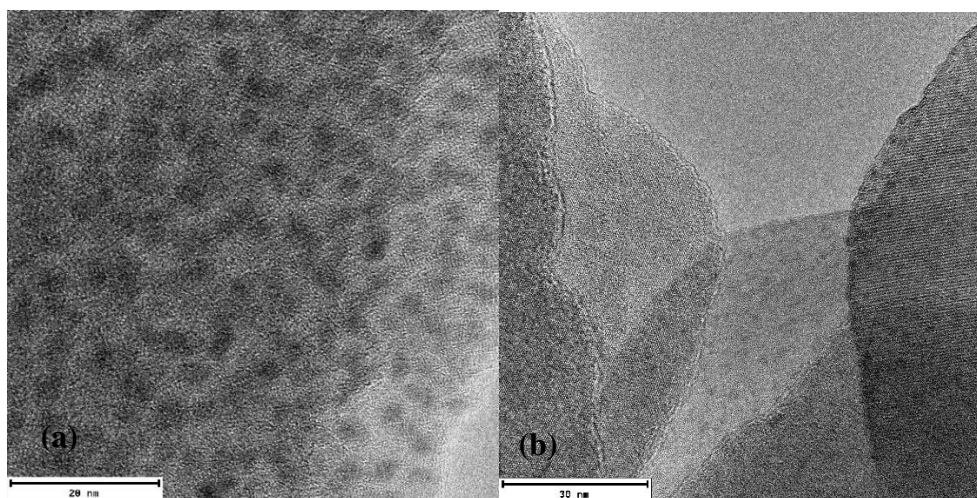


Figure 56. Electron diffraction pattern of CoNi(CN)₄.

TEM images and diffraction patterns obtained after exfoliation in DDP are shown Figures 57a&b and 58a&b. The Co sample after do not appear to be in separate single sheets after exfoliation in DDP, the TEM images suggest there exist in family of multi-layered sheets which are separate from each other rather than singly exiting sheets, resulting in short range ordered crystals. Figure 57c shows d-spacings of 0.377 and 0.473 which corresponds to the unexfoliated phase.



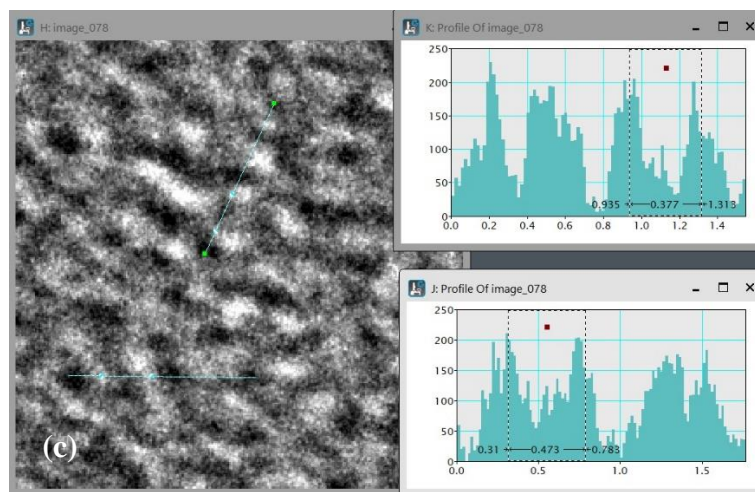


Figure 57. TEM images of $\text{CoNi}(\text{CN})_4$ after treatment with DDP (a) 20 nm, (b) 30 nm (c) profile

The electron diffraction also appears to be a little more distinct compared to the complex before exfoliation. However, the effect of lack of singly existing sheets can be seen from the pattern resulting in blurred patterns from originating underlying lower layers.

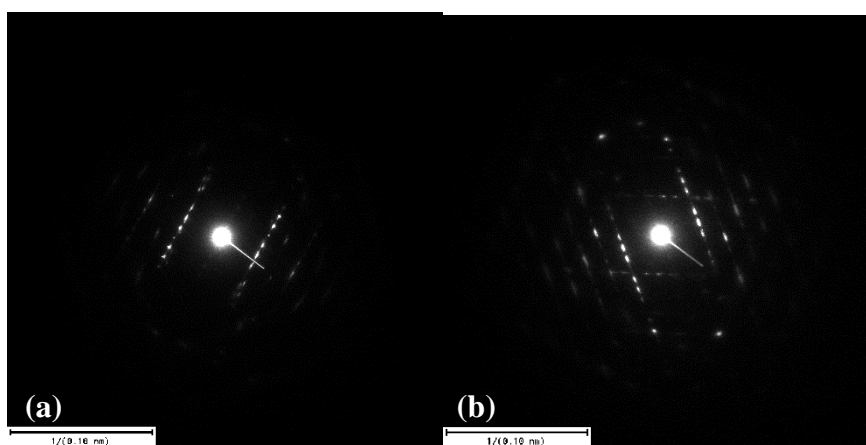


Figure 58. Electron diffraction pattern of $\text{CoNi}(\text{CN})_4$ after treatment with DDP (a and b).

3.4.4 Raman Scattering for Co Transition Metal complex

The Raman shift observed for the Co samples before exfoliation in DDP is shown in Figure 59. The prominent shift at a wavenumber of 2150-2200 cm^{-1} shown in Figure 59 insert represents the B_{1g} and A_{1g} of $C\equiv N$ vibrational mode.

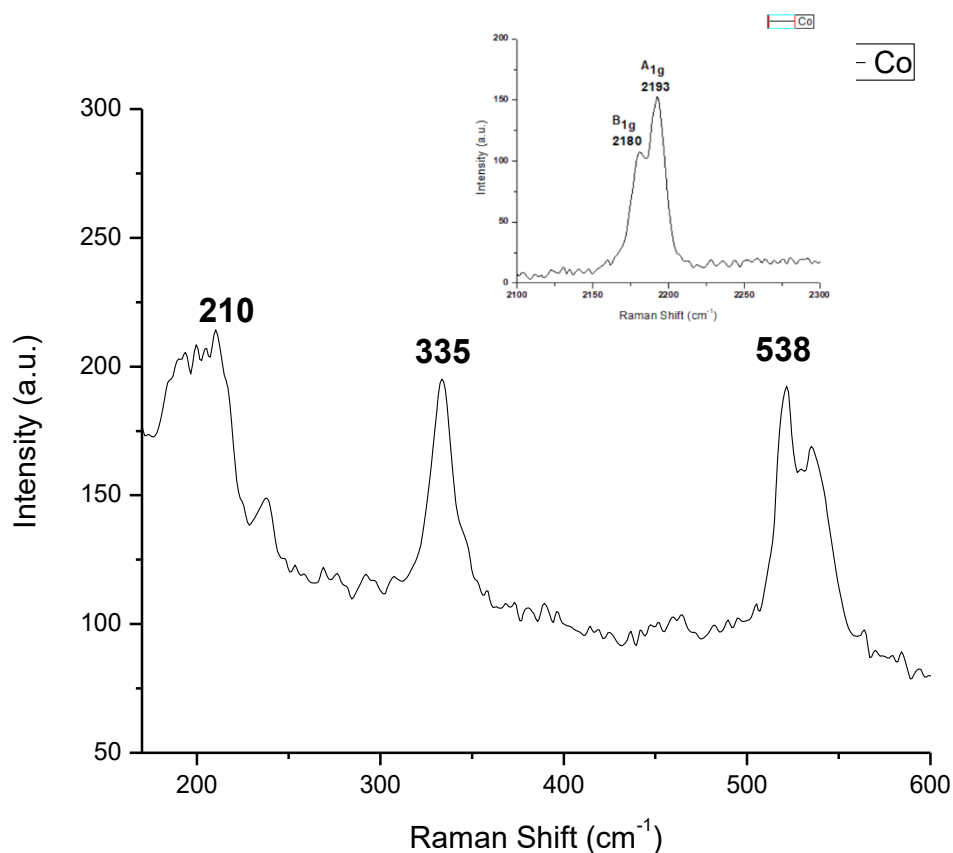


Figure 59. Raman shift for Co sample before exfoliation

The other peaks identified are similar to the previous peaks identified for Fe and other metals. However, there is a lot of peak broadening observed, especially at 210 cm^{-1} . The peak that corresponds to the ' A_{1g} ' stretching of the octahedral central Co atom. The bands at 335/538 cm^{-1} to correspond to Co-CN bond, which arises from the shift pattern of either linear or bent Co-CN bond. As discussed in the previous sections, the bands

suggest that the Co center may be flexible to re-orient itself to accommodate and trap molecules.

3.4.5 TGA for Co Transition Metal Complex

The TGA analysis of the Co complex before exfoliation reveals the onset temperatures for the Co sample is at 312°C. Decomposition follows until 25% of the weight sample is left at about 319°C. This shows that the Co sample is completely dehydrated, and the only transition that was observed is due to degradation of the material. On treatment with DDP, Onset temperature starts at to 245°C (Figure 60b). This transition may be due to loss of DDP traces. A little over 20% of sample weight was loss due to this phase. In the second region, thermal degradation initiates at 375°C and continues through 377°C until 460°C. The overall weight loss results in 43% of initial sample material remaining.

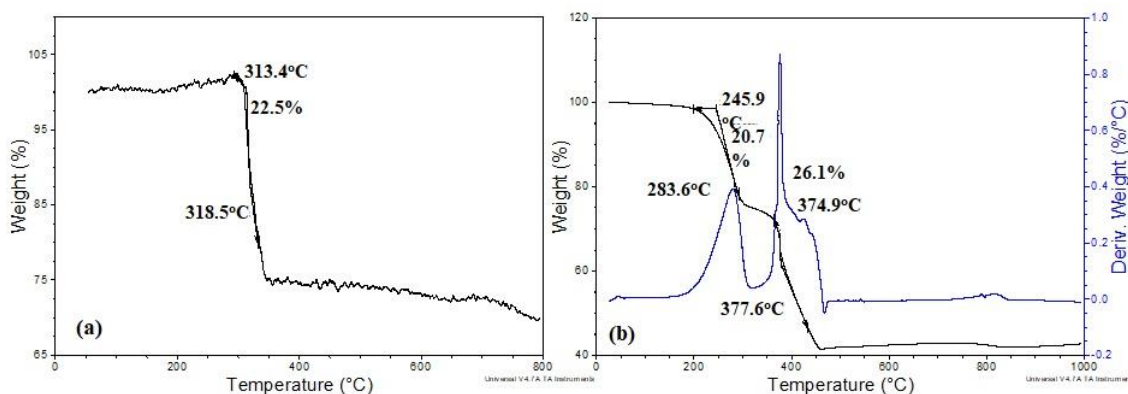


Figure 60. TGA. Analysis for Co samples (a) before and (b) after exfoliation with DDP

3.4.6 VSM for Co Transition Metal Complex

Figure 61 shows the hysteresis loop of the Co samples obtained from VSM measurements at room temperature. The hysteresis indicates that the synthesized Co has a

saturation magnetization of 0.1422 emu/g, a coercive field (H_c) value of 271.937 Oe, a remanent magnetization (M at $H=0$) of 0.0382 emu/g and squareness ($S = M_r/M_s$) value of 0.267. Similar results are obtained after it was exfoliated with DDP. As follows; the saturation magnetization is 0.1434 emu/g, the coercive field (H_c) is 271.498 Oe, the remanent magnetization (M at $H=0$) is 0.0383 emu/g while squareness ($S = M_r/M_s$) is 0.266.

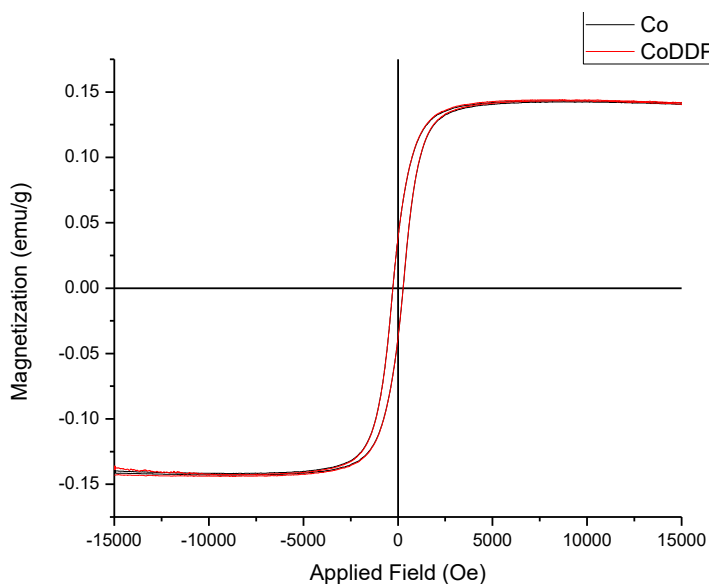


Figure 61. Magnetic hysteresis loop for Co complexes

3.5 Filtration Results of Transition Metal Complex on Microporous Fiber

Table 4 shows the calibration table for standard NaCl solutions. The linear fit of the averages of the five trials is obtained in Figure 62 and the equation of the line summarized in the table 5.

Table 4. Molarity Calibration

Standard Concentration (Mol/dm ³)	Hanna Edge Instrument Readings (% NaCl)					
	Trial 1	Trial 2	Trial 3	Trial 4	Trial 5	Average
0.001	0.2	0.2	0.2	0.2	0.2	0.2
0.002	0.4	0.4	0.4	0.4	0.4	0.4
0.005	0.8	0.8	0.8	0.8	0.8	0.8
0.010	1.5	1.5	1.5	1.5	1.4	1.5
0.020	3.1	3.1	3.1	3.1	3.0	3.1
0.050	7.1	6.9	6.8	6.6	6.0	6.7
0.100	12.7	12.2	12.0	11.5	11.3	11.9

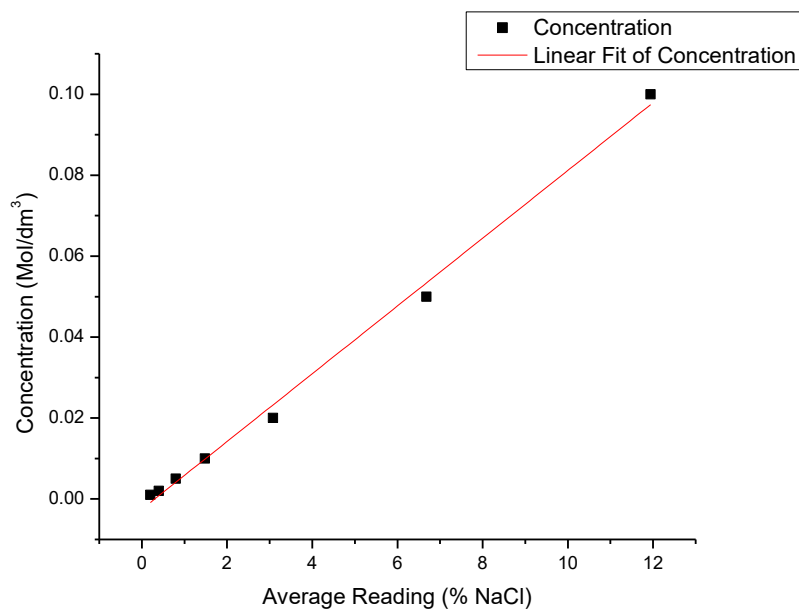


Figure 62. Linear fit for molarity calibration

Table 5. Linear Fit Summary for Na Ion Concentration

Summary	Intercept	Intercept	Slope	Slope	Statistics
	Value	Error	Value	Error	Adj. R-Square
Na+ Concentration	-0.003	0.001	0.008	2.46E-04	0.995

From table 5, the equation of line is obtained as;

$$\text{Concentration of NaCl} = 0.008x(\text{Average_}\% \text{NaCl}) - 0.003 \pm 0.001$$

In order to utilize the Hanna instrument within range above the filtered samples were diluted by a 10:1 dilution by mixing 1.0ml of sample with 9.0 ml of deionized water. The respective samples were tested for NaCl concentration, total dissolved solid and electrical conductivity. Table 6 shows the NaCl concentration correlated from the

Hanna instrument probe. Appendix A contains the total dissolved solid, and electrical conductivity data obtained from the samples.

Table 6. NaCl concentration in filtered water through respective membranes

Sample Name	Hanna Edge Instrument Readings (% NaCl)						Concentration for 10:1 dilution (Mol/dm ³)	Filtered Sample Concentration (Mol/dm ³)
	Trial 1	Trial 2	Trial 3	Trial 4	Trial 5	Average		
Fe	5.9	6.4	6.5	6.7	7.3	6.6	0.052	0.52
FeDDP	5.9	6.0	6.2	6.7	7.4	6.4	0.051	0.51
Mn	5.3	5.5	5.9	7.1	7.4	6.2	0.050	0.50
MnDDP	6.1	6.3	6.5	6.8	7.3	6.6	0.053	0.53
Ni	6.0	6.4	6.8	7.0	7.2	6.7	0.053	0.53
NiDDP	6.5	6.3	6.6	7.1	7.5	6.8	0.054	0.54
Co	6.3	5.3	6.0	6.7	7.0	6.3	0.050	0.50
CoDDP	7.1	7.7	8.4	8.9	9.8	8.4	0.068	0.68
Pristine	11.2	11.0	10.6	10.1	10.4	10.7	0.087	0.87

The filtered sample from the pristine 1.0-micron Sterlitech Teflon membrane shows a NaCl concentration of 0.87 M. Hence effect of the pristine PTFE is very minimal and have little or no significant filtration effect on the NaCl solution compared to the

membranes impregnated with metal tetra cyanonickelate complexes. The membrane samples impregnated with tetracyano-nickelate complexes grown on them filters between 32 to 50% wt. of NaCl from the concentrated NaCl solution. Exfoliated Cobalt with DDP filtered 32% wt of NaCl, which is the least amount filtered by the test samples. About about 50% wt of NaCl were rejected from the concentrated solution after filtering through the Mn and Co filter. 49% of the Na ion were rejected for Fe after DDP treatment and 48% rejection before it was exfoliated. All the other samples also show Na ion rejection before and after they had been exfoliated with DDP. The results show that except for Fe, all other samples after exfoliation in DDP give a slightly lower Na rejection. The difference is thought of as an artifact that is negligible. It could also be thought to arise from the possibility of Na^+ to escape from a possibly thinner layer upon saturated loading with NaCl. It can be imagined as a reduced tortuous path compared to unexfoliated counterparts. However, the difference is very minimal and negligible. The exfoliated version on the other hand may be economically preferred for commercial application because of energy savings that might result because they are atomistically thinner. The result is summarized in Figure 63.

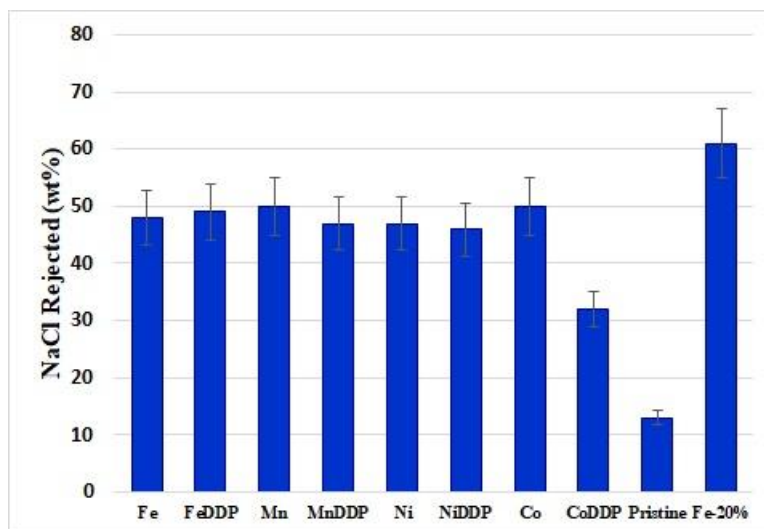


Figure 63. Comparison of the amount of NaCl rejected during filtration

In order to compare the filtration effect with reverse osmosis, 20% of the concentrated salt solution was allowed to pass through the membrane that has been impregnated with Fe complex. An average NaCl percentage of 5.2% was obtained from the Hanna instrument and this translates to 0.039 M for the 10:1 dilution of the filtered sample. Finally the resulting filtered sample contains 0.39 M NaCl. The result shows that 61% of the NaCl was removed by the process.

3.6 BET Surface Area Results and Analysis

The BET surface areas for all samples show no isotherm data. This suggests that the mechanism of filtration of the sample could not have happened by adsorption of the ions in the complex matrix, it is probably due to the selective permeation of ions based on size exclusion and the previously predicted ion charge repulsion.

4. RECOMMENDATION AND CONCLUSION

4.1 Recommendation for Future Work

Energy storage, magnetic and electronic application probing of the class of compound discussed need to be accessed to fully utilize the 2-dimensional nature of the formed structures. In addition, the prepared membranes in this research effort need to be further developed to be fully applicable for high through-put commercial applications beyond laboratory scale.

There are more to be understood in the behavior of the Co sample, the color transition effects and differences between hydrated and un-hydrated samples both before and after exfoliation in DDP. Also, the influence of monovalent, di-valent and trivalent cations on the hydrated cobalt complex should be investigated. New areas that also need to be studied include insight into the cobalt and the other metal cyanide complexes possible application as cathode material in sodium ion battery.

4.2 Conclusions

In this research, an innovative filter was designed based on Fe, Mn, Co and Ni transition metal cyanonickelate nanocrystals grown over polytetrafluoroethylene support. The developed membranes exhibited an efficient saline water filtration at extremely low energy expenses. The membranes in general removes over 50% of the Na^+ ion from a 1.0 M saline solution, when 10-15 ml of the solution was filtered. A even better performance of 61% was observed when 20% of the 15 ml volume was collected over the membrane instead of the total volume. The as prepared samples were confirmed by using standard

characterization techniques, such as x-ray diffraction, scanning electron microscopy, transmission electron microscopy, vibrating sample magnetometry and Raman scattering.

The structure of the nanomaterial was confirmed by Raman spectra and TEM. The TEM results clearly show the fringes of the crystals which allow the determination of the d-spacing of the species. The d-spacings results from TEM agrees with those from x-ray diffraction. The TEM results also confirms the exfoliation process, by revealing layers of overlap of sheets of the crystals, and short range ordered crystals existing in group of layered sheets for unexfoliated and exfoliated species respectively. Vibration magnetometry results reveal that the samples have low saturation magnetization ranging from 0.1422-0.1456 emu/g. The nanomaterials also show high coercive field within a vicinity of 270 Oe.

We suggest a growth mechanism that allows the metal complexes to be grown within the micropores of the Teflon membranes by producing a pseudo 2-D sheets within the pores. The opposing reactants serve as delimiters on both sides of the membrane thus preventing further growth of metal complexes. An illustration of the proposed growth mechanism is shown in the Figure 64.

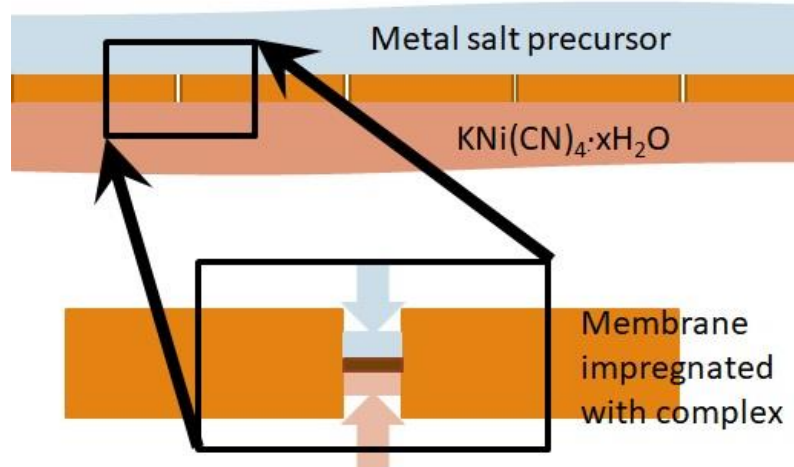


Figure 64. Limiting growth mechanism of complex within microporous membranes

The results gathered from mimicking a reverse osmosis produced a 61% removal of Na^+ ion, which is clearly better than the 50% removal that is obtained from the complete filtration. Filtering only 20% of the salt sample reveal that when the whole concentrated solution was allowed to pass through, there could be ion overload on the membrane which could cause seepage of the salt or set membrane failure into motion.

We expect the present fabricated filter to be very promising in applications such as commercial waste water remediation and saline water filtration. Finally, this research has successfully established earlier theoretical postulation by Goss et al. Hence our hypothesis that theoretical predictions using density function theory can create a pathway for investigating and understanding new knowledge area was established.

5. SYNTHESIS OF NICKEL FERRITE-GRAPHITIC LAYERS NANOCOMPOSITE WITH INVERTED MAGNETIC HYSTERESIS

5.1 Introduction

Magnetic materials have a fascinating and interesting magnetic and dielectric property especially when their size is reduced to the nanoscale. These properties attracted many researchers to study it. Ferrites are a group of magnetic material that consists of iron oxide mixed by one or more divalent metals such as Zn, Mn, Ni, Co etc. Unlike magnetic metals (Co, Ni, Fe etc.), ferrite have dielectric properties which means that when a ferrite material is subjected to electromagnetic wave it will not conduct electricity. These properties give privilege to ferrites over the other magnetic materials that conduct electricity. This is one the reason for the wide range applications of ferrites [54, 55]. In the recent years, a great attention has been focused on nickel ferrites due to the promising applications in multilayer chip inductor. Ni-ferrite can be prepared by many ways including ball milling, sol-gel, hydrothermal [56], microwave [57], co-precipitation [58], reverse micelle [59], combustion [60], solvothermal [61] etc.

In the present contribution, a new way to prepare nickel ferrite using iron tetracyanonickelate (II) ($\text{Fe}[\text{Ni}(\text{CN})_4] \cdot 3\text{H}_2\text{O}$) is presented. We found that this material can be converted into nickel ferrite by heating it in air. In-fact it has been observed that as the temperature reaches 400°C the iron tetracyanonickelate (II) powder starts to ignite. Surprisingly, the ignition does not take place uniformly, but it starts at certain point and then steadily propagates in a wave-like fashion through the entire material. As result the materials was found to expand to form C/NiFe₂O₄. The as-prepared samples were characterized by standard techniques to confirm the formation of nickel ferrite. The

present finding is novel and important for both scientific prospective and industrial applications.

5.2 Experimental work

Iron tetracyanonickelate (II) powder ($\text{Fe}[\text{Ni}(\text{CN})_4] \cdot 3\text{H}_2\text{O}$) has been prepared according to the previous method described earlier in chapter 2. Nickel ferrite of the form $\text{C}/\text{NiFe}_2\text{O}_4$ was prepared as follow; 0.3 g of the dry prepared iron tetracyanonickelate (II) powder was placed in quartz boat and place in an open-ended glass tube which was then place in a furnace at 400°C for 1 hour. Air was allowed to freely pass through one open end while the second is connected to exhaust system. In order to visualize the reaction a separate experiment was performed using hotplate inside the fume hood and the ignition propagation was observed.

5.3 Characterizations

The as-synthesized samples, without any further washing or any treatments, were analyzed by different characterization techniques to explore their morphological, structural and magnetic properties. The morphological features were investigated using field emission scanning electron microscope (FE-SEM), FEI Helios Nanolab 400, samples were imaged using 5-10 kV accelerating voltage, working distance 4 mm and beam current 86 mA. The elemental composition was analyzed using energy dispersive analysis X-ray (EDAX) attached to SEM. Structural properties were studied by the field emission high-resolution transmission electron microscope (HRTEM), JEOL 2010F at accelerating voltage 200 kV. Raman spectroscopy Thermoscientific DXR with excitation wavelength 532 nm was used to probe the room temperature vibrational modes. X-ray diffraction (XRD) was done with Bruker D8 Advance ECO, thermogravimetric analysis

(TGA) was done using TA instruments Q50. MicroSense EZ9 vibrating sample magnetometer (VSM) was applied to probe the magnetic properties at room temperature.

5.4 Results and Discussions

5.4.1 X-ray Diffraction

The X-ray diffraction from Figure 65 reveals that the synthesized powder has an inverse spinel structure. As it can be seen from the Figure. The observed peaks can be ascribed to the following planes, (220), (311), (222), (400), (422), (511) and (440); which are in a good matching with JCPDS No. 10-325 [62]. The calculated lattice constant was 8.624 Å. The estimated crystallite size calculated using the Scherrer equation was 23.92 nm. By considering the stoichiometry of the reaction in going from Fe[Ni(CN)₄] to NiFe₂O₄, we observe that the mole ratio of Ni:Fe has changed. This would indicate that the excess Ni could be dispersed as NiO or there could be partial substitution of Ni for one quarter of the Fe in the ferrite structure. Unfortunately, the x-ray pattern for NiO is a

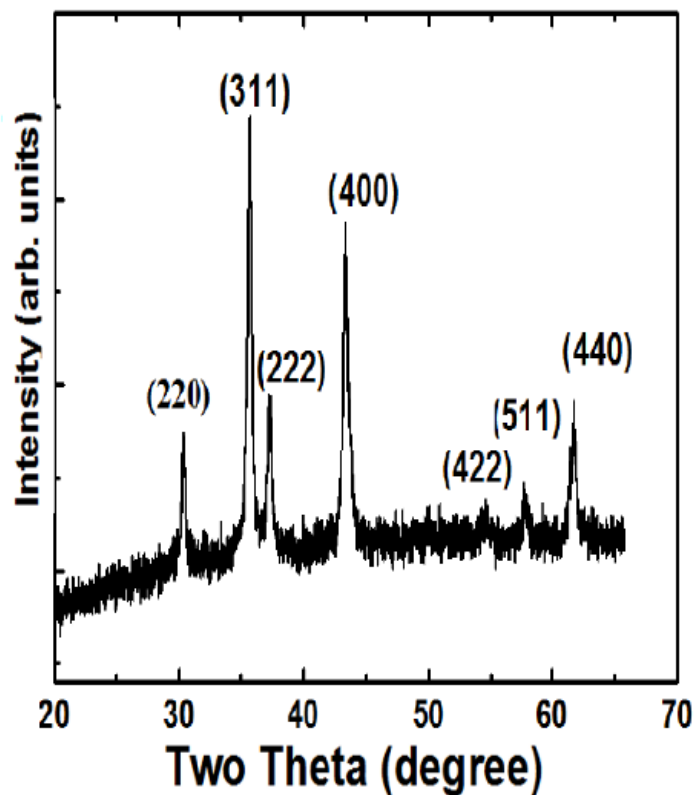


Figure 65. X-ray Diffraction of Synthesized Nickel Ferrite

cubic phase with few lines and they all fall under the lines of the ferrite phase hence no different or unique peaks will be observed for NiO.

5.4.2 Scanning Electron Microscopy

The detailed surface morphology of the obtained nickel ferrite sample has been studied using SEM. Figure 66 shows the SEM micrographs for the nickel ferrite powder at two different magnifications. SEM morphological investigation reveals that nickel ferrite nanoparticles have nonuniform morphology with large amounts of agglomeration.

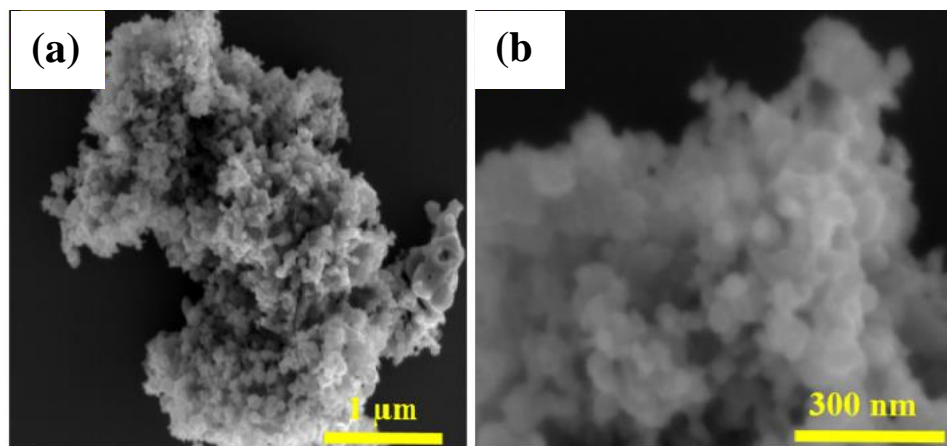


Figure 66. SEM Images of Nickel Ferrite (a) $1\mu\text{m}$ (b) 300 nm

5.4.3 Transmission Electron Microscopy

HRTEM was employed to study the structure and morphology of the as-prepared sample. Figure 67a&b shows the obtained HRTEM images of the as-prepared nickel ferrite. It is clear from the images that the arranged fringes suggest that the obtained nickel ferrite has good crystallinity with the fringe spacing of 0.26 nm which is attributed to the (311) lattice plane orientation. HRTEM investigations confirm the results obtained by SEM and XRD. Cubic lattice is clearly seen with the interlayer distance equal to 0.26 nm which confirm the formation of nickel ferrite.

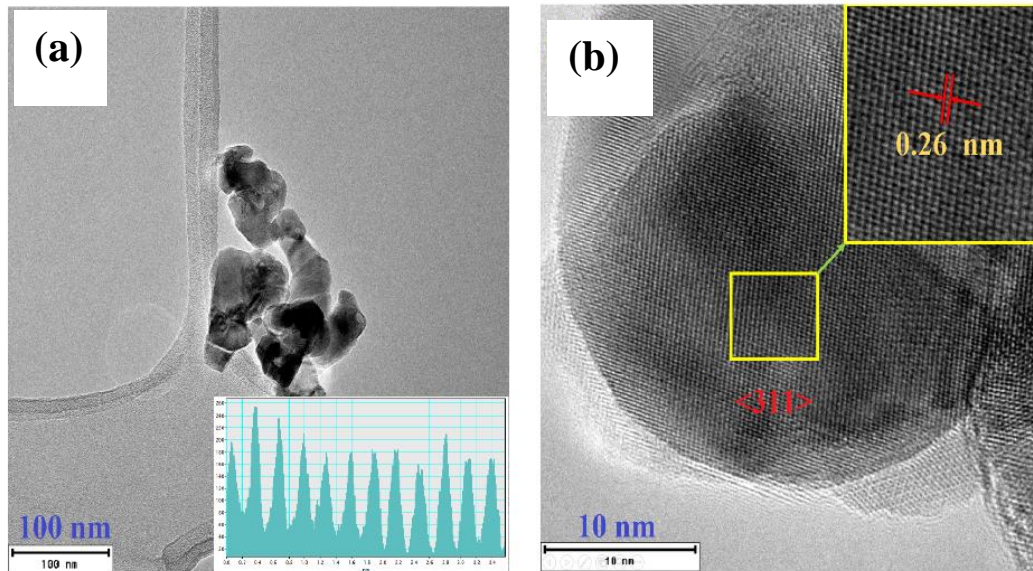


Figure 67. TEM Images of Nickel Ferrite (a) 100 nm (b) 10 nm

5.4.4 Raman Spectroscopy

The lattice vibrations have been investigated using Raman spectroscopy at room temperature. Figure 68 shows the obtained Raman spectra of the as-prepared nickel ferrite powder. Several vibrational bands have been observed for the iron nickel cyanide. According to group theory, it has been predicted that spinel structure has 42 vibrational modes. Among these modes only A_{1g} , E_g and T_{2g} are Raman active [63]. These characteristic vibrational modes - A_{1g} , F_{2g} and E_g for nickel ferrite were observed at 685, 481 and 324 cm^{-1} respectively. These are due to the stretching and bending vibrational modes for metal-C/metal-N and metal-CN/metal-NC [64-66]. The most intensive peaks at the range $2000\text{-}2200\text{ cm}^{-1}$ has been identified in section 3.1.4 to be attributed to ν ($\text{C}\equiv\text{N}$) stretching modes. Interestingly, in Figure 68c, a zoom in to this mode reveals that it consists of three peaks separated by 20 cm^{-1} intervals with gradual increase in intensity as the wave number increases.

Additionally, two vibrational bands were observed at 1363 and 1576 cm^{-1} which can be ascribed to D-band and G-band of carbon materials. It is well known that D-band arises from the defects and imperfection in graphite structure, which generally comes from the edges. While G-band arises from the hexagonal graphite with perfect structure. Moreover, the ratio between the intensities of these two bands can give information about the crystal quality of the carbon material [67-69].

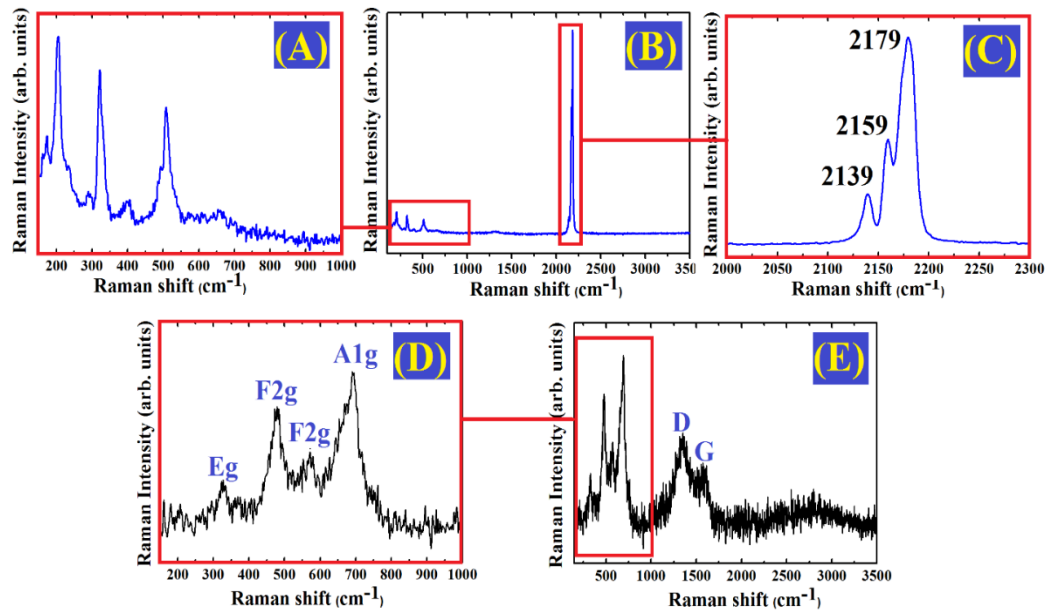


Figure 68. Raman Spectra of Nickel Ferrite

5.4.5 Magnetic Properties

The magnetic property of the C/NiFe₂O₄ nanoparticles before and after heating in air were studied using VSM. Figure 69 show the magnetic hysteresis loop obtained at room temperature. Before heating, a traditional magnetic hysteresis with specific magnetization of 0.142 emu/g was obtained as discussed earlier in chapter 3. However, the hysteresis loop for the C/NiFe₂O₄ nanoparticles, is inverted in which the specific magnetization is positive when the applied magnetic field is negative and negative as the

applied magnetic field becomes positive. The saturated specific magnetization is 28.668 emu/g which is much lower than the saturation value for bulk material. In order to make sure there is no mismeasurements, the sample was checked to be correctly positioned and the measurements were repeated several times. This unusual behavior is known as prosteresis and was observed for core-shell structure when the outer shell is diamagnetic and the inner core is ferromagnetic [70-73]. Hysteresis characteristics can provide important information about the magnetic system. For example, the shape of the magnetic hysteresis is an important parameter that determines the magnetic response to the external magnetic field. Recently Ma et al. [74] reported the self-reversed magnetic hysteresis in the case iron oxide and Fe^{3+} core shell structure in which it possesses both the diamagnetic and ferromagnetic characteristics at the same time. The authors explained the occurrence of the self-reversed magnetic hysteresis by the magnetic exchange coupling between the Fe^{3+} and iron oxide core. In the present case, the outer shell is the graphitic layer while the inner core is the nickel ferrite nanoparticles. Although understanding the magnetic behavior of the present case needs more investigations, we believe that there are some surface interactions that takes place at the nickel ferrite-graphitic layer interface which in turn could cause this anomalous magnetic behavior.

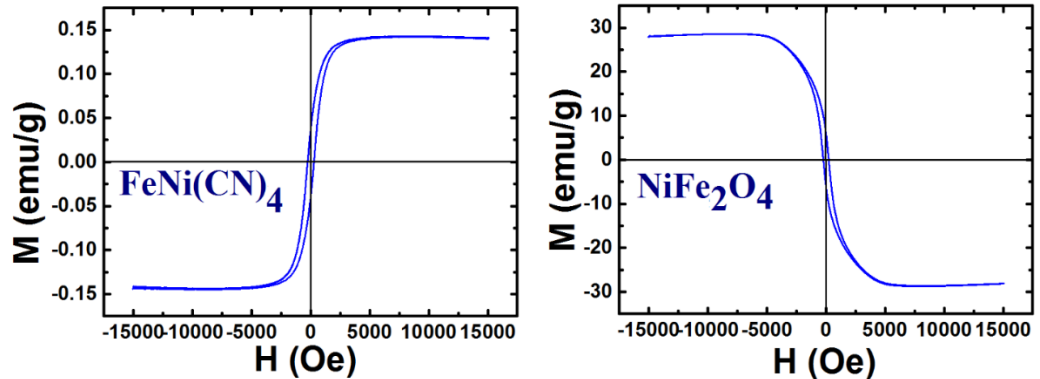


Figure 69. Magnetic hysteresis loop of the nickel ferrite

5.5 Proposed Mechanism of Nickel Ferrite Formation

It has been demonstrated that nickel ferrite nanoparticle can be synthesized using iron tertcyanonickelate (II) powder by simply heating it at 400°C in air. There are several similar methods for the synthesis of nickel ferrite such as solution combustion or citrate gel auto-combustion method. The current method involves the exothermic reaction that takes place in the gel or solution media. In fact, a lot of new materials with unusual properties have been successfully synthesized via this method [75]. The chemical mechanism, thermodynamic and kinetics of this method have been intensively studied and discussed. Although our synthesis approach does not involve citric acid and the experimental procedure is completely different, we still believe that the chemical mechanism can be explained in a very similar way. In principle, the way that ignition process happens, as depicted in the frames in Figure 70, suggests that the starting point local the temperature suddenly increases to very high degree (~ 1000°C). It is a reasonable assumption that, the key point lies on the presence of element such as

hydrogen and carbon which are highly flammable especially when this reaction happens in open air and there is enough oxygen that can oxidize these atoms and start the fire. Based on our TGA results in section in section 3.1.5, there two decompositions which took place within the temperature range 100-800°C. The first was attributed to loss of water. The second which happened around 400°C resulted in the decomposition of the metal complex.

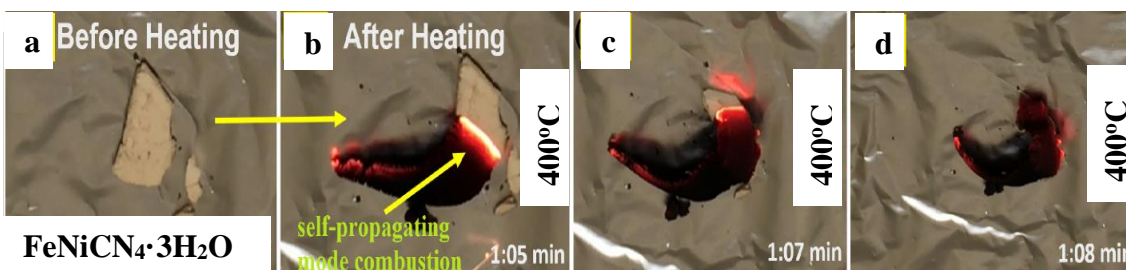


Figure 70. Self-propagating ignition of nickel ferrite formation

The kinetics of the current approach can be summarized in two steps. In the first step all water molecules are removed, i.e. dehydration process. In the second step decomposition of cyanide takes place which is accompanied by an exothermic reaction in which a lot heat is generated in the system in addition to a large quantity of gas. We believe that hydrogen cyanide will be formed during this decomposition which is highly flammable. It has been reported that only nickel oxide, not metallic nickel, can facilitate the decomposition of HCN (< 99 %) at 400°C in which the nickel oxide has exceptional catalytic activity at this temperature [76]. Since our sample contains nickel which can be oxidized at the reaction temperature in the presence of atmospheric oxygen, it could have some impact in the decomposition of the HCN. The decomposition of HCN may be the reason behind the ignition and the observed ignition propagation front that takes place in

the sample. The rapid expansion of the sample (Figure 71) could also be explained by this mechanism.

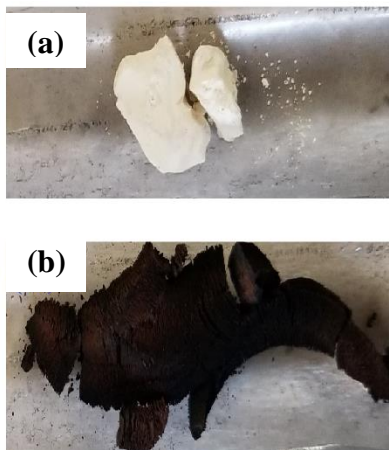


Figure 71. Rapid expansion of iron tetracyanonickelate (II) to form nickel ferrite

5.5.1 Conclusions

In summary, nickel ferrite nanoparticle has been successfully synthesized via a novel approach. This approach is straightforward, simple and can be scaled up for industrial applications. The approach does not involve the use of any surfactant or applying high temperature. Simply by heating $\text{FeNi}(\text{CN})_4 \cdot 3\text{H}_2\text{O}$ in the air at 400°C , it is observed that the $\text{FeNi}(\text{CN})_4 \cdot 3\text{H}_2\text{O}$ starts to ignite and burn to form nickel ferrite. The formation of nickel ferrite was confirmed by XRD, HRTEM, Raman, and SEM. The formation mechanism of nickel ferrite could be explained by the thermal decomposition of cyanide and possible formation of HCN which is responsible for ignition. A reverse hysteresis or magnetic prosteresis was observed for the graphitic-Nickel ferrite nanomaterial. This suggest that there are some surface interactions that takes place at the nickel ferrite-graphitic layer interface which in turn could cause this anomalous magnetic behavior.

In summary, the highlights of the second part of this research is presented as follows:

- 1 A new approach to the synthesis of nickel ferrites has been presented
- 2 Nickel ferrite nanoparticles were prepared via heating iron-nickel cyanide in the air.
- 3 Mechanism of nickel ferrite was proposed
- 4 The present method can be applied to different ferrites types.

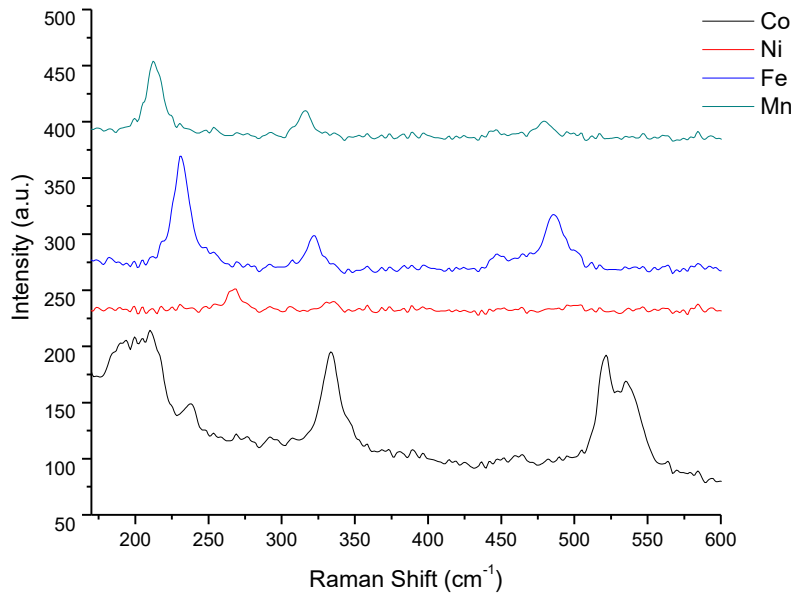
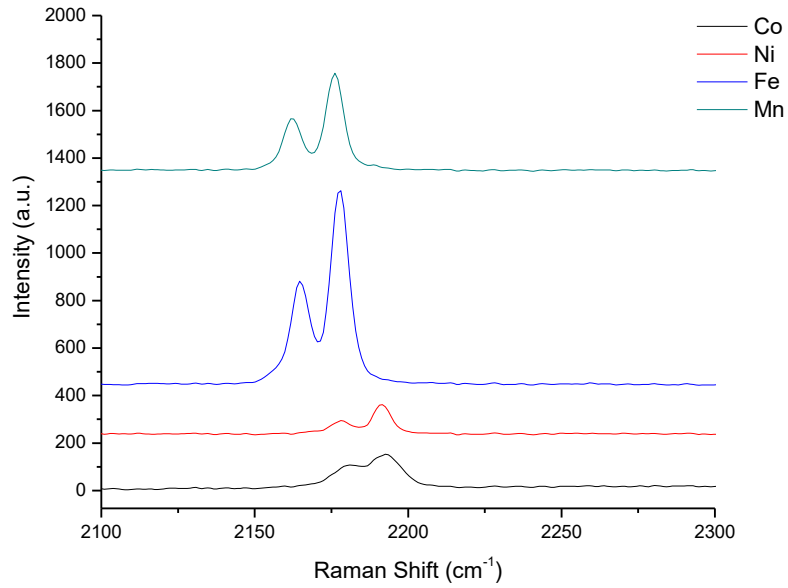
APPENDIX SECTION

Appendix 1: NaCl %, TDS and conductivity of filtered water samples using the Teflon impregnated with metal complex.

Sample Name	Sample Conc	Hanna Instrument Readings																				AVR Reading
		Trial 1				Trial 2				Trial 3				Trial 4				Trial 5				
		NaCl (%)	TDS (ppm)	EC (µs/cm)	T (°C)	NaCl (%)	TDS (ppm)	EC (µs/cm)	T (°C)	NaCl (%)	TDS (ppm)	EC (µs/cm)	T (°C)	NaCl (%)	TDS (ppm)	EC (µs/cm)	T (°C)	NaCl (%)	TDS (ppm)	EC (µs/cm)	T (°C)	
NaCl	0.001	0.2	82.3	164.4	24.3	0.2	83.9	168.9	24.2	0.2	79.2	158.5	24	0.2	81.4	163.1	23.6	0.2	81.9	164.2	23.5	0.2
NaCl	0.002	0.4	152	303	24.3	0.4	160	321	23.7	0.4	152	305	23.7	0.4	156	312	23.4	0.4	157	315	23.4	0.4
NaCl	0.005	0.8	301	603	24	0.8	301	603	23.6	0.8	290	578	23.5	0.8	293	586	23.6	0.8	298	596	23.8	0.8
NaCl	0.01	1.5	543	1084	24.3	1.5	552	1103	23.8	1.5	560	1180	23.3	1.5	558	1115	23.3	1.4	509	1021	23.5	1.48
NaCl	0.02	3.1	1100	2200	24.3	3.1	1106	2211	23.5	3.1	1098	2197	23.1	3.1	1100	2202	23.2	3	1081	2172	23.6	3.08
NaCl	0.05	7.1	2540	5100	24	6.9	2470	4930	24.1	6.8	2430	4840	23.8	6.6	2360	4700	24	6	2140	4270	23.8	6.68
NaCl	0.1	12.7	4560	9120	24.3	12.2	4390	8750	24.4	12	4300	8610	24	11.5	4110	8240	23.8	11.3	4060	8120	23.8	11.94
Fe		5.9	2120	4260	24.1	6.4	2290	4590	23.7	6.5	2320	4630	23.1	6.7	2400	4810	22.8	7.3	2630	5230	22.5	6.56
FeDDP		5.9	2110	4230	24.6	6	2150	4320	23.4	6.2	2240	4470	23	6.7	2410	4820	22.8	7.4	2650	5290	22.8	6.44
Mn		5.3	1890	3780	24.3	5.5	1990	3970	23.7	5.9	2130	4260	23	7.1	2560	5090	22.3	7.4	2660	5310	22.4	6.24
MnDDP		6.1	2210	4420	24.3	6.3	2290	4570	23.6	6.5	2320	4700	23	6.8	2420	4840	22.7	7.3	2620	5230	22.9	6.6
Ni		6	2150	4340	24.2	6.4	2330	4620	23.3	6.8	2430	4850	23.3	7	2500	5010	23	7.2	2580	5160	23.1	6.68
NiDDP		6.5	2320	4640	24.4	6.3	2270	4550	23.3	6.6	2360	4720	23.1	7.1	2560	5110	23.2	7.5	2620	5360	23	6.8
Co		6.3	2260	4510	24.4	5.3	1920	3840	24.1	6	2160	4300	23.5	6.7	2410	4810	23.1	7	2520	5040	23.3	6.26

CoDDP		7.1	2550	5070	24.3	7.7	2760	5520	24.1	8.4	3020	6010	23.4	8.9	3200	6360	23.1	9.8	3510	7020	23.3	8.38
Pristine		11.2	4020	8030	24.2	11	3960	7890	23.7	10.6	3800	7600	23.7	10.1	3630	7260	23.4	10.4	3760	7510	23.4	10.66

Appendix 2: Comparison of the Raman shift for Fe, Mn, Ni and Co samples showing the peak broadening in Co, and shift in wavenumber from Mn to Co



Appendix 3: Total dissolve solid, electrical conductivity and NaCl % measured for the respective filtered produce water samples obtained by using the initial compressed caked over sintered glass method. Hanna Instrument was used for the measurements at 22.9°C.

Sample	TDS (g/l)	Electrical Conductance (ms/cm)	NaCl (%)
Control produce water	10.52	23.71	31.8
FeNi(CN) ₄ +BzoH+DDP	7.10	14.35	17.7
FeNi(CN) ₄ +DDP	7.15	23.94	28.4
FeNi(CN) ₄ +BzoH	11.8	24.07	30.5
CdNi(CN) ₄ +BzoH	11.74	24.29	29.8
CdNi(CN) ₄ +DDP	11.48	22.8	28.6
CdNi(CN) ₄ +BzoH+DDP	12.06	24.37	30.1
CoNi(CN) ₄ +BzoH	9.8	19.39	24.1
CoNi(CN) ₄ +BzOH+DDP	6.98	13.40	17.1
MnNi(CN) ₄ +BzoH	6.86	13.60	17.1
MnNi(CN) ₄ +DDP	7.15	14.41	18.3

REFERENCES

1. Xu, P., et al., *Porous graphene: Properties, preparation, and potential applications*. Chinese Science Bulletin, 2012. 57(23): p. 2948-2955.
2. Lee, C., et al., *Measurement of the Elastic Properties and Intrinsic Strength of Monolayer Graphene*. Science, 2008. 321(5887): p. 385.
3. Beall, G.W., et al., *Single crystalline graphene synthesized by thermal annealing of humic acid over copper foils*. Physica E: Low-dimensional Systems and Nanostructures, 2014. 56: p. 331-336.
4. Ferrari, A.C., et al., *Science and technology roadmap for graphene, related two-dimensional crystals, and hybrid systems*. Nanoscale, 2015. 7(11): p. 4598-4810.
5. Iwamoto, T., *Past, present and future of the clathrate inclusion compounds built of cyanometallate hosts*. Journal of inclusion phenomena and molecular recognition in chemistry, 1996. 24(1): p. 61-132.
6. JeongYong Lee; Omar K. Farha; John Roberts, K.A.S.S.T.N.J.T.H., *Metal-Organic Framework Materials as Catalyst*. The Royal Society of Chemistry, 2009.
7. Gray, H.B. *Electronic Structures of Square Planar Metal Complexes*. in *Proceedings of the 8th International Conference on Coordination Chemistry*. 1964. Vienna: Springer Vienna.
8. Nash, T.L., et al., *2-D transition metal cyanide nanosheets as precursor material for an ultra-low platinum group metal catalyst*. 2014.

9. Keppler, H., *Crystal Field Theory*, in *Encyclopedia of Geochemistry: A Comprehensive Reference Source on the Chemistry of the Earth*, W.M. White, Editor. 2017, Springer International Publishing: Cham. p. 1-4.
10. Kauffman, G.B. and J. Halpern, *Coordination compound*, in *Encyclopædia Britannica* 2018, Encyclopædia Britannica, inc. .
11. Ludi, A., *Prussian blue, an inorganic evergreen*. *Journal of Chemical Education*, 1981. 58(12): p. 1013.
12. Coleby, L.J.M., *A history of Prussian blue*. *Annals of Science*, 1939. 4(2): p. 206-211.
13. Harris, T.D., et al., *Record ferromagnetic exchange through cyanide and elucidation of the magnetic phase diagram for a Cu(II)Re(IV)(CN)₂ chain compound*. (1520-5126 (Electronic)).
14. Culp, J.T., et al., *Interface directed assembly of cyanide-bridged Fe–Co and Fe–Mn square grid networks*. *Polyhedron*, 2003. 22(22): p. 3059-3064.
15. Goss, M., *A Novel 2-D Transition Metal Cyanide Membrane: Modeling, Structural, Magnetic, and Functional Characterization*. 2015, Texas State University, San Marcos, Texas.
16. Culp, J.T., et al., *Magnetism of metal cyanide networks assembled at interfaces*. *Coordination Chemistry Reviews*, 2005. 249(23): p. 2642-2648.
17. Palin, D.E. and H.M. Powell, *The structure of molecular compounds; the clathrate compound of quinol and methanol*. *Journal of the Chemical Society*, 1948. 2: p. 571-574.

18. Keggin J.F., M., *Structures and Formulae of the Prussian Blues and Related Compounds*. Nature, 1936. 137: p. 577-578.
19. Buser, H.J., Ludi, A., Petter, W., Schwarzenbach, D., *Erratum: Single-crystal study of prussian blue: $Fe_4[Fe(CN)_6]_2 \cdot 14H_2O$* . Journal of the Chemical Society, Chemical Communications, 1972.
20. Beall, G.W., et al., *Crystal structure and Raman spectral study of ligand substitution in $Mn_3[Co(CN)_6]_2 \cdot xL$* . Inorganic Chemistry, 1978. 17(11): p. 2978-2981.
21. Beall, G.W., et al., *Crystal structure of $Mn_3(Co(CN)_6)_2 \cdot 12H_2O$ and $Cd_3(Co(CN)_6)_2 \cdot 12H_2O$ by neutron and x-ray diffraction*. 1977.
22. Brown, I.D., *On the geometry of O H...O hydrogen bonds*. Acta Crystallographica Section A, 1976. 32(1): p. 24-31.
23. Brown, D.B. and D.F. Shriver, *Structures and solid-state reactions of Prussian blue analogs containing chromium, manganese, iron, and cobalt*. Inorganic Chemistry, 1969. 8(1): p. 37-42.
24. Weiser, H.B., W.O. Milligan, and J.B. Bates, *X-ray Diffraction Studies on Heavy-metal Iron-cyanides*. The Journal of Physical Chemistry, 1942. 46(1): p. 99-111.
25. Dinolfo, P.H. and J.T. Hupp, *Supramolecular Coordination Chemistry and Functional Microporous Molecular Materials*. Chemistry of Materials, 2001. 13(10): p. 3113-3125.
26. Morales, A.M. and C.M. Lieber, *A Laser Ablation Method for the Synthesis of Crystalline Semiconductor Nanowires*. Science, 1998. 279(5348): p. 208.

27. Weissbuch, I., et al., *Self-Assembly at the Air–Water Interface. In-Situ Preparation of Thin Films of Metal Ion Grid Architectures*. Journal of the American Chemical Society, 1998. 120(19): p. 4850-4860.
28. Weissbuch, I., et al., *Oriented Crystalline Monolayers and Bilayers of 2×2 Silver(I) Grid Architectures at the Air-Solution Interface: Their Assembly and Crystal Structure Elucidation*. Chemistry – A European Journal, 2000. 6(4): p. 725-734.
29. Magnera, T.F., et al., *The organometallic ‘molecular tinkertoy’ approach to planar grid polymers*. Journal of Organometallic Chemistry, 1997. 548(1): p. 83-89.
30. Ferlay, S., et al., *A room-temperature organometallic magnet based on Prussian blue*. Nature, 1995. 378(6558): p. 701-703.
31. Hatlevik, Ø., et al., *Enhancement of the Magnetic Ordering Temperature and Air Stability of a Mixed Valent Vanadium Hexacyanochromate(III) Magnet to 99 °C (372 K)*. Advanced Materials, 1999. 11(11): p. 914-918.
32. Gadet, V., et al., *High-TC molecular-based magnets: a ferromagnetic bimetallic chromium(III)-nickel(II) cyanide with TC = 90 K*. Journal of the American Chemical Society, 1992. 114(23): p. 9213-9214.
33. Holmes, S.M. and G.S. Girolami, *Sol-gel synthesis of KV(II)[Cr(III)(CN)₆]} · 2H₂O: A crystalline molecule-based magnet with a magnetic ordering temperature above 100 C*. 1999.

34. Liu, J.Y., et al., *Three cyanide-bridged assemblies induced by positive ions: Hydrothermal syntheses, crystal and powder X-ray structures*. *Inorganica Chimica Acta*, 2013. 407: p. 126-130.
35. Pei, D., et al., *Electronic structure, bonding and phonon modes in the negative thermal expansion materials of Cd(CN)₂ and Zn(CN)₂*. *Journal of Physics: Condensed Matter*, 2008. 20(27): p. 275224.
36. Zhang, Y.-Q. and C.-L. Luo, *On the Origin of Magnetic Anisotropy in Cyanide-Bridged Co₉M₆ (M = MoV or WV) Systems: A DFT Study*. *Inorganic Chemistry*, 2009. 48(22): p. 10486-10488.
37. Beall, G.W. and M. Goss, *Self-assembly of organic molecules on montmorillonite*. *Applied Clay Science*, 2004. 27(3): p. 179-186.
38. Kresse, G., *VASP the GUIDE*. <http://cms.mpi.univie.ac.at/vasp/>.
39. Nash, T.L., et al., *Modeling, Characterization, and Exfoliation of a New Family of 2-D Materials*. *Science of Advanced Materials*, 2014. 6(4): p. 703-713.
40. Lukov, V.V., et al., *Modern studies in the area of molecular magnets: State, problems, and prospects*. *Russian Journal of Coordination Chemistry*, 2015. 41(1): p. 1-15.
41. Gallagher, N.M., A. Olankitwanit, and A. Rajca, *High-Spin Organic Molecules*. *The Journal of Organic Chemistry*, 2015. 80(3): p. 1291-1298.
42. Cohen-Tanugi, D. and J.C. Grossman, *Nanoporous graphene as a reverse osmosis membrane: Recent insights from theory and simulation*. *Desalination*, 2015. 366: p. 59-70.

43. Bunch, J.S., et al., *Impermeable Atomic Membranes from Graphene Sheets*. Nano Letters, 2008. 8(8): p. 2458-2462.
44. Holt, J.K., et al., *Fast Mass Transport Through Sub-2-Nanometer Carbon Nanotubes*. Science, 2006. 312(5776): p. 1034.
45. Corry, B., *Designing Carbon Nanotube Membranes for Efficient Water Desalination*. The Journal of Physical Chemistry B, 2008. 112(5): p. 1427-1434.
46. Thomas, M., B. Corry, and T.A. Hilder, *What have we learnt about the mechanisms of rapid water transport, ion rejection and selectivity in nanopores from molecular simulation?* Small (Weinheim an der Bergstrasse, Germany), 2014. 10(8): p. 1453-1465.
47. Zhang, J., et al., *Enhanced precipitation of cyanide from electroplating wastewater via self-assembly of bimetal cyanide complex*. Separation and Purification Technology, 2015. 150: p. 179-185.
48. Yurdaku, Ş., *Fourier transform infrared and Raman spectroscopic studies on 8-hydroxyquinoline metal(II) tetracyanonickelate complexes*. Journal of Molecular Structure, 1997. 412(3): p. 231-237
49. Tran Cao, D., et al., *Modification of the SERS spectrum of cyanide traces due to complex formation between cyanide and silver*. Advances in Natural Sciences: Nanoscience and Nanotechnology, 2018. 9(2): p. 025006.
50. Gopal Reddy, C.V., et al., *A highly sensitive Raman method for selective cyanide detection based on evaporated cuprous iodide substrate*. Analytical Methods, 2010. 2(5): p. 458-460.

51. Han, S., et al., *Resonance Raman studies of Escherichia coli sulfite reductase hemoprotein. 3. Bound ligand vibrational modes*. Biochemistry, 1989. 28(13): p. 5477-5485.
52. Gardner, M.T., et al., *Vibrational Analysis of a Molecular Heme–Copper Assembly with a Nearly Linear Fe(III)–CN–Cu(II) Bridge: Insight into Cyanide Binding to Fully Oxidized Cytochrome c Oxidase*. Inorganic Chemistry, 1996. 35(23): p. 6878-6884
53. Sabale, S., et al., *Synthesis and Properties of Monodisperse Superparamagnetic $Mg_{0.8}Mn_{0.2}Fe_2O_4$ Nanoparticles Using Polyol Reflux Method*. Acta Metallurgica Sinica (English Letters), 2014. 27(6): p. 1122-1126.
54. Pankhurst, Q.A., et al., *Applications of magnetic nanoparticles in biomedicine*. Journal of Physics D: Applied Physics, 2003. 36(13): p. R167-R181.
55. Duraia, E.-S.M. and K.A. Abdullin, *Ferromagnetic resonance of cobalt nanoparticles used as a catalyst for the carbon nanotubes synthesis*. Journal of Magnetism and Magnetic Materials, 2009. 321(24): p. L69-L72.
56. Köseoğlu, Y., et al., *Synthesis and characterization of $ZnFe_2O_4$ magnetic nanoparticles via a PEG-assisted route*. Journal of Alloys and Compounds, 2008. 462(1): p. 209-213.
57. Mahmoud, M.H., et al., *Mössbauer and magnetization studies of nickel ferrite nanoparticles synthesized by the microwave-combustion method*. Journal of Magnetism and Magnetic Materials, 2013. 343: p. 21-26.

58. Zhang, D., et al., *Templated fabrication of NiFe₂O₄ nanorods: Characterization, magnetic and electrochemical properties*. *Solid State Sciences*, 2009. 11(1): p. 113-117.
59. Kale, A., S. Gubbala, and R.D.K. Misra, *Magnetic behavior of nanocrystalline nickel ferrite synthesized by the reverse micelle technique*. *Journal of Magnetism and Magnetic Materials*, 2004. 277(3): p. 350-358.
60. Prabhakaran, T. and J. Hemalatha, *Combustion synthesis and characterization of highly crystalline single phase nickel ferrite nanoparticles*. *Journal of Alloys and Compounds*, 2011. 509(25): p. 7071-7077.
61. Wang, J., et al., *Solvothermal synthesis and magnetic properties of size-controlled nickel ferrite nanoparticles*. *Journal of Alloys and Compounds*, 2009. 479(1): p. 791-796.
62. Nejati, K. and R. Zabihi, *Preparation and magnetic properties of nano size nickel ferrite particles using hydrothermal method*. *Chemistry Central Journal*, 2012. 6(1): p. 23.
63. Dixit, G., et al., *Structural, magnetic and optical studies of nickel ferrite thin films*. *Adv. Mater. Lett*, 2012. 3(1): p. 21-26.
64. Moretti, G. and C. Gervais, *Raman spectroscopy of the photosensitive pigment Prussian blue*. *Journal of Raman Spectroscopy*, 2018. 49(7): p. 1198-1204.
65. Kim, K., J.W. Lee, and K.S. Shin, *Cyanide SERS as a platform for detection of volatile organic compounds and hazardous transition metal ions*. *Analyst*, 2013. 138(10): p. 2988-2994.

66. Grandjean, F., L. Samain, and G.J. Long, *Characterization and utilization of Prussian blue and its pigments*. Dalton Transactions, 2016. 45(45): p. 18018-18044.
67. Duraia, E.-S.M. and G.W. Beall, *Large temperature-induced red shift of G-band of functionalized graphene nanosheets synthesized from humic acid*. Superlattices and Microstructures, 2016. 98: p. 379-384.
68. Duraia, E.-S.M., et al., *Humic acid-derived graphene-SnO₂ nanocomposites for high capacity lithium-ion battery anodes*. Journal of Materials Science: Materials in Electronics, 2018. 29(10): p. 8456-8464.
69. Duraia, E.-S.M., A. Fahami, and G.W. Beall, *Microwave-Assisted Synthesis of N-Doped Graphene-Wrapped MnO₂ Nanoflowers*. Journal of Electronic Materials, 2018. 47(12): p. 7288-7295.
70. Opherden, L., et al., *Inverted hysteresis and negative remanence in a homogeneous antiferromagnet*. Physical Review B, 2018. 98(18): p. 180403.
71. Aharoni, A., *Exchange anisotropy in films, and the problem of inverted hysteresis loops*. Journal of Applied Physics, 1994. 76(10): p. 6977-6979.
72. Ziese, M., I. Vrejoiu, and D. Hesse, *Inverted hysteresis and giant exchange bias in La_{0.7}Sr_{0.3}MnO₃/SrRuO₃ superlattices*. Applied Physics Letters, 2010. 97(5): p. 052504.
73. Wu, S.Y., et al., *Proteresis of Cu₂O/CuO core-shell nanoparticles: Experimental observations and theoretical considerations*. Journal of Applied Physics, 2014. 116(19): p. 193906.

74. Ma, J. and K. Chen, *Modulated self-reversed magnetic hysteresis in iron oxides*. Scientific Reports, 2017. 7: p. 42312.
75. Sutka, A. and G. Mezinskis, *Sol-gel auto-combustion synthesis of spinel-type ferrite nanomaterials*. Frontiers of Materials Science, 2012. 6(2): p. 128-141.
76. Osińska, M., *Decomposition of gaseous HCN in the presence of Ni-containing catalysts*. Reaction Kinetics, Mechanisms and Catalysis, 2013. 109(1): p. 57-65.